

UNIVERSITY OF AMSTERDAM

MASTERS THESIS

Modelling Diffusive Signals for the Germination of *Aspergillus* Conidia

Examiner:

Dr. J.A. Kaandorp

Author:

Boyan MIHAYLOV

Supervisor:

Prof. dr. H.A.B. Wösten

Assessor:

assessor name

*A thesis submitted in partial fulfilment of the requirements
for the degree of Master of Science in Computational Science*

in the

Computational Science Lab
Informatics Institute

June 2025



Declaration of Authorship

I, Boyan MIHAYLOV, declare that this thesis, entitled ‘Modelling Diffusive Signals for the Germination of *Aspergillus* Conidia’ and the work presented in it are my own. I confirm that:

- This work was done wholly or mainly while in candidature for a research degree at the University of Amsterdam.
- Where any part of this thesis has previously been submitted for a degree or any other qualification at this University or any other institution, this has been clearly stated.
- Where I have consulted the published work of others, this is always clearly attributed.
- Where I have quoted from the work of others, the source is always given. With the exception of such quotations, this thesis is entirely my own work.
- I have acknowledged all main sources of help.
- Where the thesis is based on work done by myself jointly with others, I have made clear exactly what was done by others and what I have contributed myself.

Signed:

Your signature

Date: June 2025

“Algebra is applied to the clouds; the radiation of the star profits the rose; no thinker would venture to affirm that the perfume of the hawthorn is useless to the constellations. Who, then, can calculate the course of a molecule? [...] Germination is complicated with the bursting forth of a meteor and with the peck of a swallow cracking its egg, and it places on one level the birth of an earthworm and the advent of Socrates. Where the telescope ends, the microscope begins. Which of the two possesses the larger field of vision? Choose. A bit of mould is a pleiad of flowers; a nebula is an ant-hill of stars.”

Victor Hugo

UNIVERSITY OF AMSTERDAM

Abstract

Faculty of Science
Informatics Institute

Master of Science in Computational Science

Modelling Diffusive Signals for the Germination of *Aspergillus* Conidia

by Boyan MIHAYLOV

Include your abstract here Abstracts must include sufficient information for reviewers to judge the nature and significance of the topic, the adequacy of the investigative strategy, the nature of the results, and the conclusions. The abstract should summarize the substantive results of the work and not merely list topics to be discussed.

Length 200-400 words.

Acknowledgements

Thank the people that have helped, supervisors family etc.

Contents

Declaration of Authorship	i
Abstract	iii
Acknowledgements	iv
Contents	v
List of Figures	viii
List of Tables	x
Abbreviations	xi
1 Introduction	1
2 Literature Review	6
2.1 The <i>Aspergillus</i> genus	6
2.1.1 Description	6
2.1.2 The role of heterogeneity	7
2.2 Conidial germination	8
2.2.1 Germination phases	8
2.2.2 Factors for germination	8
2.3 Germination inhibitor	9
2.3.1 Volatile organic compounds	9
2.3.2 1-octen-3-ol	10
2.3.3 Open questions	11
2.4 The conidial cell wall	11
2.4.1 Function and dimensions	11
2.4.2 The inner cell wall layers	12
2.4.3 The outer cell wall layers	13
2.5 Conidial aggregation	13
2.6 Diffusion	14
2.6.1 The diffusion constant	14
2.6.2 The permeation constant	14

2.6.3	Estimating the diffusion and permeation constants	15
2.7	Adsorption	17
2.8	Modelling	17
3	Methods	19
3.1	General assumptions	19
3.2	Mathematical foundations	20
3.2.1	Diffusion	20
3.2.2	Permeation	21
3.2.3	Adsorption	22
3.3	Computational models	24
3.3.1	Numerical models: general considerations	25
3.3.2	Numerical model: macroscopic scale	27
3.3.3	Numerical model: spore scale	29
3.3.4	Numerical model: cell wall scale	31
3.3.5	Analytical models	33
3.3.6	Model comparison setup	37
3.4	Model parameters	38
3.4.1	Diffusion and permeation constants	38
3.4.2	Initial and threshold concentrations	41
3.4.3	Adsorption parameters	42
3.5	Inducer permeation	42
3.6	Inhibitor release computations	43
3.6.1	Single-spore experiment setup	44
3.6.2	Multi-spore experiment setup	44
3.6.3	Spore cluster experiment setup	44
3.7	Parameter estimation	45
3.7.1	Data	45
3.7.2	From deterministic to statistical models	46
3.7.2.1	Independent germination factors	47
3.7.2.2	Inhibitor-dependent induction	48
3.7.2.3	Inducer-dependent inhibition	50
3.7.2.4	Variable permeability model	51
3.7.2.5	Random variable distributions	51
3.7.3	Equilibrium probabilities	52
3.7.4	Parameter ranges	52
3.7.5	Fitting the parameters to experimental data	53
3.8	Julia implementation	54
4	Results	56
4.1	Model comparisons	56
4.2	Single-spore experiments	58
4.3	Multi-spore experiments	60
4.4	Spore cluster experiments	61
4.5	Parameter estimation	64
4.5.1	Basic models and <i>A. niger</i> data	64
4.5.2	Combined models	66

4.5.3	Models with variable permeability	70
4.5.4	Selected models and <i>A. nidulans</i> data	70
5	Discussion	74
5.1	Natural scenario	74
5.2	Model characteristics	74
5.3	Inhibition timing	76
5.4	Effect of spore clusters	77
5.5	Germination models	78
5.6	Interpretation of estimated parameters	80
6	Conclusion and Future Work	82
7	Ethics and Data Management	84
A	Estimated Parameters	86
B	Fitting Models To <i>A. nidulans</i> Data	89
	Bibliography	92

List of Figures

3.1	In the macroscopic-scale model (low resolution), the spore (system A) does not interfere with the flow of diffusion in the medium (system B) due to its relatively small volume. It does, however, serve as a source or a sink for the concentration in its containing lattice node (cube with black outline).	28
3.2	The spore-scale (medium-resolution) model: the flux J' at the spore-medium interface is governed by slow permeation, while the flux J in the medium is governed by fast diffusion.	30
3.3	Two options for the inhibitor distribution in the high-resolution model: homogeneous in the entire spore (left) or restricted to the cell wall (right). The images are cross-sections through the centre of the three-dimensional lattice.	32
3.4	Schematic representation of the designated volume for each spore.	34
3.5	Diagrammatic views of the different scenarios for the initial inhibitor concentration (inhibitor marked in yellow). Abbreviations: m/r - melanin/rodlets, c/p - chitin/polysaccharides, mem - cell membrane.	40
3.6	Visualisation of intermediate spore densities and the corresponding centre-to-centre distances between the spores.	44
3.7	A densely packed 13-spore cluster.	45
4.1	Comparison of the concentration time course for all inhibitor depletion models in a single-spore setup.	57
4.2	Comparison of the concentration time course for all inhibitor depletion models in a multi-spore setup.	57
4.3	Spore-to-spore distance versus residual inhibitor concentration for the volume-based analytical model and the medium-resolution numerical model.	58
4.4	Results from the single-spore experiments, plotted on a log-log scale. Top row: internal concentration evolutions for 1-octen-3-ol permeating simple-material barriers (left) and composite barriers (right). The curves for 1-octen-3-ol through water and 1-octen-3-ol through agarose decay too fast to be shown on the logarithmic axis. Bottom row: internal concentration evolutions for a hypothetical permeation reaching thresholds of different magnitude at 4 hours of incubation (left) and at 2 hours of incubation (right).	59
4.5	Time courses of the internal inhibitor concentration for the extreme values of the tested permeation constants (P_s) and spore densities (ρ_s), corresponding to spore-to-spore distances (L) in the multi-spore experiments. The green dashed lines indicate the equilibrium concentration in the spore according to the volume-based model. The red dashed lines indicate the fitted exponential law in the early time of release (first 10 min).	61

4.6	Analysis of the early-time release exponent for different permeation constants (P_s). Left: relationship between spore density and the normalised exponent (semi-logarithmic plot). Right: relationship between spore-to-spore distance and the normalised exponent (double-logarithmic plot)	62
4.7	Cross-sections through the 3D lattice at different moments in time, with colour gradients indicating the inhibitor concentration. Top two rows: simulations with a full-spore inhibitor distribution. Bottom two rows: simulations with a protoplast excluded from diffusion.	63
4.8	Time course of the internal inhibitor concentrations for the cases illustrated in Figure 4.7.	64
4.9	<i>A. niger</i> germination data vs. germination probabilities predicted by the models. Top: density-dependent long-term germination probability (p_{\max}). Bottom: time-dependent germination probability of the volume-based model (VBM) vs. the Dantigny model (DM), with p_{\max} (red dashed line) and τ_g (green dashed line).	65
4.10	<i>A. niger</i> germination data vs. germination probabilities predicted by the models. Top plots: density-dependent long-term germination probability (p_{\max}). Bottom plots: time-dependent germination probability of the volume-based model (VBM) vs. the Dantigny model (DM), with p_{\max} (red dashed lines) and τ_g (green dashed lines).	67
4.11	<i>A. niger</i> germination data vs. germination probabilities predicted by the models. Top plots: density-dependent long-term germination probability (p_{\max}). Bottom plots: time-dependent germination probability of the volume-based model (VBM) vs. the Dantigny model (DM), with p_{\max} (red dashed lines) and τ_g (green dashed lines).	69
4.12	<i>A. niger</i> germination data vs. germination probabilities predicted by the models with variable α . Top plots: density-dependent p_{\max} . Bottom plots: time-dependent germination probability of the volume-based model (VBM) vs. the Dantigny model (DM), with p_{\max} (red dashed lines) and τ_g (green dashed lines).	71
4.13	<i>A. niger</i> germination data vs. germination probabilities predicted by the models with variable α . Top: density-dependent long-term germination probability (p_{\max}). Bottom: time-dependent germination probability vs. Dantigny curves.	72
5.1	Diagrammatic illustration of the basic germination models (left column) and their enhancement through combinations (central column) and through the addition of varying cell wall permeability (right column). G indicates the germination event, C denotes the carbon source (inducer) and I denotes the inhibitor. The thresholds for the two germination factors are indicated by the Γ -like symbols. The dashed red line indicates the best performing model.	79
B.1	<i>A. nidulans</i> germination data vs. germination probabilities predicted by the $(I \rightarrow T)C \wedge I$ model.	89
B.2	<i>A. nidulans</i> germination data vs. germination probabilities predicted by the $(I \rightarrow S)C \wedge I$ model.	90
B.3	<i>A. nidulans</i> germination data vs. germination probabilities predicted by the $(I \rightarrow T+S)C \wedge I$ model.	91

List of Tables

3.1	Diffusion coefficient (D) and permeation coefficient (P_s) of glucose in various media. The D coefficient for hydrophobins is assumed equal to that for lipids.	39
3.2	Diffusion coefficient (D) and permeation coefficient (P_s) of 1-octen-3-ol in various media. The D coefficient for hydrophobins is assumed equal to that for lipids.	40
3.3	Composite layer permeation coefficients (P_{total}) for 1-octen-3-ol in various scenarios of barrier composition.	41
3.4	Free parameter bounds and units.	53
4.1	Permeation constants fitted to produce a 4-hour and a 2-hour depletion of the internal inhibitor to different threshold values.	59
A.1	Parameters for the $(I \rightarrow T)C \wedge I$, $(I \rightarrow S)C \wedge I$ and $(I \rightarrow T+S)C \wedge I$ models, fitted on <i>A. niger</i> data by Ijadpanahsaravi et al. [1]; *: alanine, **: proline.	86
A.2	Parameters for the $C \wedge I$, $(I \rightarrow T)C \wedge I$, $(I \rightarrow S)C \wedge I$ and $(I \rightarrow T+S)C \wedge I$ models with varying permeability, fitted on <i>A. niger</i> data by Ijadpanahsaravi et al. [1]; *: alanine, **: proline.	87
A.3	Parameters for the $(I \rightarrow T)C \wedge I$, $(I \rightarrow S)C \wedge I$ and $(I \rightarrow T+S)C \wedge I$ models, fitted on <i>A. nidulans</i> germination data with density-driven inhibition by Herrero-Garcia et al. [2].	87
A.4	Parameters for the $(I \rightarrow T)C \wedge I$, $(I \rightarrow S)C \wedge I$ and $(I \rightarrow T+S)C \wedge I$ models, fitted on <i>A. nidulans</i> data of exogenously inhibited germination by Herrero-Garcia et al. [2].	88
A.5	Parameters for the $(I \rightarrow T)C \wedge I$, $(I \rightarrow S)C \wedge I$ and $(I \rightarrow T+S)C \wedge I$ models, fitted on <i>A. nidulans</i> data with both density-driven and exogenously driven inhibition by Herrero-Garcia et al. [2].	88

Abbreviations

cAMP-PKA	cyclic adenosine monophosphate - protein kinase A
CARS	coherent anti-Stokes Raman spectroscopy
CDF	cumulative distribution function
COBYLA	constrained optimisation by linear approximation
CPU	central processing unit
DE	differential evolution
DHN	dihydroxynaphthalene
DM	Dantigny model
DPPC	dipalmitoylphosphatidylcholine
FITC	fluorescein isothiocyanate
GLUT1	glucose transporter 1
GPI	glycosylphosphatidylinositol
GPU	graphics processing unit
ODE	ordinary differential equation
PDF	probability density function
RAM	random access memory
RMSE	root mean square error
TEM	transmission electron microscope
VBM	volume-based model
VOC	volatile organic compound

Chapter 1

Introduction

A mould colony of the *Aspergillus* genus grows on a substrate of decaying matter. As part of its reproductive cycle, it forms a multitude of conidiophores - finger-like arrays of highly resistant asexual spores (conidia) exhibited on its outer surface. Whether picked up by the wind, brushed by the hydrophobic legs of an insect or swept by a rolling raindrop, spores, conidiophores or even entire pieces of the colony may end up submerged in an aqueous medium, such as a small puddle or a dew drop. Such an environment carries a lot of benefits for the fungus: the low viscosity of water allows compounds to dissolve and diffuse better. At the same time, the hydrophobic coating of conidia imposes a tight control over substances entering their cell wall. If the medium contains the nutrients required for survival, the spores will soon germinate, absorbing water from their environment and forming germ tubes, which expand into the mycelium of a growing colony. In a similar way, *Aspergillus* moulds are submerged in artificial bioreactors and cultivated for the production of useful substances.

Diffusion, a major driving force in such environments, is a process intuitively associated with the loss of order — a random dispersion of particles to a high-entropy equilibrium. Yet, this spontaneously irreversible phenomenon, fundamental to the physical universe, gives rise to complex order by fuelling the processes of life, transporting molecules through mere thermal fluctuations, timing transformative events in the development of organisms, like an ingeniously simple hourglass. It is a process on a molecular level with measurable consequences on any higher scale and with mechanics extensively described by mathematics. Diffusion is also a potential tool for *Aspergillus* fungi to control their transition from long-lasting dormant spores to vegetative mycelium. This thesis applies the methodology of Computational Science to compile knowledge about diffusion and conidial physiology and propose a model that captures essential principles of diffusive signalling in *Aspergillus* germination.

It has been observed that the conidia within an inoculum coordinate their germination depending on their density, and furthermore have a different germination behaviour depending on the potential nutrients present in their surrounding. This has led to the recognition of two major signalling mechanisms at play - inhibitory signals between spores [2] and inducing signals caused by the presence of readily assimilable molecules [3]. Known germination inducers are the consumable carbon sources glucose and amino acids [4]. A popular inhibitor candidate with a disputed effect on germination is 1-octen-3-ol [2, 5]. The current studies focus on a hypothesis in which both signals are enabled by the passive diffusion of molecules. An inducing molecule needs to access the receptor proteins embedded in the conidial cell wall. A relevant question is whether its inducing action is timed by the permeability of the cell wall and the surrounding medium. Following the opposite direction, inhibitor molecules are assumed to be released from the spore into the medium, where they randomly disperse to other spores. In this case, not only is the timing relevant, but also the ambient saturation of inhibitor from the simultaneous release by many spores.

The main research question the thesis aims to address is, can a diffusion-based model of inhibition and induction explain germination patterns of *Aspergillus* spores, and do known carbon source molecules and 1-octen-3-ol fit in the two respective mechanisms? At a lower level, this requires an investigation of the concentration of left in the spore at a given time, such that germination is possible. This applies to both phenomena of interest: the release of inhibitor molecules until their saturation in the medium and the passive intake of inducer molecules until their saturation in the cell wall. The objective of this thesis is to construct a meaningful mathematical representation of diffusive signals, the interactions between them and their role in germination, compiled in a relatively simple model that can be tested against experimental data. To this end, a special focus is put on the inhibitor release, envisioning the spore as a spherical container of a finite quantity of inhibitor molecules, separated from the extracellular medium by a semi-permeable boundary. The assumption for this scenario is that the inhibitor is not substantially renewed in the dormant spore and can therefore diffuse out to its complete depletion or until equilibration between the internal and the external concentration. Beyond a given depletion threshold, the germination is considered uninhibited. This framework is then adapted to model the entry of carbon sources into the cell wall.

To model the diffusion processes, a combination of numerical simulations and analytical derivations is employed. These address some intermediate research questions: How fast does a single spore release an inhibitor with specific molecular properties? How does the ambient concentration in dense spore cultures slow down the inhibitor release? Do spore clusters retain more inhibitor as opposed to loosely dispersed cultures? How does inhibition interact with induction? How can the heterogeneity of the spores be represented?

This involves modelling spore systems on different scales, with the ultimate goal to obtain a mathematical formula that can be easily used in parameter estimation procedures on available data. Three lattice-based numerical solvers, focussing on a macroscopic scale (low resolution), spore scale (medium resolution) and cell-wall scale (high resolution), are compared to two analytical variants: a simple permeation scheme and an extension of it informed by spore density (referred to as the volume-based model). This serves for validation and verification, highlighting the utility of each model for specific purposes, revealing insights through result discrepancies and affirming the volume-based model as a lightweight but versatile representation of the phenomena of interest.

First, an attempt is made to relate the parameters of barrier permeation models to real quantities documented in literature. Thus, in a system with a single spore, where 1-octen-3-ol is the primary germination inhibitor, slowly released through a lipid bilayer membrane and a cell wall of hydrophobins and polysaccharides, a simple permeation model using known material properties leads to an underestimation of the time needed for the initiation of germination. To explain this discrepancy, two possibilities are observed: first, that upon release the inhibitor strongly interacts with the cell wall through adsorption; and second, that coagulated spores in dense clusters slow down the diffusive flow of inhibitor into the medium. The first case is backed by theoretical support from literature, but exemplary calculations with a standard adsorption model show that known absorption capacities might not be enough to slow down permeation significantly. In the second case, simulations reveal that the volumes occupied by the spores are not sufficient to block the outflow of inhibitor away from the cluster. As for the inducer, a simple check addresses the question of whether permeation through the cell wall limits the timing of carbon signalling. It is found that carbon sources like glucose may indeed be significantly slowed down in their approach toward the carbon receptors.

Having narrowed down the mechanism of inhibitor release in a single spore, it is examined how a multitude of spores can increase the inhibition of the culture. Abstracting the inoculum as a homogeneous grid of inhibitor sources, the density of the grid is varied to explore the equilibration of the inhibitor concentration. Two models with a different fundamental approach, the medium-resolution solver and the volume-based model, manage to represent this phenomenon, illustrating how the density of the spore culture and the permeability of the cell wall interact to drive the extracellular concentration up and to minimise the diffusion-driving concentration gradient.

The final step is an attempt to relate the model to experimental data. It is recognised that documented germination statistics are strongly influenced by the variation of spore characteristics. Since the formulas obtained in the preceding experiments are deterministic representations of permeation processes in an ideal spore, the aspect of heterogeneity

is introduced by replacing some of the parameters in the models with random variables. This results in a combined model of germination induction and inhibition, which serves to predict the germination probability under a given set of parameters. Different variants of this model are developed according to various scenarios, in which either induction or inhibition, or both mechanisms in parallel, trigger germination, and additionally influence each other's actions. Using a differential evolution algorithm in tandem with a non-linear derivative-free local optimiser, the parameters of these variants are tuned to experimental data from experiments with *A. niger* and *A. nidulans*. From this, it is concluded that a model with two germination-triggering criteria: the depletion of an inhibitor and the inhibitor-dependent saturation of an inducer; has most success in explaining the data. However, when trying to account for externally added 1-octen-3-ol to a culture of *A. nidulans*, the models produce inconsistent results, leading to the interpretation that the natural self-inhibition based on spore density has fundamentally different mechanisms from the response to added 1-octen-3-ol, and that the volatile compound is likely not a single primary germination inhibitor for *A. nidulans*.

The thesis is laid out in the following sections. First, a [Literature Review](#) introduces the fungi of the *Aspergillus* genus, highlighting their relevance to human society, their main characteristics and the specifics of their germination, including how spores exhibit self-inhibition and why their cell wall presents a restrictive barrier for molecular signals. The chapter continues with an introduction to the concepts of diffusion and permeation, focussing on the quantification of diffusion parameters relevant to the studies. The concept of adsorption is then briefly presented as a complementary phenomenon affecting diffusion. A short overview of computational models used in the research of fungi is then laid out to contextualise the approach used in the thesis.

The [Methods](#) chapter first presents the most important assumptions and simplifications with regard to the observed developmental time frame, the notion of germination, the physiology of a spore and the mechanism of diffusive signalling. The mathematical and physical theory behind diffusion, permeation and adsorption is then briefly introduced. The chapter proceeds by presenting all models used in the experiments, including the three numerical solvers and the analytical formulas for barrier permeation. The comparative setup through which these models are validated is then described. To represent natural phenomena, the models need to be applied with parameters that correspond to specific material properties, the inference of which is explained in an intermediate section. This is followed by the experimental setup of a single-spore, a multi-spore and a high-resolution spore cluster simulation of inhibitor release. The chapter then introduces the data used in the final model fitting stage, elaborates the stochastic modelling of heterogeneous parameters and the construction of combined inducer/inhibitor-dependent

germination models and, finally, clarifies the optimisation procedure used to fit the models to the data. A concluding section gives some essential technical details on the implementation of the models with the Julia programming language.

The [Results](#) chapter presents the outcome of the computational experiments, starting with the model comparison, the single-spore, multi-spore and spore cluster configurations. Proceeding with the parameter estimation of the germination models, the performance of each model in representing *A. niger* germination data is analysed. This helps to identify some promising variants that are combined into more complex crossovers, which are once again fitted to the data, exhibiting a yet higher performance. The chapter continues with the attempt to reduce the estimation error further in select models by representing the cell wall porosity as a random variable. This highlights three best-performing model candidates from the series, according to which germination is triggered by inhibition release and an inhibitor-dependent induction. Finally, the secondary fitting procedure of the best models to *A. nidulans* data is described.

The [Discussion](#) chapter reflects back on some fundamental assumptions, starting with the reality-check of possible spore densities occurring in nature, then outlining some limitations of the diffusion models. It is reviewed what role the different numerical solvers had in the research process and how well suited they were for it. The chapter proceeds with a more detailed examination and interpretation of the results from the main numerical experiments. Possible reasons for the low inhibitor permeation estimate are discussed. The properties of the analytical model are explained with reference to its mathematical structure. A designated section revisits the significance of the diffusion-limiting effect of spore packing in clusters with regard to the limitations of the applied model. Subsequently, the biological plausibility of the germination models is discussed, which reinforces the outcome of their alignment with germination data. The inability of the best-performing models to capture both endogenously driven and exogenously controlled inhibition in *A. nidulans* germination is interpreted with regard to known controversies around the role of 1-octen-3-ol. In a final section, the estimated parameters of all best-performing models are investigated for plausibility, from which the scenario with an inhibitor-affected induction signal and threshold comes out as most consistent.

The [Conclusion and Future Work](#) section gives a final overview of the findings with respect to the original research questions and re-contextualises the studies with regard to recent scientific advancements. Some application prospects of the presented models beyond the scope of the thesis are highlighted, future steps are proposed to improve the developed framework, and an illustration is given of some more sophisticated research endeavours that can be pursued through possible model extensions.

Chapter 2

Literature Review

2.1 The *Aspergillus* genus

2.1.1 Description

Moulds of the genus *Aspergillus* are ubiquitous in our environment and have a multi-faceted relationship with human societies. Some of these fungi can be pathogenic to animals and plants, colonising lung tissues, secreting mycotoxins and suppressing immune response by masking detectable components of their cell wall [6, 7], thus causing e.g. variants of aspergillosis in immunocompromised people. Additionally, the abundance and resilience of *Aspergillus* spores contribute to food and feed spoilage, which is of critical importance for the food industry [1, 8]. On the other hand, the metabolic processes of *Aspergillus* spp., most notably in *A. niger*, *A. oryzae* and *A. tereus* have long been utilised for the industrial production of useful substances for the biochemical and food industry: organic acids such as citric acid, itaconate and galactarate [9], enzymes like oxidases, phytases, glucoamylases [10], chitinases [11] and other secondary metabolites such as malate and lovastatin [9]. Due to their enzymatic production, species of the genus are furthermore used in fermentation processes. For example *A. oryzae* plays a vital role in the production of soy sauce and miso [12]. The use of *A. nidulans* as a model organism in genetic research and cell biology has elucidated phenomena significant for the understanding not only of aspergilli and related filamentous fungi, but of eukaryotic organisms as a whole [13].

The signature characteristic of *Aspergillus* fungi is the structure of their conidiophore — the specialised hyphal stalk carrying the asexual spores of the fungus, the conidia. Its resemblance to an asperges, a device used for sprinkling holy water during Catholic liturgies, designates the name of the genus [13]. With about ten thousand spores carried

by a conidiophore [14], an *A. niger* colony can produce more than a billion conidia [4], which are dispersed in the environment with varying efficiency through three primary vectors: air currents, water droplets and animal carriers, in particular the hydrophobic surfaces of insect bodies [14]. Once the conidium settles into a suitable medium, it can germinate.

2.1.2 The role of heterogeneity

Like many other filamentous fungi, aspergilli have acquired their ecological niche by evolving various survival mechanisms that increase their stress resistance and chance of propagation. These are generally rooted in a significant heterogeneity expressed at multiple stages of their development. As a most trivial example, differences can be observed in the sizes of conidia — $5.3 \pm 0.6 \mu\text{m}$ for *A. niger* [15], from 2.4 to $2.7 \mu\text{m}$ for *A. nidulans* [16], from 2 to $3.5 \mu\text{m}$ for *A. fumigatus* and from 3 to $6 \mu\text{m}$ for *A. flavus* [17].

As the fungus grows into a more complex morphology, a rich variety in form and function is revealed. A functional diversity in spatially differentiated zones of the vegetative mycelium has been confirmed by gene expression analysis [18–20] and attributed to epigenetic adaptations [21]. This is accompanied by a morphological heterogeneity in the sizes and shapes of mycelial microcolonies, ranging from dispersed mycelia to loose clumps and structured pellets [15, 22]. The causes for these differently self-organised structures can be traced back to the density and the composition of the spore inoculum, with lower spore densities leading to radially structured hyphal pellets and higher densities resulting in large colonies of dispersed mycelia [15, 23]. A primary mechanism in this heterogeneous morphological development is the aggregation of spores and hyphae through coagulative interactions [15, 22, 24], accompanied by an asynchronicity in the timing of the conidial germination [3], partly explained by the varying degrees of maturation of the spores as they disperse from the conidiophores [14]. At the same time, the germination percentage of the spore ensemble varies depending on environmental stimuli, with different germination rates exhibited upon changing the chemical components of the medium [3, 4]. Since hyphae do not have the stress resistance of conidia, it is suggested that the emergent regulation of the germination incidence through a heterogeneous environmental response is part of a bet-hedging mechanism, a finely tuned evolutionary strategy that secures a reserve of resistant dormant spores in case of unfavourable environmental changes [3, 25].

All of these adaptation techniques have a direct impact on the biochemical productivity or virulence of *Aspergillus* fungi and can be exploited in their industrial utilisation, e.g. for control of their rheological properties [15, 22, 23], or for targeted prevention of their harmful effects [26]. As the inoculation stage both allows for external control and largely

determines the later growth of the fungus, a research focussed on the pre-germination stage of coidia can capture essential principles before the physiological variation of the spores causes a greater divergence. Thus, the inherent heterogeneity of the spores can be combined with deterministic models to explain the experimentally observed germination statistics.

2.2 Conidial germination

2.2.1 Germination phases

The transition of *Aspergillus* conidia to vegetative mycelium is characterised by several distinct phases. A dormant spore, as it inoculates the new environment, has a rigid, hydrophobic, multi-layered cell wall [6] which confers the spore its ability to withstand high thermal and oxidative stress, resist osmotic pressure, dehydration, UV light and fluctuations in pH levels [27]. This dormant state can preserve the fungus in unfavourable conditions for over a year [28], before germination marks its transition from a fermentative to a respiratory metabolism and exchanges its high resistance for a more vulnerable but vegetatively active regime [27].

The activation of dormant conidia becomes evident through the onset of isotropic growth (the swelling phase), during which the diameter of the spore doubles its size, as water is taken up and the cell wall engages in a restructuring procedure. Compatible solutes like trehalose and mannitol, vital for the long-term resistance of dormant conidia, become degraded, along with the dense protective outer layer of the cell wall, consisting of rodlet proteins [27]. This prominent structural change in the conidium has been observed between 2 and 6 hours from inoculation in *A. niger* conidia [15, 29]. After the isotropic swelling phase, a polarity axis is established through the deposition of cortical markers, leading to the targeted transport of vesicles and key proteins and resulting in the protrusion of a germ tube [27]. Thus, the fungus enters its polarised growth phase.

2.2.2 Factors for germination

While the metabolic pathways leading to the break of conidial dormancy have yet to be mapped in satisfactory detail, it is known that specific sensing mechanisms enable conidia to adjust their germination response to the presence of nutrients in the medium. The specific combination of carbon, nitrogen and inorganic salts has been observed to elicit different responses in terms of germination percentage [4]. Glucose and amino acids

are typical nutrition components consumed by filamentous fungi in their natural environments as part of their saprotrophic lifestyle. As different mould species occupy distinct environmental niches, their susceptibility to specific amino acids varies, with alanine and proline being the highest-inducing carbon source shared among most *Aspergillus* species [3], leading to a nearly complete germination of the inoculum.

The mechanism through which carbon signals trigger the break of dormancy has only been partly understood so far. One carbon source sensor identified in conidia is the heterotrimeric G-protein signalling system, which activates the cAMP-PKA pathway in response to glucose and sets early processes of germination in motion [27, 30, 31]. Other components of environmental sensing include Ras proteins [32] and the Calcineurin pathway [27]. The functioning and coordination of these pathways is a topic of ongoing research, but current knowledge outlines a complex network of dependencies.

It has been found that the germination of a spore is not merely a consequence of an activating trigger, but rather an interplay between environmental stimuli and inhibitory signals. The mutual germination blocking of conidia from different or identical species becomes evident when observing how the inoculum density affects the percentage of germinated spores. In prior experiments with *A. niger* conidia, an increase of the spore count from 5000 to 40000 per 150 µL suspension has led to a decrease of the germination incidence of about 20% in media using alanine, proline and arginine as carbon sources [1]. In general, a reduction of the germination percentage has been documented at conidial densities higher than 10^5 spores/mL [2, 33], the consequences of which reflect in the subsequent morphological development and productivity of the mycelium [23]. The decrease in germination occurrences cannot be explained by a competition for nutrients, since the carbon sources primarily have a signalling role and are not consumed during the dormant conidium phase [1]. While there may exist other germination-determining scarcities at crowded inoculi, e.g. of O₂ and CO₂ [34], a likely factor is the increased concentration of an auto-inhibitor produced by the spores themselves.

2.3 Germination inhibitor

2.3.1 Volatile organic compounds

Volatile organic compounds (VOCs) are a broad class of small, heat-stable molecules known to enable communication between organisms and across kingdoms, e.g. as means of attraction, warning or repulsion [35, 36]. Their low molecular weight (50-300 Da) and high vapour pressure at ambient conditions make them highly diffusible, conferring their potential to reach molecular receptors at considerable distances within a short

time. If a spore times its own germination through the slow release of a such a self-inhibitory compound, then it would also inhibit the germination of nearby spores at high densities, producing a so-called “crowding effect”. It has been proposed that such a mechanism prevents premature germination within the conidiophores, where spores are packed densely, delaying the break of dormancy until dispersal [37].

VOCs, in particular 8-carbon (C-8) oxylipins, have been found to accumulate in the headspace of *A. oryzae* [38] and *A. flavus* [39]. These include 1,3-octadiene, 1,5-octadien-3-ol, 1-octen-3-ol, 3-octanone, octanal, 2-octenal, 1-octanol; and 2,4-octadienal. Among these, 1-octen-3-ol has proven to have the strongest inhibitory effect on germination in *A. nidulans*, followed by 3-octanone and 3-octanol [2]. These are also the three primary compounds identified in solvent extractions from the medium of the fungus. In *A. oryzae*, the dominant headspace VOCs are 1-octen-3-ol, 2-octenal and 3-octanone [39]. Using a freeze-thaw cycle to destroy the integrity of the cell membrane, a substantial release of 1-octen-3-ol has been observed in *A. flavus* conidia as well, followed by 3-octanone, 2-octen-1-ol and 1-octen-3-one [5].

2.3.2 1-octen-3-ol

1-octen-3-ol is a secondary alcohol and a flavour compound in mushrooms. Along with 3-octanone and 3-octanol, it is produced by the oxygenation and breakdown of linoleic acid [2]. 1-octen-3-ol was first recognised as a primary germination auto-inhibitor in *Penicillium paneum*, a mould related to *Aspergillus* via the order *Eurotiales* [37]. When exposed to exogenous concentrations of 1-octen-3-ol (4 mM), dormant *P. paneum* conidia do not swell and swollen conidia do not germinate [37]. Evidently, the auto-inhibitor mildly increases the cell membrane permeability and transiently lowers the internal pH level of the conidia, which influences respiration and protein synthesis [40, 41]. At an inoculum density of 10^6 spores/mL, the germination rate for 1, 2.5, 4 and 5 mM added 1-octen-3-ol is measured at $83 \pm 8.1\%$, $35 \pm 6.3\%$, $13 \pm 2.1\%$ and $1 \pm 0.6\%$, respectively, against a no-inhibitor control experiment with $88\% \pm 5.3\%$ germination success.

Experiments with *A. nidulans* have shown that dormant conidia exposed to 4 mM also do not reach a swelling phase at the expected 4-hour mark and remain in their passive state until the end of the 16-hour experiment [2]. At an inoculum density of 10^5 spores/mL, added 1-octen-3-ol concentrations of 1, 2.5, 4 and 5 mM yield $87 \pm 6.1\%$, $36 \pm 4.3\%$, $14 \pm 2.1\%$ and $1 \pm 0.3\%$ germinated spores, respectively, against a no-inhibitor control experiment with $95\% \pm 5.3\%$ germination incidence. These results are quantitatively similar to the outcome of the experiments with *P. paneum*, suggesting that analogical mechanisms may be at play during the inhibition of *Aspergillus* spores.

The effects of 1-octen-3-ol on filamentous fungi are known to be reversible [2, 39, 40]. Thus, conidia blocked from germination can resume their break of dormancy once the ambient inhibitor concentration is lowered, e.g. when the spore is transferred to a less crowded environment.

2.3.3 Open questions

Although 1-octen-3-ol is recognised as an appropriate candidate for auto-inhibition in *Aspergillus* conidia, there is inconclusive evidence that it is as a sole primary endogenous factor in this process for all *Aspergillus* species. For instance, *A. niger* spores washed of superficial compounds also exhibit reduced germination under crowding [1]. A possible explanation for this is that the VOC is constantly produced or very tightly bound to the conidium [40]. Furthermore, experiments with *A. flavus* conidia have indicated that the threshold concentration for inhibiting germination is not less than 10 mM, while the quantity of 1-octen-3-ol released by spores, even after freeze-dry forcing, is below 1 μ M [5]. A concerted interaction with another potential inhibitor may paint a more complete picture. This could be one or several of the less prominent VOCs found in the headspace (such as 3-octanone). Alternatively, some studies point at the role of a heat-labile peptide, indicated by the loss of auto-inhibition after a heat-treatment of the conidia [5]. However, a thermal instability would imply a considerable molecular size, which has implications on the diffusion rate and permeability through the cell wall of the dormant conidium.

A lightweight, volatile and thermodynamically stable molecule such as 1-octen-3-ol would clearly have radically different dynamics compared to a protein large enough to denature or break down under heat. This not only has implications for the diffusion of the inhibitor through the surrounding medium, but also affects its permeation through the layers of the cell wall. Therefore, to estimate the inhibitor release timing, the properties of the conidial envelope need to be carefully studied.

2.4 The conidial cell wall

2.4.1 Function and dimensions

The multi-layered, rigid cell wall of an *Aspergillus* conidium ensures its long-term viability, protects it against various stresses, enables its adhesion to surfaces, including those of other spores, masks it from immune response and forms a substantial screening barrier for signalling molecules such as nutrients or inhibitors [42]. While an exhaustive

comparison of the spore wall thickness and consistency in different *Aspergillus* species is difficult to obtain, documented measurements hint on a significant variance within and across species, strains and stages of development. For instance, transmission electron microscope (TEM) studies of *A. fumigatus* indicate a cell wall thickness of about 25 nm in 0.5-day old spores and 50 nm in 1-day old spores [43]. Meanwhile, coherent anti-Stokes Raman spectroscopy (CARS) of dormant *A. nidulans* conidia outlines a thickness range of 273-490 nm [44]. Apart from the likely physiological difference between the species, an underestimation of the true thickness by the TEM procedure is possible due to the dehydration of the samples, while the large variance in the CARS procedure can be traced to the indirect inference of the cell wall extent by employing spectral variations. A consensual assumption would be that the cell wall's thickness is in the order of a hundred nanometers in dormant conidia [45].

2.4.2 The inner cell wall layers

The cell wall structure is characterised by several distinct layers. The innermost zone remains mostly conserved through the vegetative transformations of the conidium and consists of glucans (71%), chitin (9%), mannan (6%) and galactan (13%), measured for *A. fumigatus*[46]. Furthermore, glycoproteins are estimated to constitute 20-30% of the cell wall dry weight in filamentous fungi [7]). A common structural molecule, chitin comprises folded molecules, forming a microfibril matrix that glucans and glycoproteins are cross-linked with [42]. Glucans are polysaccharides of different molecular species found in great abundance in the cell wall. A general categorisation distinguishes these as α - and β -glucans. The β -(1,3)-glucan forms long molecules that extend throughout the cell wall and covalently bind to other components. It thus forms a rigid structural network that provides mechanical strength and a scaffold for galactomannan, melanin and other compounds [6, 42, 47]. Being a characteristic molecule in fungi, β -(1,3)-glucan is recognised by receptors such as Dectin-1 in humans, necessitating the evolutionary adaptation of some fungi to mask it via α -(1,3)-glucans [42, 48] — molecules constituting about 19% of the cell wall polysaccharides in *A. fumigatus* [48]. The biosynthesis, organisation and maintenance of the polysaccharides and other connected structures occurs to a great extent within the cell wall itself, enabled by transglycosidases and yapsin orthologs [42, 49]. These are an example of the various GPI-anchored proteins tethered to the cell membrane, which along with the glycoproteins freely embedded in the cell wall matrix serve re-structuring, environmental sensing and transportation functions.

2.4.3 The outer cell wall layers

The outer layer of the cell wall is the region that undergoes the most significant transformation during the break of dormancy and the consequent onset of hyphal growth. One of its major components during the dormant conidial stage is the mechanically resistant and highly insoluble hydrophobin layer, a tightly packed structure of RodA proteins that group in parallel fascicles to form long amyloid-like structures of about 10 nm thickness [50, 51]. The amphipathic behaviour of Class-I hydrophobin molecules enables them to self-assemble at hydrophilic-hydrophobic interfaces [52] and form bilayers when in isolation [51]. The resulting rigid hydrophobic barrier between the spore and its environment ensures its long-lasting protection against stresses and immune system response [50, 52], while selectively permitting molecular transport through its structure. As the outermost component of the cell wall, hydrophobins also contribute to the adhesion of spores and thus to their agglomeration and virulence [42, 53].

Interacting with the hydrophobin layer and cross-linking with the inner regions of the cell wall is a layer of dihydroxynaphthalene (DHN) melanin, a negatively charged and hydrophobic pigment that plays an integral role in the structural assembly of the conidial wall layers [54] and confers the spore its resilience against UV radiation, heat stress and toxins, further enhancing its viability [7, 55].

While being highly insoluble and chemically resistant to outside influences, the outer layer undergoes a programmed degradation by aspartic proteases upon the break of conidial dormancy [27, 56], removing the rigid rodlet structure to give way to the vegetative expansion of the spore. Thus, the protective coating of the spore has its most substantial barrier function in the early period prior to germination.

2.5 Conidial aggregation

The outer cell wall layer of *Aspergillus* conidia has adhesive properties, enabling e.g. spores of *A. fumigatus* to attach to epithelial host cells [57]. Furthermore, electrostatic and salt bridging between spore surface polysaccharides and hydrophobic interactions of surface proteins give rise to spore agglomeration and a subsequent coagulative pellet formation in *A. niger* [15]. This process appears correlated with the onset of conidial swelling in germination-inducing media [58]. The conidial aggregates are heterogeneous in size, possibly as a way to diversify survival strategies [22]. An inquiry into the distributions of spore counts within aggregated clusters yields varying results depending on the inoculum density, strain used, method of cultivation and measurement technique [15, 24, 59]. Nonetheless, the observations show that spore agglomeration consistently

occurs within the first hour from inoculation, followed by a slight breakage of the clusters, possibly from the stress induced by swelling spores and growing germ tubes [15].

2.6 Diffusion

2.6.1 The diffusion constant

Diffusion is a process of fundamental importance in nature, arising from the spatially and temporally uncorrelated Brownian motion of particles driven by thermal kicks [60]. Fick's laws of diffusion [61] lay the physical framework for the statistical description of this phenomenon and give rise to mathematical relationships fundamental to scientific modelling. According to these, the flux of particles follows a direction from a higher to a lower concentration, during which their total mass in the system is conserved [60]. The mathematical formulation of these principles can be used to quantify the relationship between time and the mean squared displacement of a diffusing molecule [62], expressed through the *diffusion constant* D , measured in units of area per time. This measure can be obtained experimentally or inferred through other characteristic properties of the diffusing substance and its surrounding medium.

2.6.2 The permeation constant

The permeation of molecules through a barrier is closely related to diffusion and is a highly relevant phenomenon in biological systems, where interfaces like membranes define distinct spatial compartments. Most generally, semi-permeable barriers represent heterogeneities in the medium of diffusion, where the diffusion constant is altered locally due to a less accessible region [63]. The relationship between the diffusion constant of the particle-barrier system and the specific geometry and interface type of the barrier is captured by the *permeation constant* P_s , measured in units of speed [60]. This relationship includes different parameters depending on the choice of barrier model.

In the pore-flow model [64], permeation can be viewed as one-dimensional migration of particles along capillary channels of the barrier due to molecular interactions [60]. This approximation is representative of porous barriers, the passage through which is limited by the size and tortuosity of its permeable cavities. In this case, P_s is dependent on the fraction of the surface area occupied by the pores [60, 65].

If the cavities of the barrier are within the molecular scale, as is the case of biological membranes, the diffusing substance can still permeate through its hydrophobic-hydrophilic interaction at the barrier interface [66]. In this so-called solution-diffusion

model, the diffusing substance is assumed to partition into the barrier as a solute [64]. Thus, the permeation constant is dependent on the *partition coefficient* for the given system: an equilibrium constant denoting the stable-state ratio of the compound concentrations in a mixture of the barrier and non-barrier medium. Most commonly, this is the octanol-water partition coefficient K_p , applicable for lipid membranes in an aqueous environment [67], but also recognised as useful in approximating other types of membranes [68]. A further extension of this theory differentiates the permeabilities of the different structural layers of the lipid membrane [69].

2.6.3 Estimating the diffusion and permeation constants

The quantification of diffusion and permeability is essential in studying how a molecular signal diffuses through the cell wall into and out of the spore. In the case of dormant conidia, this includes the passage through an aqueous medium, the hydrophobin-melanin layer of the cell wall, the inner polysaccharide-rich cell wall and the cell membrane.

While the volatility of 1-octen-3-ol makes it difficult to study its diffusion coefficient experimentally, one can approximate it via the Stokes-Einstein relation,

$$D = \frac{k_B T}{\zeta}, \quad (2.1)$$

using the Stokes radius a of the diffusing particle and the viscosity η of the medium, which collectively determine the friction coefficient $\zeta = 6\pi\eta a$ for spherical approximations of the molecule [60]. Alternatively, available data on molecules of a similar size can be used. Glucose is a widely studied compound with only a slightly larger molecular mass (180.16 g/mol, compared to 128.21 g/mol of 1-octen-3-ol), which diffuses in water with a constant $D = 6 \times 10^{-6} \text{ cm}^2 \text{ s}^{-1}$ [70]. Experiments with various proteins indicate diffusion coefficients similarly in the order of $10^{-7} - 10^{-6} \text{ cm}^2 \text{ s}^{-1}$ [71, 72].

Hydrophobins, of which Class I form stable rodlet structures and Class II aggregate into semi-soluble assemblages [52, 73], are found in various fungal species, with Class I being characteristic for *Aspergillus* members (RodA in *A. nidulans* and HYP1 in *A. fumigatus*) [73]. In-vitro, SC3 hydrophobins, members of Class I and characteristic for the *Schizophyllum commune* fungus, have been observed to form membranes with very selective permeability, blocking the passage of particles heavier than 200 Da (roughly equivalent to 0.8 nm) [74]. Artificial bilayers from HFBI hydrophobins (members of Class II), commonly found in *Trichoderma reesei*, have exhibited a very low permeability for water [75]. Thus, assuming this permeability is preserved in the outer cell wall complex, both classes can impose a considerable barrier for molecules entering and exiting

the spore. This implies that the passive diffusion of large proteins would effectively be blocked. While self-assembled hydrophobin bilayers may obey the solution-diffusion principle, their structural configuration in the outer cell wall may exhibit discontinuities and be more akin to a porous mesh, as some microscopic images suggest [76].

The lack of data on the diffusivity of the separate cell wall components also requires the use of molecular analogues to estimate sensible permeability ranges. For example, agarose, commonly used as a growth substrate, can be regarded as a more loosely-structured representative of the polysaccharides. For glucose in an agarose film, a $D = 6.46 \times 10^{-6} \text{ cm}^2 \text{ s}^{-1}$ has been estimated and referred to a $D = 7 \times 10^{-6} \text{ cm}^2 \text{ s}^{-1}$ of glucose in water [77]. A much more rigid and structured polysaccharide, cellulose, yields a low diffusivity in comparison: finite-element studies of glucose diffusing in cellulose nanofibril peripheral nerve conduits indicate $D \approx 1.7 \times 10^{-7} \text{ cm}^2 \text{ s}^{-1}$ [78]. A study related to the food industry has obtained a diffusion coefficient of 1-octen-3-ol in deuterium water (D_2O) of roughly $8 \times 10^{-6} \text{ cm}^2 \text{ s}^{-1}$ and in agar gel of 2×10^{-6} to $6 \times 10^{-6} \text{ cm}^2 \text{ s}^{-1}$, depending on the measurement method. Due to its heavier molecule, D_2O has about 125% the viscosity of normal water [79], which implies that the Stokes-Einstein relation (Equation 2.1) would lead to a diffusion coefficient of 1-octen-3-ol in water of about 2.5×10^{-6} to $7.5 \times 10^{-6} \text{ cm}^2 \text{ s}^{-1}$, a result aligning closely with the diffusivity of glucose in water.

The permeability of lipid bilayers is an extensively studied subject. Water molecules have been found to permeate through cell membranes with a P_s of 3×10^{-10} to $7 \times 10^{-3} \text{ cm s}^{-1}$ [80]. The permeation constant of glucose through a synthetic membrane of L- α -dipalmitoylphosphatidylcholine (DPPC) has been estimated at $P_s \approx 1.4 \times 10^{-10} \text{ cm s}^{-1}$ [81]. Another estimate indicates $P_s = 2.4 \times 10^{-10} \text{ cm s}^{-1}$ for glucose permeating a synthetic lipid bilayer [82]. The same source also notes that natural lipid membranes exhibit a significantly higher permeability for glucose, facilitated by glucose transporters (GLUT1). A similar mechanism, however, has not been described for VOCs.

The complex structure of the conidial cell wall and its transformation during the germination phases make the quantification of an effective cell-wall encompassing permeation coefficient difficult, but some insight can be gained from experimental studies. Results from fluorescent staining of conidia of filamentous fungi like *A. niger* and *A. nidulans* with fluorescein isothiocyanate (FITC) dextran indicate that a spore in the process of germination can take up particles of weight 150 kDa (Stokes radius of about 8 nm) [83], a very high upper limit that well encompasses potential heat-labile peptides. However, in their dormant phase, the conidia are heterogeneously stained, indicating that not all FITC-dextran molecules can pass through the cell wall barrier. Since the smallest mentioned molecule of the viability dye in the study is 10 kDa, the maximum permissible

molecular size for cell walls of dormant conidia could fall anywhere within the range of 10 to 70 kDa (Stokes radius of 2.3 nm and 6.0 nm, respectively).

Several other factors may obstruct the passive diffusion of molecular signals between spores. First, considering the extracellular medium of conidial clusters, the question arises whether the interiors of conidia become significant excluded volumes for the molecular paths in the medium, especially in tightly packed clusters. The presence of immobile obstacles in the spatial domain of diffusing particles is known to produce anomalous diffusion [84]. While the diffusivity within dormant spore clusters has not been studied extensively, research indicates that the pellet cores formed by such clusters are generally oxygen-depleted [85], suggesting that crowding imposes barriers for diffusion. Returning to the molecular scale, an additional diffusion-limiting factor could be the strong interaction of the permeating particle with the cell wall matrix, leading to temporary bonds that slow down the molecular passage in a non-trivial way.

2.7 Adsorption

While permeation models capture the principles of passive diffusion, they consider at most polar interactions between the permeating molecule and the barrier. However, when passing through the porous polysaccharide matrix, molecules may form covalent bonds and become transiently embedded in the cell wall. It has been shown that ions of heavy metals can be adsorbed by *Aspergillus* fungi [86], in particular through their α -glucans [87]. Such adsorption capacity has also been proven for industrial pollutant VOCs like α -pinene, n-hexane and ethyl acetate [88]. Most notably, a study has quantified the adsorption of 1-octen-3-ol by yeast glucans obtained from the cell wall [89]. A commonly used model in this case is the Langmuir isotherm, based on the binding kinetics of a molecular species to a matrix with a finite adsorption capacity [90]. While there is strong evidence for the interaction of glucans with ions and VOCs, highlighting fungi as promising biosorbents of off odours and pollutants, such behaviour has not been documented with regard to glucose or amino acids, suggesting that adsorption plays a stronger role in the inhibitor release rather than in carbon signalling.

2.8 Modelling

Computational models addressing diffusivity in fungal colonies have mostly focussed on the vegetative mycelium — a phase with macroscopically observable morphological characteristics. Techniques such as microscopic image processing [15, 91] and X-ray microcomputed tomography [92] have been used to capture spatio-temporal data against

which hyphal growth models can be tested, elucidating relationships between the topology, morphology and chemical productivity of the mycelia through simulations [92–95]. While hyphal growth dynamics have been studied on a variety of scales [96], only a few models relate these to germination mechanisms. For example, the onset of polarised growth in a swelling spore is captured by a classical lattice-based model [97] that reinforced the understanding of the role of the Spitzenkörper in hyphal tip growth [98].

Attempts at modelling germination have, in contrast, had a stronger focus on statistical descriptions rather than spatial representations. For instance, the germination percentage of spores over time is commonly predicted by sigmoidal functions fitted over experimental data points [99, 100]. The benefit of these models is that they provide descriptive indicators for germination under specific environmental conditions, such as the saturation percentage of germinated spores (p_{\max}) and a characteristic germination time (τ_g) in the model by Dantigny et al. [100]. Nonetheless, the models are primarily based on phenomenological observations and are not necessarily derived from first principles.

Contrary to this, the mathematics of diffusion has steady foundations in statistical physics [60, 101] and has been extensively explored in computational biology models as a driving force in morphogenesis [102], growth [103] and chemical signalling [104]. Therefore, highlighting the effects of diffusion in germination inhibition can help discern universal laws and dependencies in an otherwise highly heterogeneous system.

Inhibitory kinetics have long been modelled on a molecular level using modified variants of the Michaelis-Menten equation [105]. The formulas reflect the rate and saturation levels of inhibitors binding to a substrate and can incorporate different reaction scenarios, depending on whether the inhibition is competitive, uncompetitive or non-competitive [106]. While such models have a practical use in the pharmaceutical industry, the pathways of inhibition in conidial germination are likely more complex and cannot be fully captured by the mass-action principles behind Michaelis-Menten models.

The quantitative modelling of conidial agglomeration, a primary factor in defining obstacles for diffusion in the dormant spore phase, is still in its infancy, with some attempts being made at describing the kinetics of spore aggregation [24]. Meanwhile, inspiration can be drawn from related stochastic phenomena such as Brownian coagulation [107] and disordered sphere packings [108].

Chapter 3

Methods

10-15 pages

3.1 General assumptions

The focus of this research is narrowed down to a time frame of the conidial life cycle in which relatively few structural changes take place and the spore retains a relatively constant volume and cell wall consistency. Therefore, a spore is considered to germinate as soon as it enters its swelling stage, which marks the onset of cell wall restructuring. The initiation of germination is viewed as a binary decision process which takes place when the inhibitor concentration falls under a threshold or when the inducing signal surpasses a threshold. The models first focus on the process of inhibitor release in greater detail, arguing that some of the logic can be applied to the case of inducer permeation by reversing the direction of the concentration gradient.

It is considered that the germination-determining signals are conducted by singular molecular species (i.e. not mixtures of different compounds) which propagate via passive diffusion. This implies direct molecule-to-molecule interactions and excludes extracellular transport via vesicles or uptake facilitation by transporter proteins. The extracellular medium which surrounds the spores is assumed to contain water, although its diffusive properties could also apply to agarose, as indicated in the [Literature Review](#).

In most of the presented models, a conidium is approximated by a sphere, with its cell membrane and the different layers of its cell wall represented by spherical shells within the spore volume. This allows for the application of spherical geometry properties in many of the calculations. In many-spore simulations, it is assumed that the spores are homogeneously distributed in an infinite volume. When addressing the number of conidia

per unit volume, the term used in the text is *spore density*, which is meant to avoid the notion of *concentration*, generally used for molecular species. It is not to be confused with the material density of an individual spore.

3.2 Mathematical foundations

First, a mathematical description of the main physical concepts used in the modelling process is laid out: diffusion as the driving mechanism in the extracellular medium, permeation as its derivative process across the spore interface and adsorption as a diffusion-decelerating phenomenon.

3.2.1 Diffusion

A molecule can be considered a point in space with a positional vector \vec{r} . Using the abstraction of a diffusing particle as a “random walker” in three-dimensional space, the mathematics of diffusion can be derived from the statistical analysis of its motion [60, 109]. By definition, this motion is uncorrelated in time and space. The mean squared displacement of the particle, $\langle |\vec{r}|^2 \rangle$, is linearly related to the time t via the diffusion constant D as $\langle |\vec{r}|^2 \rangle = 6Dt$ [62]. The constant D , measured in m^2/s , thus characterises the ease with which a specific molecule migrates through a specific medium, and can be related to properties like the molecular size of the diffusing particle and the viscosity of the medium (see the Stokes-Einstein relation in Equation 2.1) [60]. Fick’s first law states that the particle flux J through an infinitesimal volume in space follows a direction from the region of higher concentration to that of lower concentration, tending to reduce or “smooth” the concentration gradient. This is expressed by the equation

$$J = -D \frac{\partial c}{\partial x}, \quad (3.1)$$

where c is the concentration of the diffusing substance and x is a spatial coordinate. The second law of diffusion is based on the mass conservation principle, stating that no quantities of the substance can be created or destroyed. It takes the form of the continuity equation

$$\frac{\partial c}{\partial t} + \frac{\partial}{\partial x} J = 0 \quad (3.2)$$

and, combined with Equation 3.1, yields the relationship between the time and space derivatives of the concentration, constituting the *diffusion equation*:

$$\frac{\partial c}{\partial t} = D \frac{\partial^2 c}{\partial x^2}. \quad (3.3)$$

An intuitive reading of this formula is that the concentration gradient becomes smoother over time: the sign of its curvature, dictated by the second-derivative term on the right-hand side, drives a compensatory change of the concentration over time. Thus, any sharply localised concentrations gradually spread out, which is consistent with the equilibration of molecular systems toward high-entropy, i.e. a maximisation of the number of possible microstates [60].

3.2.2 Permeation

A similar equilibration principle applies to the concentrations of a substance on the opposite sides of a semi-permeable barrier. The flux J through the barrier is proportional to the difference Δc between the concentrations on the two sides of the barrier:

$$J = P_s \Delta c = P_s (c_{\text{in}} - c_{\text{out}}). \quad (3.4)$$

Here, c_{in} and c_{out} are the concentrations in the interior and the exterior delineated by the barrier, and P_s is the permeation constant measured in units of speed (m/s) [60, 67]. As the number of particles exiting the barrier from a volume V at a concentration c is proportional to the barrier surface area A , the following temporal evolution of the concentration drop can be derived [60]:

$$\frac{d(\Delta c)}{dt} = - \left(\frac{AP_s}{V} \right) \Delta c. \quad (3.5)$$

The reciprocal of the prefactor on the right-hand side is commonly denoted as $\tau \equiv \frac{V}{AP_s}$. Since the solution of this ordinary differential equation (ODE) is commonly of the form

$$\Delta c(t) = \Delta c(0) e^{-t/\tau}, \quad (3.6)$$

τ represents a characteristic relaxation time for the concentration difference across the barrier. The dependence of the effective permeability on the surface-to-volume ratio (as indicated in Equation 3.5) has been confirmed experimentally [110].

The permeation constant may have different physical interpretations depending on the model of the observed system. In the pore-flow model [64], P_s is dependent on the fraction α of the barrier surface occupied by pores [60, 65]:

$$P_s = \frac{\alpha D}{d}, \quad (3.7)$$

where d is the thickness of the barrier.

In the solution-diffusion model, commonly applying to lipid bilayers, the diffusing substance is assumed to partition into the barrier [64]. In this case, the Meyer-Overton rule relates the permeation and diffusion constants [67]:

$$P_s = \frac{K_p D}{d}. \quad (3.8)$$

The right-hand side involves the octanol-water partition coefficient K_p , an equilibrium constant denoting the stable-state ratio of the compound concentrations in a mixture of a lipophilic and an aqueous solvent. K_p thus indicates the lipophilic vs. hydrophilic preference of the diffusing molecule.

Finally, if the diffusion constant itself is unknown, α and K_p can be absorbed into an *effective diffusion constant* D_{eff} , yielding

$$P_s = \frac{D_{\text{eff}}}{d}. \quad (3.9)$$

Following Equation 3.5, the evolution of the concentration drop across the barrier can be simulated over time for a specific P_s . Conversely, one can impose the boundary condition that the concentration drop at a specific time, $\Delta c(t)$, should be a fixed value, then estimate the needed permeation constant for such a decrease. This way, one can either examine the likeliness of a given material system to reproduce certain inhibitor release dynamics or infer the permeability of an unknown material system given the release timing.

3.2.3 Adsorption

If the inhibitor molecules strongly interact with the cell wall, e.g. with the hydrophobic or polysaccharide networks, their effective permeation incorporates the release deceleration due to temporary retention in an adsorption matrix. The adsorption process can be

described as a reaction between an inhibitor I and a binding site S to a bound complex IS :



The reaction kinetics are governed by the adsorption and desorption constants k_{on} and k_{off} . Separating the concentration of inhibitor in the cell wall into a concentration of bound and of unbound inhibitor (q and c_{free} , respectively), the concentration of available (unbound) sites is $B_{\text{max}} - q$, where B_{max} is the maximum binding capacity in mol of binding sites per unit volume. The rate equation for q is then

$$\frac{\partial q}{\partial t} = k_{\text{on}} c_{\text{free}} (B_{\text{max}} - q) - k_{\text{off}} q. \quad (3.11)$$

Assuming that the binding and unbinding equilibrate quickly compared to the cell wall permeation, the steady-state ($\frac{\partial q}{\partial t} \approx 0$) is given by

$$k_{\text{on}} c_{\text{free}} (B_{\text{max}} - q_{\text{eq}}) = k_{\text{off}} q_{\text{eq}}. \quad (3.12)$$

The solution for this equation is the Langmuir isotherm [90]

$$q_{\text{eq}} = \frac{B_{\text{max}} K_{\text{eq}} c_{\text{free}}}{1 + K_{\text{eq}} c_{\text{free}}}, \quad (3.13)$$

where $K_{\text{eq}} = \frac{k_{\text{on}}}{k_{\text{off}}}$ is an equilibrium constant. As long as $K_{\text{eq}} c_{\text{free}} \ll 1$, i.e. the binding affinity is not strong enough to cause saturation of bound sites, the linear approximation

$$q_{\text{eq}} \approx B_{\text{max}} K_{\text{eq}} c_{\text{free}} \quad (3.14)$$

can be made. Thus, following the mass conservation law, the inhibitor diffusion in the cell wall follows the dynamics

$$\frac{\partial c_{\text{cw}}}{\partial t} = \frac{\partial}{\partial t}(q + c_{\text{free}}) = D \frac{\partial^2 c_{\text{free}}}{\partial t^2}, \quad (3.15)$$

where only c_{free} diffuses freely according to Fick's laws. Thus,

$$(1 + B_{\text{max}} K_{\text{eq}}) \frac{\partial c_{\text{free}}}{\partial t} = D \frac{\partial^2 c_{\text{free}}}{\partial t^2}, \quad (3.16)$$

$$\frac{\partial c_{\text{free}}}{\partial t} = \frac{D}{1 + B_{\max} K_{\text{eq}}} \frac{\partial^2 c_{\text{free}}}{\partial t^2}. \quad (3.17)$$

It becomes evident that the diffusion constant is replaced by an effective diffusivity modulated by adsorption:

$$D_{\text{ad}} = \frac{D}{1 + B_{\max} K_{\text{eq}}}. \quad (3.18)$$

Assuming that $D \equiv D_{\text{eff}}$, this can be translated to an adsorption-dependent permeation constant:

$$P_{\text{ad}} = \frac{D_{\text{ad}}}{d} = \frac{D_{\text{eff}}}{d} \frac{1}{1 + K_{\text{eq}} B_{\max}}, \quad (3.19)$$

$$P_{\text{ad}} = \frac{P_s}{1 + K_{\text{eq}} B_{\max}}. \quad (3.20)$$

Conversely, knowing the material-specific permeation constant of the particle through the cell wall, P_s , the product of the adsorption parameters can be expressed as

$$K_{\text{eq}} B_{\max} = \frac{P_s}{P_{\text{ad}}} - 1. \quad (3.21)$$

Thus, discrepancies between the material-informed permeation constant (resulting from the molecular properties of the inhibitor and the barrier) and the model-informed permeation constant (estimated for a specifically timed inhibitor release) can be related to plausible K_{eq} and B_{\max} found in literature.

3.3 Computational models

There are two kinds of computational models constructed from the preceding mathematical theory: numerical ones, which simulate diffusion in an iterative manner, and analytical ones, which directly compute the concentrations of diffusing substances at points in time based on mathematical dependencies. The benefit of the former is that the solution process is intuitive and inherently evolving in time, analogous to actual diffusion. The benefit of the latter is that it does not require long simulations but rather involves a single evaluation of a mathematical expression for a given point in time. This section describes the approaches used in the numerical solvers and the derivation of

the saturation-sensitive extension of the analytical permeation formula. The quantity of interest is the residual concentration of inhibitor inside the spore at a time t . After presenting the specifics of each model, the setup for their mutual validation and verification by a comparative test with an exemplary set of parameters is laid out. The final subsection reveals the technical details of the algorithmic implementation in Julia.

3.3.1 Numerical models: general considerations

The numerical models are set up to solve the diffusion equation (Equation 3.3) on a finite space and time domain, discretised in regular intervals. An essential decision in the early stage of this setup concerns the dimensionality of the spatial domain. While a two-dimensional lattice in space requires significantly less computation and could well represent a section in three-dimensional space in very symmetrical setups, several considerations make it inconvenient to work with. First, particles inherently diffuse slower in lower-dimensional space (in 2D, $\langle |\vec{r}|^2 \rangle = 4Dt$ [62]), meaning that a correction of the results would be necessary. Second, even if a specific scenario is assumed in which the spores occupy a medium mostly extending in two dimensions (e.g. a thin film), this would hinder the generalisability of the model to most practical applications. Therefore, a more computationally expensive three-dimensional lattice is used at the cost of a looser set of assumptions.

To simulate diffusion over time, the multi-dimensional formulation of the diffusion equation,

$$\frac{\partial c}{\partial t} = D \nabla^2 c, \quad (3.22)$$

needs to be brought to a form that can be iteratively solved. First, the Laplacian term be expressed as partial second-order derivatives along each spatial coordinate:

$$\frac{\partial c}{\partial t} = D \left(\frac{\partial^2 c}{\partial x^2} + \frac{\partial^2 c}{\partial y^2} + \frac{\partial^2 c}{\partial z^2} \right) \quad (3.23)$$

The equation can be solved numerically using a finite-difference approximation [111]. To this end, the concentration measured a small step forward and backward from a reference point x along a spatial coordinate is expressed as a Taylor series:

$$c(x + \delta x) = c(x) + \delta x \frac{\partial c(x)}{\partial x} + \frac{\delta x^2}{2} \frac{\partial^2 c(x)}{\partial x^2} + \mathcal{O}(\delta x^3) \quad (3.24)$$

$$c(x - \delta x) = c(x) - \delta x \frac{\partial c(x)}{\partial x} + \frac{\delta x^2}{2} \frac{\partial^2 c(x)}{\partial x^2} - \mathcal{O}(\delta x^3) \quad (3.25)$$

Disregarding the higher-order terms, these two equations are summed to express the second derivative:

$$\frac{\partial^2 c(x)}{\partial x^2} \approx \frac{c(x + \delta x) + c(x - \delta x) - 2c(x)}{\delta x^2} \quad (3.26)$$

Taking a small step forward in time, a similar approach can be applied to the first-order derivative with respect to time.

$$c(t + \delta t) = c(t) + \delta t \frac{\partial c(t)}{\partial t} + \frac{\delta t^2}{2} \frac{\partial^2 c(t)}{\partial t^2} + \mathcal{O}(\delta t^3) \quad (3.27)$$

This equation can be rewritten to derive a finite-difference approximation for $\frac{\partial c(t)}{\partial t}$:

$$\frac{\partial c(t)}{\partial t} \approx \frac{c(t + \delta t) - c(t)}{\delta t} \quad (3.28)$$

The finite-difference approximations can be substituted in Equation 3.23 to obtain a discretised form of the equation. Given an orthogonal lattice with uniform spacing δx in each dimension, and iterating through time with a step δt , the discrete spatial sites are indexed by i, j and k , running from 0 to M , while the consecutive time steps are labelled by n , running from 0 to t_{\max} . Each lattice node communicates with 6 neighbours in a von Neumann neighbourhood [112]. Then the update rule for the concentration at each lattice site can be derived as follows:

$$\frac{c_{i,j,k}^{n+1} - c_{i,j,k}^n}{\delta t} = D \frac{\sum_{i'} \sum_{j'} \sum_{k'} c_{i',j',k'}^n - 6c_{i,j,k}^n}{\delta x^2}, \quad (3.29)$$

$$c_{i,j,k}^{n+1} = c_{i,j,k}^n + D \frac{\delta t}{\delta x^2} \left(\sum_{i',j',k'} c_{i',j',k'}^n - 6c_{i,j,k}^n \right), \quad (3.30)$$

where $i' \in \{i-1, i+1\}$, $j' \in \{j-1, j+1\}$ and $k' \in \{k-1, k+1\}$ are the neighbour indices with respect to the current site. This forms an *explicit, forward Euler scheme* for solving the diffusion equation. The boundary condition in all numerical models presented in this section is periodic, meaning that $c_{M+1,j,k} \equiv c_{0,j,k}$, $c_{i,M+1,k} \equiv c_{i,0,k}$ and $c_{i,j,M+1} \equiv c_{i,j,0}$. The consequences of this only become important once the diffusion radius around the spore reaches the limits of the spatial domain. For single-spore simulations, this implies

that N should be large enough for the ambient concentration not to become biased by the finite-size effect. For many-spore simulations, the “wrapping” of the diffusion wave can simply be interpreted as incoming inhibitor concentrations from neighbour volumes.

There exists a variety of optimised algorithms for solving the diffusion equation, such as the Jacobi or the Gauss-Seidel methods [113]. However, these are mostly limited to steady-state solutions, meaning that they cannot capture snapshots of the diffusion process prior to equilibration and generally omit the notion of time. Since the temporal aspect is of major importance in the current study, the numerical methods focus on the time-dependent solution of the diffusion equation.

The term $D \frac{\delta t}{\delta x^2}$ forms a dimensionless parameter, commonly referred to as the *Fourier number* [114]. The stability of the time-dependent numerical solver can greatly depend on this number [115], so it is necessary to maintain the ratio between the time step δt and the squared spatial step δx^2 below a certain threshold. This implies that δt scales quadratically with δx when the spatial resolution of the lattice is changed. This can be very restrictive, as a fine-grain lattice necessitates a very small time step and therefore a large number of simulation steps to capture a given time period.

For this reason, separate models are developed to represent three different scales of diffusion phenomena in spore cultures, such that each scale may address a different aspect from the research objective. At the coarsest resolution, the spores are viewed as inhibitor sources with negligible volumes compared to the mass of inhibitor moving in the extracellular space, so δx is set to be larger than the size of a spore. On an intermediate scale, δx is tuned to be precisely the size of a spore, effectively representing the spore as a node on the lattice. The third model adjusts δx to the scale of the cell wall, approximating the spherical geometry of the spore and thus capturing more spatial details.

3.3.2 Numerical model: macroscopic scale

The first model views each lattice site as a box region with a side δx , which may contain a spore, but the spore volume is not large enough to alter the course of diffusion (by being a low-diffusivity obstacle). Nonetheless, the spore adds new inhibitor concentration to the box with a rate based on the concentration difference between the spore and the medium in the box. In this sense, the spore does not occupy the same spatial system as the medium, but it is a source of new concentration, communicating with the medium via the lattice node assumed to contain the spore (Figure 3.1). The concentration drop between the spore and its containing cell evolves over time according to Equation 3.6:

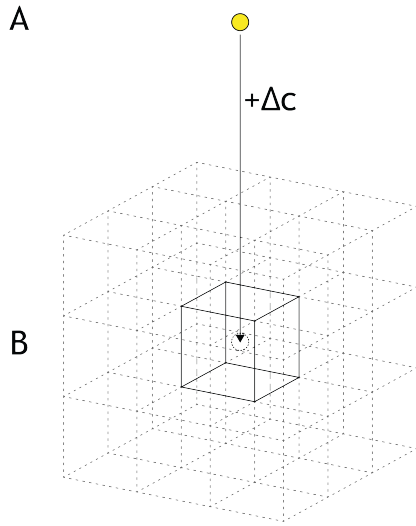


FIGURE 3.1: In the macroscopic-scale model (low resolution), the spore (system A) does not interfere with the flow of diffusion in the medium (system B) due to its relatively small volume. It does, however, serve as a source or a sink for the concentration in its containing lattice node (cube with black outline).

$$\frac{d(c_{\text{in}} - c_{\text{out}})}{dt} = \frac{dc_{\text{in}}}{dt} - \frac{dc_{\text{out}}}{dt} = -\frac{AP_s}{V}(c_{\text{in}} - c_{\text{out}}). \quad (3.31)$$

Here, c_{in} is the inhibitor concentration inside the spore and c_{out} is the concentration in the external medium. The derivative of the internal concentration is approximated by a finite difference scheme:

$$\frac{dc_{\text{out}}}{dt} \approx \frac{c_{\text{out}}(t + \delta t) - c_{\text{out}}(t)}{\delta t}. \quad (3.32)$$

Similarly,

$$\frac{dc_{\text{in}}}{dt} \approx \frac{c_{\text{in}}(t + \delta t) - c_{\text{in}}(t)}{\delta t}. \quad (3.33)$$

Using these discretisations, the update of the spore concentration can be expressed as

$$c_{\text{in}}(t + \delta t) = c_{\text{out}}(t + \delta t) + c_{\text{in}}(t) - c_{\text{out}}(t) - \frac{AP_s}{V}\delta t[c_{\text{in}}(t) - c_{\text{out}}(t)] \quad (3.34)$$

$$= c_{\text{out}}(t + \delta t) + (c_{\text{in}}(t) - c_{\text{out}}(t)) \left(1 - \frac{AP_s}{V}\delta t\right). \quad (3.35)$$

The problem arising here is the interdependence between the future concentration states $c_{\text{in}}(t + \delta t)$ and $c_{\text{out}}(t + \delta t)$. This can be resolved by implementing a half-step for the concentration drop update:

$$\Delta c^{(1/2)} = (c_{\text{in}}(t) - c_{\text{out}}(t)) \left(1 - \frac{AP_s}{2V}\delta t\right). \quad (3.36)$$

The outside concentration in the spore-containing volume is then updated as a mixture between free neighbour-to-neighbour diffusion and the added concentration from the source:

$$c_{\text{out}}(t + \delta t) = c_{\text{out}}(t) + \delta t \left[D\nabla^2 c_{\text{out}}(t) + \frac{AP_s}{V}\Delta c^{(1/2)}\right]. \quad (3.37)$$

Finally, the spore's internal concentration at a full time step can be completed:

$$c_{\text{in}}(t + \delta t) = c_{\text{out}}(t + \delta t) + \Delta c^{(1/2)} \left(1 - \frac{AP_s}{2V}\delta t\right). \quad (3.38)$$

The remaining lattice nodes, not containing a spore, are updated using Equation 3.30.

3.3.3 Numerical model: spore scale

On the intermediate scale, a spore is represented by a node on a lattice with $\delta x = 5 \mu\text{m}$, a typical diameter for an *A. niger* conidium. The orthogonal arrangement and von Neumann neighbourhood rule imply that the spore is more topologically akin to a cube than to a sphere, as illustrated in Figure 3.2. Conveniently, the permeation-defining area-to-volume ratio of a $R \times R \times R$ cube is the same as that of an inscribed sphere with a diameter R , namely $A/V = 3/R$.

Thus, the spore now occupies a definite region, albeit a singular one, in which the diffusion coefficient changes its value. This means that, while the lattice concentrations are normally updated by equation 3.30 for the domain of the extracellular medium, the spore node and the lattice nodes adjacent to it must account for the flux at the spore-medium

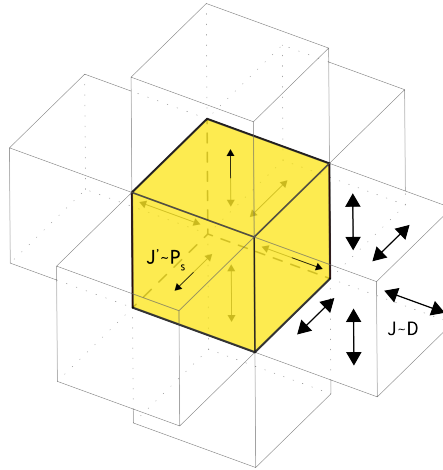


FIGURE 3.2: The spore-scale (medium-resolution) model: the flux J' at the spore-medium interface is governed by slow permeation, while the flux J in the medium is governed by fast diffusion.

interface. This can be better understood by observing Figure 3.2. A spore releases inhibitor molecules into its neighbour sites through each of its six interfacial planes. The driving flux is proportional to the permeation constant of the cell wall, P_s . To the right of the spore, a neighbour site receives the flux from the spore through one of its sides and exchanges concentration with other medium nodes through the rest of the boundary planes. The same applies to all other neighbour sites of the spore. Noting that D scales the concentration transport from one lattice node to another, the centre-to-centre distances of which is δx , the transport between a spore node and a medium node is scaled by a modified diffusion constant D' , spanning an interface of depth δx . In other words, Equation 3.9 can be used to express $D' = P_s \delta x$. This leads to a modified update scheme for the spore site:

$$c_{i,j,k}^{n+1} = c_{i,j,k}^n + D' \frac{\delta t}{\delta x^2} \left(\sum_{i',j',k'} c_{i',j',k'}^n - 6c_{i,j,k}^n \right), \quad (3.39)$$

$$c_{i,j,k}^{n+1} = c_{i,j,k}^n + P_s \frac{\delta t}{\delta x} \left(\sum_{i',j',k'} c_{i',j',k'}^n - 6c_{i,j,k}^n \right). \quad (3.40)$$

For a spore-adjacent site, only the concentration difference across the interface is weighted by D' , the rest remains D -dependent. For example

$$c_{i,j,k}^{n+1} = c_{i,j,k}^n + \frac{\delta t}{\delta x^2} \left[P_s \delta x (c_{i+1,j,k}^n - c_{i,j,k}^n) + D \left(c_{i-1,j,k}^n + \sum_{j'} \sum_{k'} c_{i',j',k'}^n - 5c_{i,j,k}^n \right) \right] \quad (3.41)$$

indicates an interfacial permeation between the concentration sites $c_{i,j,k}$ and $c_{i+1,j,k}$, while the other sites exchange concentrations with $c_{i,j,k}$ via the standard constant D .

3.3.4 Numerical model: cell wall scale

While the medium-resolution model acknowledges the spore as a region of modified diffusivity, its resolution is still coarse. To represent the conidium in higher detail, including its spherical geometry and the thickness of its cell wall, the spatial resolution needs to be increased. The spatial step is set to $\delta x = 0.2 \mu\text{m}$, approximately corresponding to half of the upper bound of the cell wall thickness. This way, the cell wall comprises a double layer of lattice nodes. The spore is thus a sphere approximated by cubic voxels. Examples from literature show that such a discretisation leads to an overestimation of the outer surface area of the sphere by a factor of 1.5 [116], which inevitably has an effect on the flux of inhibitor between the spore and the medium, e.g. reflected by the prefactor in Equation 3.5. To compensate for this, the permeation constant used in this model is multiplied by 2/3.

In the coarser models, it was assumed that the concentration of inhibitor is homogeneously distributed in the spore volume, including its inner cell wall. For the sake of comparability, the high-resolution model can be set up with equal concentration values within the entire spore volume (Figure 3.3, left), or it can correspond to a more realistic scenario, with the inhibitor only restricted to the region of the cell wall, which is the outer shell of the sphere (Figure 3.3, right). The first case assumes a very coarse bulk averaging of the diffusivities in the spore compartments. In the latter case, it is assumed that the inhibitor is already expressed in the cell wall at inoculation and that it cannot re-enter the protoplast, i.e. the inner region of the sphere is made inaccessible for diffusion. While still being a major simplification, the second scenario reduces the number of relevant diffusion regions and narrows down the materials for which the permeabilities need to be accounted for.

The interfacial neighbourhoods between lattice sites follow the update rule of Equation 3.41. This can be seen as, for example, the exchange of molecules across the hydrophobic-melanin layer. The question remains, what diffusivity governs the transport of molecules inside the cell wall, e.g. within the polysaccharide network. While the specific diffusion

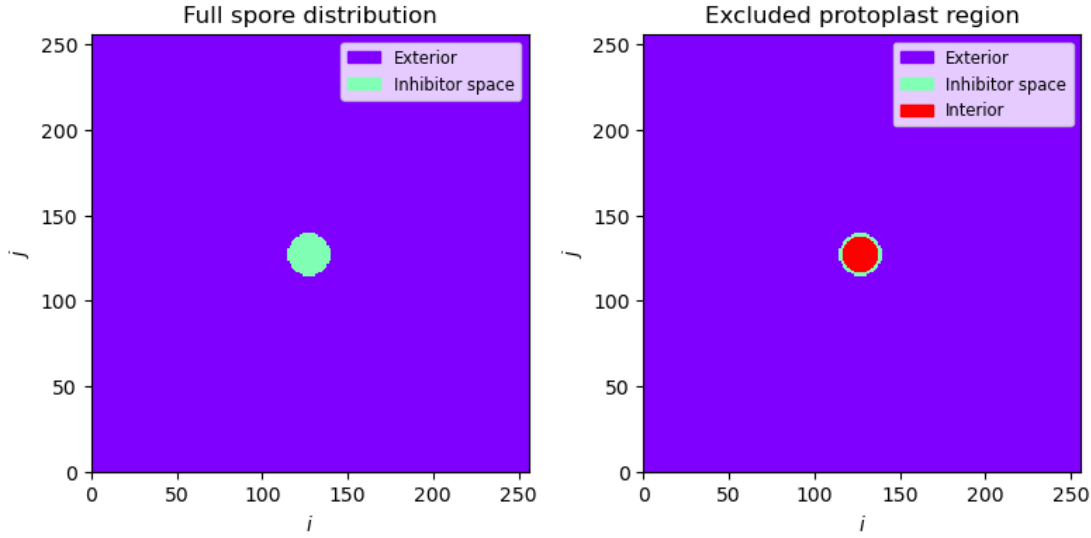


FIGURE 3.3: Two options for the inhibitor distribution in the high-resolution model: homogeneous in the entire spore (left) or restricted to the cell wall (right). The images are cross-sections through the centre of the three-dimensional lattice.

constants from literature could be used here, a simple technique, often used in practice, could be applied. Instead of viewing the inner and outer cell wall layers as separate diffusion regions, one can “clump” their diffusivities into a general cell wall region. When having two lattice regions (A and B) of different diffusivity (D_A and D_B) sharing an interface, some diffusion models treat the interfacial diffusion constant D_{AB} as the harmonic mean of the two regional diffusivities [117]:

$$D_{AB} = \frac{2D_A D_B}{D_A + D_B}. \quad (3.42)$$

Knowing that D_{AB} is the constant which determines the depletion of the spore’s inhibitor, and that D_A is the diffusion constant of the inhibitor in the medium, the “clumped” internal diffusion constant D_B can be expressed from Equation 3.42 as

$$D_B = \frac{D_{AB} D_A}{2D_A - D_{AB}}. \quad (3.43)$$

Thus, D_B scales the neighbour differences between the internal lattice sites in an update scheme analogous to Equation 3.41.

At this scale, the Fourier number constraint imposes such a small time step δt that large simulations become unwieldy. To alleviate the numerical stability constraint, one can replace the forward Euler method by an *implicit, backward Euler scheme*, which is known to be unconditionally stable [111]. This boils down to expressing the current

concentration state, $c_{i,j,k}^n$, as a function of the future concentration state, $c_{i,j,k}^{n+1}$, as opposed to the approach in Equation 3.30:

$$c_{i,j,k}^n = c_{i,j,k}^{n+1} - D \frac{\delta t}{\delta x^2} \left(\sum_{i',j',k'} c_{i',j',k'}^{n+1} - 6c_{i,j,k}^{n+1} \right). \quad (3.44)$$

This leads to a system of linear equations with the matrix form $\mathbf{A}\mathbf{c}^{n+1} = \mathbf{c}^n$, where \mathbf{A} is a matrix of coefficients derived from Equation 3.44, \mathbf{c}^{n+1} is a vector of unknowns for the future concentration values and \mathbf{c}^n is the vector of current concentration values. This system can be solved by numerical methods without risk of instability, but an overly large time step may scale the up error magnitude in the resulting solutions, since the method is first-order accurate [111].

3.3.5 Analytical models

While the lattice-based models are useful for capturing concentration distributions over the entire spatial domain, this study is primarily interested in the residual concentration in the spore. This means that, under certain simplifications, the simulations can be replaced by a simple formula that can be readily evaluated. One such formula can be derived from the exponential relaxation of the concentration drop $\Delta c = c_{\text{in}} - c_{\text{out}}$ across the spore-medium interface (Equation 3.6). Assuming that the spore is located in an infinitely vast, inhibitor-free medium and that each released molecule of inhibitor immediately diffuses away, the external concentration c_{out} can be fixed to zero [60]. This means that

$$c_{\text{in}}(t) = c_0 e^{-t/\tau}, \quad (3.45)$$

where $c_0 = c_{\text{in}}(0)$ is the initial concentration inside the spore.

The assumption for this *simple permeation model*, however, breaks down once we consider dense spore cultures, in which each spore releases a halo of inhibitor that soon reaches other spores. In this case, the inhibitor released from the ensemble accumulates in the environment and becomes a non-negligible time-dependent variable. Furthermore, the volume excluded by those spores becomes an important factor.

One fundamental assumption of the simple permeation model that can be maintained is the considerably faster diffusion in the medium compared to the permeation rate at the spore interface. Because of this, one can assume that the inhibitor molecules quickly

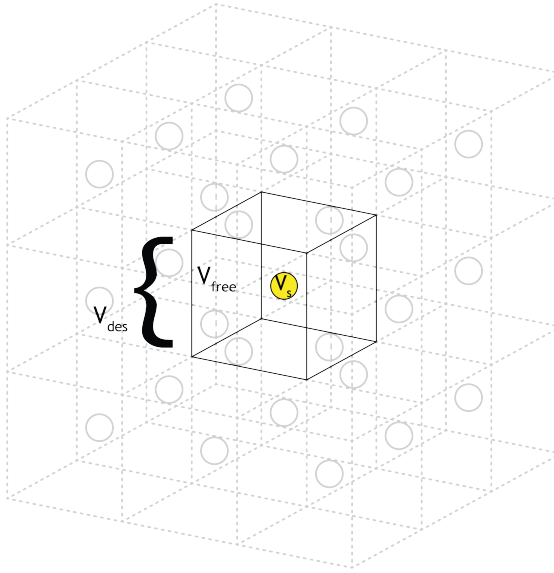


FIGURE 3.4: Schematic representation of the designated volume for each spore.

distribute in the medium and it is not necessary to explicitly solve the diffusion equation in the external domain.

Imposing the simplification that spores at an inoculum density of ρ_s are positioned in a regular grid, a designated volume per spore can be defined as

$$V_{\text{des}} = \frac{1}{\rho_s}. \quad (3.46)$$

Even if molecules diffuse over its boundaries into adjacent volumes, this occurs in a symmetric fashion, so that the net quantity of molecules within a volume remains preserved. Consequently, one can separate this volume into the space occupied by the spore, V_s , and that remaining for the medium, $V_{\text{free}} = V_{\text{des}} - V_s$ (Figure 3.4). A volume fraction, denoting the percentage per unit volume occupied by the conidia, can be defined as $\phi = \rho_s V_s$.

The flux out of a sphere is still driven by the concentration jump, multiplied by the permeability across the entire spore surface:

$$J(t) = P_s A [c_{\text{in}}(t) - c_{\text{out}}(t)]. \quad (3.47)$$

Let N denote the number of particles. The rate of particles exiting the spore is expressed as

$$\frac{dN_{\text{in}}}{dt} = \frac{d(V_s c_{\text{in}})}{dt} = -J(t) = -P_s A [c_{\text{in}}(t) - c_{\text{out}}(t)]. \quad (3.48)$$

Thus, the change in concentration in the spore can be written as

$$\frac{dc_{\text{in}}}{dt} = - \left(\frac{P_s A}{V_s} \right) [c_{\text{in}}(t) - c_{\text{out}}(t)] = -\tau^{-1} [c_{\text{in}}(t) - c_{\text{out}}(t)]. \quad (3.49)$$

The rate of particles entering the medium is equal to the flux with an opposite sign:

$$\frac{dN_{\text{out}}}{dt} = \frac{d(V_{\text{free}} c_{\text{out}})}{dt} = J(t) = P_s A [c_{\text{in}}(t) - c_{\text{out}}(t)]. \quad (3.50)$$

Consequently,

$$\frac{dc_{\text{out}}}{dt} = \left(\frac{P_s A}{V_{\text{free}}} \right) [c_{\text{in}}(t) - c_{\text{out}}(t)] = \tau^{-1} \frac{V_s}{V_{\text{free}}} [c_{\text{in}}(t) - c_{\text{out}}(t)]. \quad (3.51)$$

It is easy to see that, in the limit $t \rightarrow \infty$, the concentrations will equilibrate to the same value, which would stop the release from the spore. The steady-state concentration can be obtained by observing the mass-conservation principle. At equilibrium, $c_{\text{eq}} = c_{\text{in}}(\infty) = c_{\text{out}}(\infty)$ and the N molecules are evenly distributed in the reference volume:

$$N = (V_s + V_{\text{free}}) c_{\text{eq}} = \frac{1}{\rho_s} c_{\text{eq}}. \quad (3.52)$$

In the initial condition,

$$N = V_s c_{\text{in}}(0) + V_{\text{free}} c_{\text{out}}(0). \quad (3.53)$$

The initial concentration in the spore, $c_{\text{in}}(0) = c_0$, and the initial external concentration $c_{\text{out}}(0) = c_{\text{ex}}$, are constants. Equating the mass expressions yields

$$\frac{1}{\rho_s} c_{\text{eq}} = V_s c_0 + V_{\text{free}} c_{\text{ex}} = V_s c_0 + \left(\frac{1}{\rho} - V_s \right) c_{\text{ex}}. \quad (3.54)$$

Therefore,

$$c_{\text{eq}} = \rho_s \left[V_s c_0 + \left(\frac{1}{\rho} - V_s \right) c_{\text{ex}} \right] = \phi c_0 + (1 - \phi) c_{\text{ex}}. \quad (3.55)$$

Coming back to the system of coupled ODEs,

$$\dot{c}_{\text{in}} = \tau^{-1} (c_{\text{in}} - c_{\text{out}}) \quad (3.56)$$

$$\dot{c}_{\text{out}} = \tau^{-1} \frac{V_s}{V_{\text{free}}} (c_{\text{in}} - c_{\text{out}}), \quad (3.57)$$

the eigenvalues of the matrix of coefficients,

$$\mathbf{A} = \tau^{-1} \begin{bmatrix} -1 & 1 \\ \frac{V_s}{V_{\text{free}}} & -\frac{V_s}{V_{\text{free}}} \end{bmatrix} \quad (3.58)$$

are found to be $\lambda_0 = 0$ and $\lambda_1 = -\tau^{-1} \left(1 + \frac{V_s}{V_{\text{free}}} \right)$. The latter governs the decay toward equilibrium and can be rewritten as

$$\lambda_1 = -\tau^{-1} \left(1 + \frac{V_s}{V_{\text{free}}} \right) = -\tau^{-1} \left(\frac{V_{\text{free}} + V_s}{V_{\text{free}}} \right) = -\tau^{-1} \left(\frac{V_{\text{des}}}{V_{\text{des}} - V_s} \right) = -\tau^{-1} \left(\frac{1}{1 - \phi} \right). \quad (3.59)$$

Since the standard solution of both ODEs is an exponential decay, its effective characteristic time is computed as the reciprocal of λ_1 :

$$\tau_{\text{eff}} = -\frac{1}{\lambda_1} = \tau(1 - \phi). \quad (3.60)$$

One can define the deviation of the internal concentration from equilibrium as $\delta(t) = c_{\text{in}}(t) - c_{\text{eq}}$ and it can be shown that this deviation also relaxes to zero with the characteristic time τ_{eff} :

$$\delta(t) = \delta(0)e^{-t/\tau_{\text{eff}}}. \quad (3.61)$$

Since $\delta(0) = c_0 - c_{\text{eq}}$,

$$c_{\text{in}}(t) = c_{\text{eq}} + (c_0 - c_{\text{eq}})e^{-t/\tau_{\text{eff}}}, \quad (3.62)$$

Plugging in the term for c_{eq} ,

$$c_{\text{in}}(t) = \phi c_0 + (1 - \phi) \left[c_{\text{ex}} + (c_0 - c_{\text{ex}}) e^{-\frac{t}{\tau(1-\phi)}} \right]. \quad (3.63)$$

In case there is no external inhibitor concentration prior to the inoculation, $c_{\text{ex}} = 0$ and the above formula simplifies to

$$c_{\text{in}}(t) = \phi c_0 + (1 - \phi)c_0 e^{-\frac{t}{\tau(1-\phi)}}. \quad (3.64)$$

For very low spore densities, $\phi \rightarrow 0$ and the expression reverts to Equation 3.45. As the volume ratio increases, saturation effects become more prominent due to the increasing ϕc_0 term and the modified relaxation time in the exponent. Due to its dependence on the designated volume per conidium, this model is henceforth referred to the *volume-based model*.

3.3.6 Model comparison setup

To validate the models as being representative of the same release process, a numerical experiment is set up to compare the residual inhibitor concentration in a single spore over time for each of the models. A time frame of 4 hours is chosen, characteristic for the onset of germination. As illustrative parameters, the initial inhibitor concentration c_0 is set to unity, the diffusivity in the medium is set to that of glucose in water ($D = 700 \mu\text{m}^2 \text{s}^{-1}$) and the permeation constant is tuned such that the concentration at 4 hours is depleted to 1% of its original value according to Equation 3.45 ($P_s = 2.665 \times 10^{-4} \mu\text{m s}^{-1}$). The spatial increment in the low-resolution model is set to $20 \mu\text{m}$, with a lattice of size $M = 16$ spanning a spatial domain with a length $L = 320 \mu\text{m}$; the time increment is set to $\delta t = 0.1 \text{ s}$. The spatial domain for the medium-resolution model has the same size, with $M = 64$, $\delta x = 5 \mu\text{m}$ and $\delta t = 0.005 \text{ s}$. Due to memory limitations, the spatial domain in the implicitly solved high-resolution model is set to $51.2 \mu\text{m}$, with $M = 256$, $\delta x = 0.2 \mu\text{m}$ and $\delta t = 0.05 \text{ s}$. Both variants of the high-resolution model are tested: with a spore full of inhibitor and with an inhibitor only constrained to the cell wall volume. In both cases, the initial concentration per lattice node is set to one.

As a second validation, the models are compared in their capacity to represent inhibitor saturation under increasing spore density. To this end, a range of densities between two centre-to-centre inter-spore distances are explored: $L = 25 \mu\text{m}$ and $L = 50 \mu\text{m}$; equivalent to periodic system sizes in the numerical models. Since the low-resolution model is too coarse to capture the small lattice size, only the two remaining numerical models and the volume-based analytical model are compared. The simulations are run for a time span of $t_{\text{max}} = 12 \text{ h}$ to account for the delayed relaxation of the concentration.

3.4 Model parameters

To apply the models to realistic scenarios, their parameters need to correspond to known properties of the investigated systems. As best documented examples, glucose and 1-octen-3-ol are selected as candidates for the induction and inhibition signals, respectively. Hydrophobins, agarose-like and cellulose-like polysaccharides are outlined as main components of the cell wall, while the cell membrane is considered equivalent to a lipid bilayer. This section derives plausible parameter values for these compounds by using simple calculations on quantities outlined in the [Literature Review](#).

3.4.1 Diffusion and permeation constants

Several diffusivity values of glucose in different systems were previously extracted from literature. The diffusion and permeation constants can be related to barriers of specific thickness, corresponding to layers of the cell wall. The cell membrane and the hydrophobin layer have a known thickness (3.8 nm and 10 nm, respectively). The intermediate layers, rich in polysaccharides, may exhibit a more significant variation. As a rough estimate based on documented observations, it is assumed that the total cell wall thickness has an upper limit of 400 nm and a lower limit of 200 nm. While chitin, melanin and other interlinked components of the cell wall may affect its permeability, the data on their diffusivity is sparse, so it is assumed for simplicity that the polysaccharides are the main diffusion-limiting molecules. Thus, subtracting the hydrophobin layer from the net cell wall thickness, two extremes of the polysaccharide layer are considered: 190 nm and 390 nm.

The resulting diffusion and permeation constants are compiled in Table 3.1. A control value for a hypothetical cell wall composed of water is included. It is assumed that the P_s computed for the polysaccharide layer variants includes a porosity factor as per the pore-flow model (Equation 3.7). For the derivation of D from P_s for a lipid bilayer membrane, the solution-diffusion model is used (Equation 3.8) with the octanol-water partition coefficient for glucose $K_p = 6.31 \times 10^{-4}$ ($\log K_p = -3.2$) [118]. It is then assumed, for lack of further data and due to the similarity of lipid and hydrophobin bilayers, that the diffusion constant in hydrophobins is equal to that in lipids. Furthermore, the extreme case of a non-porous hydrophobin layer is assumed, implementing the same solution-diffusion model to scale the permeation constant to a layer of 10 nm.

It can be shown that the diffusivity values of glucose can be used to infer some of the constants for 1-octen-3-ol. First, the Stokes-Einstein relation,

glucose	D	P_s
water	$7 \times 10^{-6} \text{ cm}^2 \text{ s}^{-1}$ [77]	$1.175 \times 10^{-1} \text{ cm s}^{-1}$ ($d = 400 \text{ nm}$)
agarose-like layer	$6.46 \times 10^{-6} \text{ cm}^2 \text{ s}^{-1}$ [77]	$3.400 \times 10^{-1} \text{ cm s}^{-1}$ ($d = 190 \text{ nm}$)
		$1.656 \times 10^{-1} \text{ cm s}^{-1}$ ($d = 390 \text{ nm}$)
cellulose-like layer	$1.7 \times 10^{-7} \text{ cm}^2 \text{ s}^{-1}$ [78]	$8.947 \times 10^{-3} \text{ cm s}^{-1}$ ($d = 190 \text{ nm}$)
		$4.359 \times 10^{-3} \text{ cm s}^{-1}$ ($d = 390 \text{ nm}$)
lipid bilayer	$1.126 \times 10^{-13} \text{ cm}^2 \text{ s}^{-1}$	$1.900 \times 10^{-10} \text{ cm s}^{-1}$ ($d = 3.8 \text{ nm}$) [81, 82]
hydrophobin layer	$1.126 \times 10^{-13} \text{ cm}^2 \text{ s}^{-1}$	$7.22 \times 10^{-11} \text{ cm s}^{-1}$ ($d = 10 \text{ nm}$)

TABLE 3.1: Diffusion coefficient (D) and permeation coefficient (P_s) of glucose in various media. The D coefficient for hydrophobins is assumed equal to that for lipids.

$$D = \frac{k_B T}{6\pi\eta a}, \quad (3.65)$$

can be used to compute the D of 1-octen-3-ol in water. For this, a temperature of $T = 303.15 \text{ K}$ can be considered (a common cultivation temperature for *Aspergillus* conidia) and thus a thermodynamic constant of $k_B T = 4.18 \times 10^{-21} \text{ J}$. The viscosity of water at this temperature is $\eta = 0.797 \text{ mPa s}$. The Stokes radius of 1-octen-3-ol can be computed through the spherical approximation of its molecular volume V_M using its molecular mass $m_M = 128.21 \text{ g mol}^{-1}$ and its average density $\rho = 0.837 \text{ g mL}^{-1}$:

$$a = \left(\frac{3}{4\pi} V_M \right)^{1/3} = \left(\frac{3}{4\pi} \frac{m_M}{\rho N_A} \right)^{1/3} \approx 0.393 \text{ nm}. \quad (3.66)$$

In the above calculation, N_A is the Avogadro number. Plugging in all values into the Stokes-Einstein relation, one attains $D \approx 6.9016 \times 10^{-6} \text{ cm}^2 \text{ s}^{-1}$. This is only slightly lower than the indicated D of glucose in water.

Computing the remaining diffusion constants requires knowledge of the viscosity of agarose, cellulose, lipids and hydrophobins. Since such information is difficult to obtain, an alternative approach can be utilised by taking the ratio of each diffusion constant of 1-octen-3-ol and its respective diffusion constant of glucose, defined by their Stokes-Einstein relations:

$$\frac{D(1\text{-octen-3-ol})}{D(\text{glucose})} = \frac{k_B T}{k_B T} \frac{6\pi \eta a(\text{glucose})}{6\pi \eta a(1\text{-octen-3-ol})} = \frac{a(\text{glucose})}{a(1\text{-octen-3-ol})} \approx 0.916. \quad (3.67)$$

Multiplying each diffusion coefficient of glucose by this ratio yields the approximate diffusion coefficient of 1-octen-3-ol in the same medium. This results in the values listed in Table 3.2. Special attention is paid to the conversion of D to P_s in the case of the lipid membrane, since 1-octen-3-ol is much less polar than glucose: its partition coefficient is

1-octen-3-ol	D	P_s
water	$6.902 \times 10^{-6} \text{ cm}^2 \text{ s}^{-1}$	$1.173 \times 10^{-1} \text{ cm s}^{-1} (d = 400 \text{ nm})$
agarose-like layer	$5.918 \times 10^{-6} \text{ cm}^2 \text{ s}^{-1}$	$3.311 \times 10^{-1} \text{ cm s}^{-1} (d = 190 \text{ nm})$
cellulose-like layer	$1.557 \times 10^{-7} \text{ cm}^2 \text{ s}^{-1}$	$1.517 \times 10^{-1} \text{ cm s}^{-1} (d = 390 \text{ nm})$
lipid bilayer	$1.032 \times 10^{-13} \text{ cm}^2 \text{ s}^{-1}$	$8.196 \times 10^{-3} \text{ cm s}^{-1} (d = 190 \text{ nm})$
hydrophobin layer	$1.032 \times 10^{-13} \text{ cm}^2 \text{ s}^{-1}$	$3.993 \times 10^{-3} \text{ cm s}^{-1} (d = 390 \text{ nm})$
		$8.586 \times 10^{-5} \text{ cm s}^{-1} (d = 3.8 \text{ nm})$
		$3.263 \times 10^{-5} \text{ cm s}^{-1} (d = 10 \text{ nm})$

TABLE 3.2: Diffusion coefficient (D) and permeation coefficient (P_s) of 1-octen-3-ol in various media. The D coefficient for hydrophobins is assumed equal to that for lipids.

$K_p = 316.23$ ($\log K_p = 2.5$). This results in a much higher effective P_s through the lipid membrane and the rodlet layer compared to glucose.

To obtain a general permeation constant for the cell wall complex, an analytical approximation can be made by viewing all M cell wall components as layered shell-like barriers [119] and combining their individual permeation constants P_i with the formula

$$\frac{1}{P_{\text{total}}} = \sum_i^M \frac{1}{P_i}. \quad (3.68)$$

For a glucose molecule entering the inner cell wall, the main limiting layer is the hydrophobin-melanin shell. For the escape of inhibitor molecules into the medium, however, several barrier composition scenarios are possible, depending on where the inhibitor originates from and where its target locus is:

- If the inhibitor is superficially expressed upon inoculation and its target locus is in the outermost layer of the cell wall, it is virtually unobstructed by any layers, only limited by diffusion in water.
- If the inhibitor source and target locus are embedded between the inner and outer cell wall layers, diffusion is obstructed only by the hydrophobin-melanin layer.

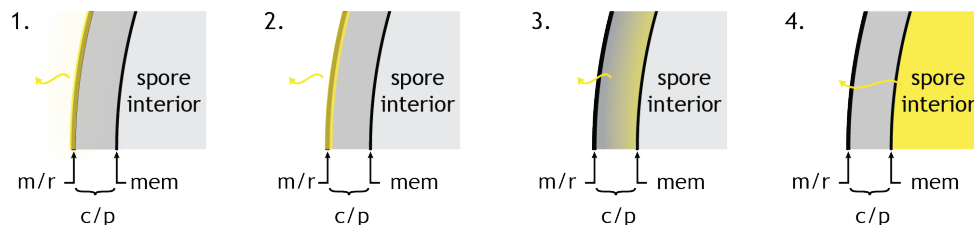


FIGURE 3.5: Diagrammatic views of the different scenarios for the initial inhibitor concentration (inhibitor marked in yellow). Abbreviations: m/r - melanin/rodlets, c/p - chitin/polysaccharides, mem - cell membrane.

Barrier composition	Total thickness	P_{total}
superficial	0 nm	∞
rodlet layer	10 nm	$3.263 \times 10^{-5} \text{ cm}^2 \text{ s}^{-1}$
rodlets + agarose-like polysaccharides	200 nm	$3.263 \times 10^{-5} \text{ cm}^2 \text{ s}^{-1}$
rodlets + agarose-like polysaccharides	400 nm	$3.262 \times 10^{-5} \text{ cm}^2 \text{ s}^{-1}$
rodlets + cellulose-like polysaccharides	200 nm	$3.250 \times 10^{-5} \text{ cm}^2 \text{ s}^{-1}$
rodlets + cellulose-like polysaccharides	400 nm	$3.237 \times 10^{-5} \text{ cm}^2 \text{ s}^{-1}$
rodlets + agarose + lipid membrane	203.8 nm	$2.364 \times 10^{-5} \text{ cm}^2 \text{ s}^{-1}$
rodlets + agarose + lipid membrane	403.8 nm	$2.364 \times 10^{-5} \text{ cm}^2 \text{ s}^{-1}$
rodlets + cellulose + lipid membrane	203.8 nm	$2.358 \times 10^{-5} \text{ cm}^2 \text{ s}^{-1}$
rodlets + cellulose + lipid membrane	403.8 nm	$2.350 \times 10^{-5} \text{ cm}^2 \text{ s}^{-1}$

TABLE 3.3: Composite layer permeation coefficients (P_{total}) for 1-octen-3-ol in various scenarios of barrier composition.

- If the inhibitor source and target loci are embedded deep inside the inner cell wall layer, diffusion is obstructed by the polysaccharide network and the hydrophobin-melanin layer;
- If the inhibitor source and target loci are inside the protoplast, diffusion is obstructed by the cell membrane and the entirety of the cell wall.

The composite permeation constants for all scenarios are computed using Equation 3.68 and listed in Table 3.3. The permeabilities vary by a small amount, mostly dominated by the effect of the outer hydrophobin-melanin layer.

3.4.2 Initial and threshold concentrations

The inhibitor depletion model aims to trace the exponential decrease of an initial inhibitor concentration to a threshold value c_T beyond which the spore germination is no longer inhibited. In search of the initial concentration c_0 for the case of 1-octen-3-ol, the study by Miyamoto et al. [5] on *A. flavus* conidia provides instructive clues. After a repeated freeze-dry cycle to destroy the integrity of the cell wall, not more than 1 μM of 1-octen-3-ol was released in by the culture of 10^9 spores/mL in a 300 μL suspension, equivalent to 3×10^8 spores. The quantity of 1-octen-3-ol in this suspension is calculated to 3×10^{-10} mol, or 1×10^{-18} mol per conidium. It is assumed that these molecules are released equally from the spore volumes. Taking rough spore radius estimate of 2.5 μm , a single spore volume is $\frac{4}{3}\pi R^3 = 65.45 \mu\text{m}^3$. This leads to a 1-octen-3-ol concentration of $1.53 \times 10^{-5} \text{ M}$ per conidium.

Findings in literature report different concentrations at which 1-octen-3-ol causes inhibition, e.g. 1 mM for *A. nidulans* [2] or 10 mM for *A. flavus* [5]. However, in both of these

studies, 1-octen-3-ol is exogenously added to the culture, so there is no indication of the natural, in-vivo threshold. It is safe to assume that the inhibitor would lose its effect, at the latest, when there are less than a hundred molecules left in the conidium. This amounts to a concentration of about 2.54×10^{-9} M, nearly five orders smaller than the presumed initial concentration.

3.4.3 Adsorption parameters

A study on the adsorption kinetics of 1-octen-3-ol in yeast β -glucan indicates an adsorption capacity $q_m = 1.863 \mu\text{g mg}^{-1}$ and an equilibrium constant $K_{\text{eq}} = 1.051 \text{ mL } \mu\text{g}^{-1} \approx 1.345 \times 10^5 \text{ M}^{-1}$ (considering the molecular weight m_M of 1-octen-3-ol) at a temperature of 37°C [89]. The measure q_m expresses the mass of 1-octen-3-ol adsorbed per mass of glucan and needs to be converted to a concentration capacity, B_{max} . This can be done through the formula

$$B_{\text{max}} = \frac{q_m \rho_{\text{glucan}}}{m_M}, \quad (3.69)$$

where ρ_{glucan} is the density of glucan in the experiment. The paper mentions that 0.01 g of yeast glucan was added to a 100 mL solution, resulting in $\rho_{\text{glucan}} = 0.1 \text{ mg mL}^{-1}$ and $B_{\text{max}} = 1.45 \times 10^{-6}$ M.

The assumption of a linear regime in the approximation in Equation 3.14 was under the condition that $K_{\text{eq}} c_{\text{free}} \ll 1$. Since the concentration of 1-octen-3-ol in the conidium is at its peak at the initial $c_0 = 1.53 \times 10^{-5}$ M, it can be assumed that the condition holds for the longer part of the release process. Thus, Equation 3.21 can be rewritten to obtain the ratio between the permeation constant without and with adsorption:

$$\frac{P_s}{P_{\text{ad}}} = K_{\text{eq}} B_{\text{max}} + 1 \approx 1.195. \quad (3.70)$$

This suggests that the standard permeation constant can be reduced by almost a half by the adsorption kinetics.

3.5 Inducer permeation

Using some of the presented theory, a simple check can be performed to confirm that the permeation of inducer molecules slows down their entry into the cell wall. The inducer

concentration at the receptor proteins is calculated using Equation 3.45, but this time it is assumed that c_{out} is a constant large number, which leads to the formula

$$c_{\text{in}}(t) = \left(1 - e^{-t/\tau}\right) c_{\text{out}}. \quad (3.71)$$

The characteristic time in this case is formed by

$$\tau = \frac{V_{\text{ps}}}{P_s^{\text{cs}} A}, \quad (3.72)$$

where A is still the outer surface area of the spore, V_{ps} is the available volume of the inner cell wall (polysaccharide layer) and P_s^{cs} is the permeation constant of the carbon source through the hydrophobin layer. The total volume of the inner cell wall region computed as a spherical shell between the inner surface of the hydrophobin layer and the outer surface of the cell membrane: $V_{\text{psT}} = \frac{4}{3}\pi((R - d_{\text{hp}})^3 - (R - d_{\text{hp}} - d_{\text{ps}})^3)$, where R is the spore radius, d_{hp} and d_{ps} are the thicknesses of the hydrophobin layer and of the polysaccharide layer, respectively.

The volume that the inducer molecules can fill upon equilibration depends on the porosity of the cell wall layer. For instance, the cell wall of *Lycoperdon pyriforme* spores has been found to contain 24% water [120]. This means that the effective volume of the inner cell wall pores would be about one quarter of the shell volume. Taking the mean spore radius for *A. niger* (2.65 μm) and an estimated mean inner wall thickness of $d_{\text{ps}} = 290 \text{ nm}$, the accessible cell wall volume is estimated at $5.45 \mu\text{m}^3$. The permeation constant for glucose through hydrophobin is taken from Table 3.1. For a typical $c_{\text{out}} = 10 \text{ mM}$ [4], Equation 3.71 computes $c_{\text{in}}(4 \text{ h}) = 3.7 \text{ mM}$, a substantial percent of the outside concentration, yet still not equilibrated. This serves as a strong indication that slow permeation also governs the inducing signal.

3.6 Inhibitor release computations

To test the viability of the scenario in which a spore releases 1-octen-3-ol by passive diffusion to enable its germination, a set of numerical experiments is performed with the parameters described previously.

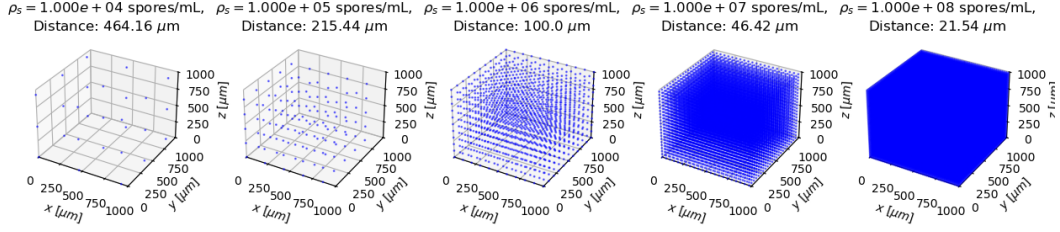


FIGURE 3.6: Visualisation of intermediate spore densities and the corresponding centre-to-centre distances between the spores.

3.6.1 Single-spore experiment setup

First, the simple permeation model is used to simulate the time course of inhibitor release for a single spore in an infinite medium for $t_{\max} = 4$ h. The permeation through the separate components in Table 3.2 as well as through all potential barrier compositions from Table 3.3 is computed for 1 million intermediate time steps. A second experiment addresses the question: What should P_s be for the inhibitor to decrease, by a certain percent, to its threshold concentration c_T in a given time span? Five orders of magnitude are explored - from a depletion to 10% ($c_T = \mathcal{O}(10^{-6} \text{ M})$) to a depletion to 10^{-5} times its original concentration ($c_T = \mathcal{O}(10^{-10} \text{ M})$). Two scenarios are observed with regard to the timing of germination - in the first scenario, the arrival at the threshold is set to 4 h and, in the second scenario, the germination-inducing depletion occurs at 2 h of cultivation. In the latter case, a two-hour lag between inhibitor depletion and germination is considered.

3.6.2 Multi-spore experiment setup

To explore the effect of density-driven inhibitor saturation, the volume-based analytical model and the medium-resolution numerical model are used to simulate different densities of regularly spaced spores, releasing inhibitor into the medium. The conidial densities range from 10^4 to 10^8 spores/mL, consistent with the density ranges used in laboratory experiments [1, 2]. The permeation constants used for this experiment correspond to the 4-hour depletion scenarios for the single-spore case.

3.6.3 Spore cluster experiment setup

The high-resolution numerical model is put to use in the exploration of spore clusters and their obstructive effect on diffusion. A lattice with $N = 128$ subdivisions per dimension and a space increment $\delta x = 0.2 \mu\text{m}$ (system size $L = 25.6 \mu\text{m}$) is set up with an absorbing boundary (all boundary concentrations are forced to zero). Two extreme scenarios are examined: a single spore positioned in the centre of the lattice and a spore fully

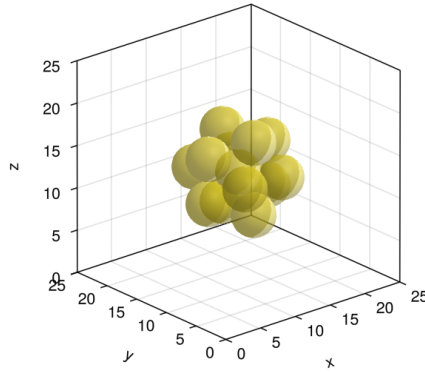


FIGURE 3.7: A densely packed 13-spore cluster.

surrounded by 12 identical directly adjacent neighbours in an icosahedral arrangement (the most compact cluster packing possible, as shown in Figure 3.7). The two inhibitor distribution scenarios outlined previously — homogenous over the spore and restricted to the cell wall — are explored for each cluster option. In the second case, c_0 is rescaled from the volume of the entire spore (V_s) to match the same number of molecules just in the vacant cell wall volume (V_{ps}). This yields $c_0 = \frac{V_s}{V_{ps}} \times 1.53 \times 10^{-5} \text{ M} \approx 2 \times 10^{-4} \text{ M}$. As before, the time span is set to 4 hours. The permeation constant is set to reach a depletion of 1% at that time, like in the model comparison experiment.

3.7 Parameter estimation

The final step in the research process combines the mechanisms of inhibition and induction into a probabilistic model of germination from the theory presented so far. Multiple scenarios for the inducer-inhibitor interaction in determining germination are explored. This results in several model variants, rich in free parameters, the values for which cannot be directly obtained from literature. For this reason, recorded data of the germination incidence of *A. niger* [1] and *A. nidulans* [2] are used to estimate the parameters.

3.7.1 Data

The first data set is from the supplemental material of Ijadpanahsaravi et al. [1] and includes the estimated parameters for the germination model by Dantigny [100], obtained from the germination statistics of *A. niger* cultures under 3 types of carbon source in the medium: alanine (Ala), arginine (Arg) and proline (Pro); and at four conidial densities: 3.33×10^4 spores/mL, 6.67×10^4 spores/mL, 1.33×10^5 spores/mL

and 3.67×10^5 spores/mL (converted from 5×10^3 , 1×10^4 , 2×10^4 and 4×10^4 spores in a 150 μL solution, respectively). The Dantigny parameters are p_{\max} (the long-term saturation limit of the germinated fraction), τ_g (the time for half-saturation of the germinated fraction) and ν (a design parameter modelling the heterogeneity of germination times), each provided with a 95% confidence interval. The model constructed from these parameters expresses the probability of germination as

$$p = p_{\max} \left[1 - \frac{1}{1 + \left(\frac{t}{\tau_g} \right)^\nu} \right]. \quad (3.73)$$

Traced over the cultivation time t , this function is nothing more but a cumulative distribution function (CDF) of germination event probabilities over an observed period. Using this data, the temporal course of germination for each inducer type and each spore density. The Dantigny parameters are given for both the onset of swelling and germ-tube formation, of which the former is selected as more relevant to the current study. The germination incidence in the Pro subset is generally the highest, followed by the Ala subset and the Arg subset. In the Arg subset, p_{\max} has an overly large variance and the τ_g parameter is as long as the time of observation, which possibly signals an insufficiently descriptive fit, so only the Ala and Pro subsets are considered.

The second data set is extracted from a publication by Herrero-Garcia et al. [2] on the inhibitory effects of 1-octen-3-ol and other 8-carbon oxylipins in germinating *A. nidulans* cultures. There are two results of interest: germination percentages under varying conidial densities and under exogenously added concentrations of 1-octen-3-ol. The first case examines a wider range of spore densities compared to the previous data set: 6 orders of magnitude increasing from 10^3 spores/mL to 10^8 spores/mL. The germination percentages are given as statistical snapshots at 11 h of incubation, so information about the temporal course is missing. Nonetheless, it is assumed that the authors performed the measurement at a near steady-state of germination, so the values are deemed equivalent to p_{\max} . The same assumption applies to the observations from the second experiment with increasing doses of added 1-octen-3-ol (1, 2.5, 4 and 5 mM).

3.7.2 From deterministic to statistical models

The two models of time-dependent permeation: Equation 3.71 for the inducer and Equation 3.64 for the inhibitor, concern idealised scenarios in which a single spore has exactly defined parameters consistent throughout the entire spore culture. With heterogeneity being a hallmark of aspergilli, the deterministic formulation of these equations needs to be redefined to incorporate variation on many different levels. For each variable, the

number of independent determining factors is so large that a normal distribution can be assumed, according to the Central Limit Theorem (CLT) [121]. If the nature of these variables does not permit negative values, then the log-normal distribution is an appropriate choice, also complying with the CLT [122]. The germination model variants presented below propose different inducer-inhibitor interaction mechanism and gradually introduce random variables with specific distributions as replacement for their deterministic counterparts.

The two criteria for germination, inducer-dependent and inhibitor-dependent, can be expressed as

$$c_{\text{in}}^{\text{inh}} < c_T \quad \text{and} \quad s > s_T, \quad (3.74)$$

where $c_{\text{in}}^{\text{inh}}$ is the residual inhibitor concentration in the spore, c_T is the threshold concentration for inhibition, s is the strength of an inducing signal and s_T is the threshold for this signal. Since it is known that the inducing signals generally operate through the association of molecules to receptor proteins, the signal strength can be related to the concentration of inducer at the receptors, $c_{\text{in}}^{\text{cs}}$ via simple Michaelis-Menten kinetics:

$$s(c_{\text{in}}^{\text{cs}}) = s_{\max} \frac{c_{\text{in}}^{\text{cs}}}{K_{\text{cs}} + c_{\text{in}}^{\text{cs}}}, \quad (3.75)$$

where K_{cs} is a half-saturation concentration constant and s_{\max} is the maximum signal strength. Since the scale of the signal strength is arbitrary, s_{\max} can be set to unity.

3.7.2.1 Independent germination factors

In the most simple scenario, induction and inhibition can be considered entirely independent from each other, with a germination trigger occurring once both criteria from Equation 3.74 are simultaneously fulfilled. This model is denoted as C \wedge I, where C is a symbol for the carbon signal and I for the inhibitor. Expressing both sides of the left inequality in Equation 3.74 through the initial concentration reformulates it to

$$\left(\phi + (1 - \phi)e^{-\frac{t}{\tau(1-\phi)}} \right) c_0 < \gamma c_0 \quad \Rightarrow \quad \phi + (1 - \phi)e^{-\frac{t}{\tau(1-\phi)}} < \gamma. \quad (3.76)$$

The factor on the left-hand side, henceforth abbreviated as β , is the depletion term of the volume-based model and γ is a factor that relates the threshold concentration to a fraction of the initial concentration. Due to physiological differences between spores,

γ is a normal random variable with a mean μ_γ and a standard deviation σ_γ . This implies that each spore has its individual inhibitor depletion threshold. Furthermore, the volume fraction ϕ incorporates two variables - the spore density ρ_s (more or less precisely determined per experiment) and the spore volume V_s . The latter can vary, most notably due to the differences in spore radii within a culture. For this reason, the spore radius R is modelled by a random variable ξ with a mean μ_ξ and a standard deviation σ_ξ .

In the inducer-dependent germination condition (the right inequality in Equation 3.74), the threshold s_T can be analogously treated as a random variable ω with a distribution defined by μ_ω and σ_ω . Furthermore, the inducer concentration that s depends on is a time-dependent variable that obeys Equation 3.71. As in the inhibitor case, this includes the random radius ξ through the volume and area in Equation 3.72, but also the variation of the polysaccharide layer thickness d_{ps} , which can be modelled by a new random variable, κ . The molecular concentrations and permeation constants are considered to have negligible variation and are kept as deterministic variables. The two separate germination probabilities can be expressed through the normal CDFs

$$P(\beta < \gamma | \xi) = 1 - \Phi\left(\frac{\beta(\xi) - \mu_\gamma}{\sigma_\gamma}\right) \quad \text{and} \quad P(s > \gamma) = \Phi\left(\frac{s - \mu_\omega}{\sigma_\omega}\right). \quad (3.77)$$

The combined germination probability comprises the product of the inducer-dependent and the inhibitor-dependent probabilities, whereby all possible values of ξ and κ must be integrated over:

$$p = P(\beta < \gamma | \xi) \times P(s > \gamma), \quad (3.78)$$

$$p = \int_0^\infty \int_0^\infty \Phi\left(\frac{s(\xi, \kappa) - \mu_\omega}{\sigma_\omega}\right) \left[1 - \Phi\left(\frac{\beta(\xi) - \mu_\gamma}{\sigma_\gamma}\right)\right] f_\kappa(\kappa) f_\xi(\xi) d\kappa d\xi. \quad (3.79)$$

$f_\xi(\xi)$ and $f_\kappa(\kappa)$ is the probability density functions (PDFs) of ξ and κ , evaluated at the specific values.

3.7.2.2 Inhibitor-dependent induction

In a second scenario, induction is seen as the primary factor for germination, but its effect is modulated by the inhibitor. This means that the germination-determining criterion only involves the exceedance of the signal threshold s_T , but the role of the inhibitor is in shifting $s_T \equiv \omega$ up or attenuating the signal strength s . The first case can be modelled as

a linear perturbation from a base threshold by an amount proportional to the inhibitor concentration by a factor k :

$$\omega = \omega_0 + k c_{\text{in}}^{\text{inh}}. \quad (3.80)$$

This expression can be substituted for ω in the inducer-dependent probability from Equation 3.77. It is important to note that the inhibitor concentration, $c_{\text{in}}^{\text{inh}} = \beta c_0$, also incorporates a second potentially varying quantity, the initial concentration. Accounting for possible differences in the inhibitor synthesis, c_0 is modelled by the random variable ψ , with a distribution defined by μ_ψ and σ_ψ . Hence, the germination probability of the *inhibitor-dependent induction threshold* model, denoted by $(I \rightarrow T)C$, contains an integral over all three random variable distributions:

$$p = \int_0^\infty \int_0^\infty \int_0^\infty \Phi\left(\frac{s(\xi, \kappa) - k c_{\text{in}}^{\text{inh}}(\xi, \psi) - \mu_{\omega_0}}{\sigma_{\omega_0}}\right) f_\kappa(\kappa) f_\xi(\xi) f_\psi(\psi) d\kappa d\xi d\psi. \quad (3.81)$$

Alternatively, it could be assumed that the inhibitor reduces the signal strength by binding to the receptor proteins or other components further down the signalling pathway. This implies a common Hill-type inhibitor interaction with the signal:

$$s' = s \left[\frac{1}{1 + \left(\frac{c_{\text{in}}^{\text{inh}}(\xi, \psi)}{K_I} \right)^n} \right]. \quad (3.82)$$

The new parameters in this equation are K_I , a signal-halving inhibitor concentration, and n , a Hill coefficient describing the cooperativity of the inhibitor in binding to molecules [123]. The probability for this *inhibitor-dependent induction signal* model, denoted by $(I \rightarrow S)C$, is

$$p = \int_0^\infty \int_0^\infty \int_0^\infty \Phi\left(\frac{s(\xi, \kappa) \left[1 + \left(\frac{c_{\text{in}}^{\text{inh}}(\xi, \psi)}{K_I}\right)^n\right]^{-1} - \mu_{\omega_0}}{\sigma_{\omega_0}}\right) f_\kappa(\kappa) f_\xi(\xi) f_\psi(\psi) d\kappa d\xi d\psi. \quad (3.83)$$

It is conceivable that the inhibitor effect is more complex, affecting both the threshold and the signal simultaneously. In this case, the two cases can be combined in a *general inhibitor-dependent induction* model, denoted by $(I \rightarrow T+S)C$:

$$p = \int_0^\infty \int_0^\infty \int_0^\infty \Phi\left(\frac{s\left[1 + \left(\frac{c_{\text{in}}^{\text{inh}}}{K_I}\right)^n\right]^{-1} - kc_{\text{in}}^{\text{inh}} - \mu_{\omega_0}}{\sigma_{\omega_0}}\right) f_\kappa(\kappa) f_\xi(\xi) f_\psi(\psi) d\kappa d\xi d\psi. \quad (3.84)$$

3.7.2.3 Inducer-dependent inhibition

While having less support by experimental evidence, a scenario could be envisioned in which the effective germination trigger is directly linked to the depletion of the inhibitor, but the complex induction pathway serves to alter the threshold for inhibition or facilitate the release of the inhibitor. The first case is similar to the reciprocal relationship, with the threshold γ being linearly perturbed by the inducing signal from a base value γ_0 :

$$\gamma = \gamma_0 + ks. \quad (3.85)$$

Hence, the *inducer-dependent inhibition threshold* model, denoted by $(C \rightarrow T)I$, has a probability

$$p = \int_0^\infty \int_0^\infty \left[1 - \Phi\left(\frac{\beta(\xi) - ks(\xi, \kappa) - \mu_{\gamma_0}}{\sigma_{\gamma_0}}\right)\right] f_\kappa(\kappa) f_\xi(\xi) d\kappa d\xi. \quad (3.86)$$

Alternatively, the inducing signal may enhance the permeability of the cell wall, e.g. by activating the degradation of cell wall compounds. The simplest way to model this is by multiplying the permeation constant by the signal strength: $P'_s = sP_s^{\text{inh}}$. Thus, the germination probability in the *inducer-dependent inhibitor release* model, denoted by $(C \rightarrow P)I$, is

$$p = \int_0^\infty \int_0^\infty \left[1 - \Phi\left(\frac{\beta(\xi, s) - \mu_\gamma}{\sigma_\gamma}\right)\right] f_\kappa(\kappa) f_\xi(\xi) d\kappa d\xi. \quad (3.87)$$

As before, a combination of the two scenarios is explored, the *general inducer-dependent inhibitor* model, denoted by $(C \rightarrow T+P)I$:

$$p = \int_0^\infty \int_0^\infty \left[1 - \Phi\left(\frac{\beta(\xi, s) - ks(\xi, \kappa) - \mu_{\gamma_0}}{\sigma_{\gamma_0}}\right)\right] f_\kappa(\kappa) f_\xi(\xi) d\kappa d\xi. \quad (3.88)$$

3.7.2.4 Variable permeability model

For simplicity of the calculations, the above models are limited to a number of random variables that necessitate integrals in up to three dimensions. One additional parameter which could exhibit variation is the permeation constant P_s , both for the inducer and for the inhibitor permeation. This could be due to heterogeneities in the cell wall density, uncorrelated with the spore or cell wall volume. Recalling from Equation 3.7 that the permeation constant can be dependent on the porosity α of the cell wall, this variable can also be distributed with a mean μ_α and standard deviation σ_α . This possible model extension is reserved for a secondary stage in which a selection of successful models can be augmented with a variable permeability as means for further improvement.

3.7.2.5 Random variable distributions

The assumed distribution for each random variable introduced above needs to comply with the characteristics of the physical quantity it represents. The more physiologically specific parameters, ξ , κ and ψ , cannot have negative values, so a log-normal distribution is assigned to them. This means that their PDFs have the form

$$f_X(x) = \frac{1}{x\sigma_{\log}\sqrt{2\pi}} \exp\left[-\frac{(\ln x - \mu_{\log})^2}{2\sigma_{\log}^2}\right], \quad x > 0, \quad (3.89)$$

where

$$\mu_{\log} = \ln\left(\frac{\mu_X^2}{\sqrt{\sigma_X^2 + \mu_x^2}}\right), \quad (3.90)$$

$$\sigma_{\log} = \sqrt{\ln\left(1 + \frac{\sigma_X^2}{\mu_X^2}\right)} \quad (3.91)$$

and $\mu_{\log} = \mathbb{E}[X]$ and $\sigma_{\log} = \sqrt{\text{Var}(X)}$.

The thresholds γ and ω are more abstract parameters, so the decision between a normal and a log-normal distribution depends on the question whether negative thresholds are possible. In the case of γ , this would imply that part of the spores never reach the necessary depletion threshold and therefore never germinate. While the reasons for failed germination can be numerous (e.g. genetic defects, physiological damage or locally unfavourable conditions), they can be represented in a negative threshold for inhibitor

depletion, which leads to some spores remaining dormant even when the inhibitor concentration is zero. On the other hand, if part of the ω distribution is negative, some spores would effectively not need any carbon signal to germinate. It has indeed been observed that spores can anomalously germinate in the total absence of an inducing carbon source, albeit in a very low percentage (< 5%) for *A. niger*. For *A. nidulans*, this fraction can reach up to 50% [3]. Therefore, γ and ω can be modelled as normally distributed variables with PDFs

$$f_X(x) = \frac{1}{\sqrt{2\pi}\sigma_X} \exp\left(-\frac{(x - \mu_X)^2}{2\sigma_X^2}\right). \quad (3.92)$$

3.7.3 Equilibrium probabilities

When the available germination data only contains steady-state germination percentages, as in *A. nidulans* case, the time dependence of the models is irrelevant. To reduce calculations, the probability equations can be simplified to represent long-term equilibrium values. For this, the equilibrium concentrations of inhibitor and inducer need to be considered. As $t \rightarrow \infty$, the inhibitor reaches an inhibitor concentration of $c_{\text{eq}} = \phi c_0$, or $c_{\text{eq}} = \phi c_0 + (1 - \phi)c_{\text{eq}}$ when an exogenously added inhibitor is present. In the long-time limit, the concentration of inducer at the receptor proteins is equal to the external inducer concentration $c_{\text{out}}^{\text{cs}}$. This means that the inducing signal strength saturates to a value of

$$s_{\text{eq}} = \frac{c_{\text{out}}^{\text{cs}}}{c_{\text{out}}^{\text{cs}} + K_{\text{cs}}}. \quad (3.93)$$

Furthermore, since the permeation constants only participate via the time-dependent τ term, they can be excluded from the equilibrium calculations.

3.7.4 Parameter ranges

To reduce the number of free parameters, some values are inferred from literature: μ_ξ and σ_ξ have been indicated for *A. niger* and *A. nidulans*, while the κ distribution can be roughly inferred from previous assumptions as $\mu_\kappa = 0.2 \mu\text{m}$ and $\sigma_\kappa = 0.05 \mu\text{m}$. While the initial concentration of inhibitor in the spore is a random variable, the concentration of inducer in the medium is usually a controlled value. In the *A. niger* experiments the concentration of amino acids is noted as 10 mM [1]. For the *A. nidulans* experiments, $c_{\text{out}}^{\text{cs}}$ can be computed by considering that the study uses a minimal medium (MMA) as described in Pontecorvo et al. [124]: including dextrose, of which 10 g are diluted in

1 L of water. Having a molar mass of 180 g/mol, the dextrose has a concentration of approximately 0.0556 M.

To facilitate the search for optimal values, the remaining parameters are constrained to plausible ranges. A special constraint is imposed to all standard deviations to prevent them from becoming larger than their respective means or, in the case of γ and ω , to permit a the maximum percentage of negative thresholds that experimental observations imply. This is done by fitting the exponent δ_X of the coefficient of variation instead of the standard deviation σ_X itself:

$$\delta_X = \ln \left(\frac{\sigma_X}{\mu_X} \right). \quad (3.94)$$

The free parameter bounds are listed in Table 3.4.

Parameter	Range	Units
P_s^{inh}	$(1 \times 10^{-5}, 1 \times 10^{-2})$	$\mu\text{m}/\text{s}$
P_s^{cs}	$(1 \times 10^{-8}, 1 \times 10^{-2})$	$\mu\text{m}/\text{s}$
k	$(10^{-6}, 10^6)$	—
K_I	$(1 \times 10^{-5}, 1.0)$	M
K_{cs}	$(1 \times 10^{-8}, 10.0)$	M
n	$(1.0, 3.0)$	—
s	$(1 \times 10^{-6}, 1.0)$	—
μ_γ	$(1 \times 10^{-8}, 1 \times 10^{-1})$	—
δ_γ	$(-10, -0.5)$	—
μ_ω	$(1 \times 10^{-6}, 10.0)$	—
δ_ω	$(-10, -0.5)$	—
μ_ψ	$(1 \times 10^{-5}, 1.0)$	M
δ_ψ	$(-10, 0)$	—
μ_α	$(1 \times 10^{-4}, 1.0)$	—
δ_α	$(-10, 0)$	—

TABLE 3.4: Free parameter bounds and units.

3.7.5 Fitting the parameters to experimental data

The presented germination models are compared in their capacity to represent the experimental data. To this end, an optimisation procedure is performed on the free parameters to reduce the the root mean square error (RMSE) between the data points and the germination percentages predicted by the model. This is done in two steps. First, an adaptive differential evolution (DE) algorithm with radius-limited sampling [125] is run for 10000 steps, with a population size of 50. The optimal solutions for the parameter values are then fed into a 1000-step secondary optimisation stage using the COBYLA algorithm

(Constrained Optimisation BY Linear Approximation), a derivative-free optimiser for non-linear problems [126]. Multiple optimisation runs are performed by first narrowing down the parameter bounds to see if convergence improves, then expanding them again if some of the parameter limits are reached.

Due to the large computational cost of the nested integrals in the probability calculations, approximations of the normal and log-normal CDFs are made using Gauss-Hermite quadrature [127]. The number of nodes and weights per dimension varies depending on the integral dimensionality and is heuristically determined to balance execution time and accuracy: 216 nodes for single integrals, 36 for double integrals, 10 for triple integrals and 6 for quadruple integrals.

The main criterion for the goodness of fit is the RMSE, but a qualitative inspection also determines whether some of the main characteristics of the data are represented, such as a decrease in germination rate with increasing spore density and an appropriate onset of the germination curve over time. When applicable, the most successful models are combined and subjected to the optimisation procedure again.

This procedure is conducted to its full extent on the *A. niger* data set. Based on its results, the best-fitting germination models or combinations thereof are fitted once again on the *A. nidulans* data for the two scenarios: density-driven inhibition and exogenously driven inhibition. In the second case, the prior external concentration c_{ex} of inhibitor is accounted for in the formulation of the residual concentration, as in Equation 3.63. The parameter estimation is first performed on the germination data driven by spore density, then independently on the exogenously driven germination case. Finally, both subsets are included in the same fitting procedure, in an attempt to minimise the RMSE of the models with parameters applicable to both scenarios simultaneously.

3.8 Julia implementation

All models and numerical experiments are constructed in the Julia programming language and executed from Jupyter notebooks on a Windows 11 desktop PC with a Intel Core i9-13900 CPU, 32 GB RAM and an NVIDIA RTX A4000 GPU. The packages **DataFrames**, **CSV** and **JLD2** are used to store and handle numerical data. For visualisation purposes, the packages **PyPlot** and **GLMakie** are employed. The packages **Statistics** and **Distributions** are used for the definition and evaluation of PDFs and CDFs. The

computation of integrals is performed with the package `QuadGK` or, in the case of Gauss-Hermite approximation, using `FastGaussianCurvature`. The differential evolution algorithm is provided by the package `BlackBoxOptim`, the COBYLA solver — by `NL0pt`. For less demanding model fitting purposes, the package `CurveFit` is used.

The implementation of the lattice-based numerical models involves GPU parallelisation, both for the explicit and for the implicit methods, using Julia’s CUDA-interface. In the forward Euler schemes, this is implemented by computing successive concentration steps in GPU-designated kernel functions, using a 64-bit floating-point precision. The matrix multiplication in the implicit scheme is significantly optimised by the use of sparse matrices, the methods for which are provided by the `CUSPARSE` library. The downside of this approach is that the floating-point precision is limited to 32 bits.

Chapter 4

Results

10-15 pages

4.1 Model comparisons

In comparing the three numerical solvers: the low-resolution, the medium-resolution and the high-resolution model; and the analytical simple permeation model, all models show close alignment under the assumption of a homogeneously distributed inhibitor in the spore, as depicted in Figure 4.1. A pronounced difference is observable in the high-resolution model with excluded protoplast for the inhibitor concentration. Instead of reaching the 1% of its initial concentration at the 4-hour mark, it is released much faster, reaching $c_{in}(4\text{ h}) \approx c_0 \times 10^{-5}$. As the available volume in the full-spore scenario is $V_s = \frac{4}{3}\pi R^3 \approx 65.45 \mu\text{m}^3$, vs. $V_{cw} = \frac{4}{3}\pi(R - d)^3 \approx 38.79 \mu\text{m}^3$ in the wall-restricted scenario, the characteristic release time τ in the latter system is $V_{cw}/V_s \approx 0.6$ times shorter than the one in the first system. However, the wall-restricted system reaches 1% depletion already before the 2-hour mark, possibly due to the additional constraint that molecules may not diffuse into the protoplast. The alignment of the other three cases demonstrates their equal ability to represent simplified molecular release.

The time-dependent concentration values at the two extreme densities from the multi-spore comparison are shown in Figure 4.2. A flattening of the slope is noticeable in the release curve beyond 2 hours for the spore-scale numerical model and the volume-based analytical model. A similar trend does not occur in the high-resolution model, which remains closely aligned with the simple permeation scenario (depletion to 1% at 4 hours). The functional relationship between spore-to-spore distance and concentration at the 1-hour and 4-hour mark is shown in Figure 4.3. The curves look qualitatively similar,

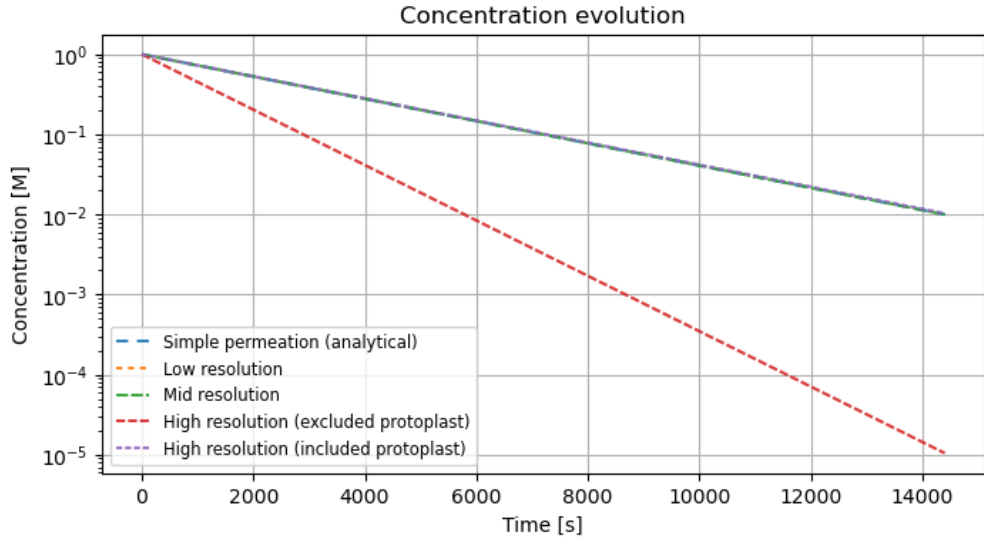


FIGURE 4.1: Comparison of the concentration time course for all inhibitor depletion models in a single-spore setup.

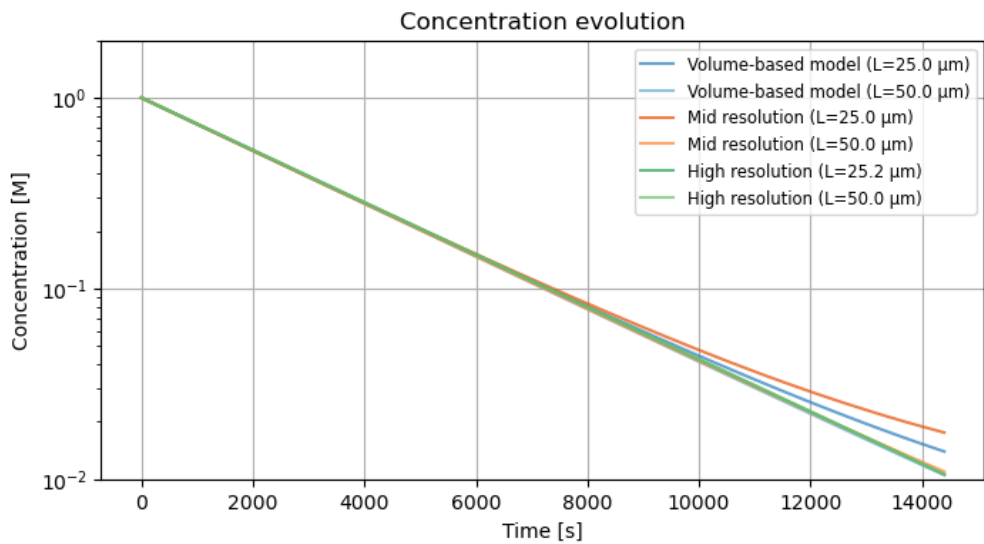


FIGURE 4.2: Comparison of the concentration time course for all inhibitor depletion models in a multi-spore setup.

suggesting that the difference is in a mere scaling factor. Furthermore, the measured concentrations vary by a maximum factor of $5/4$. This is interpreted as sufficient evidence that the volume-based model can be used as a simpler surrogate for the more elaborate simulations of the medium-resolution model.

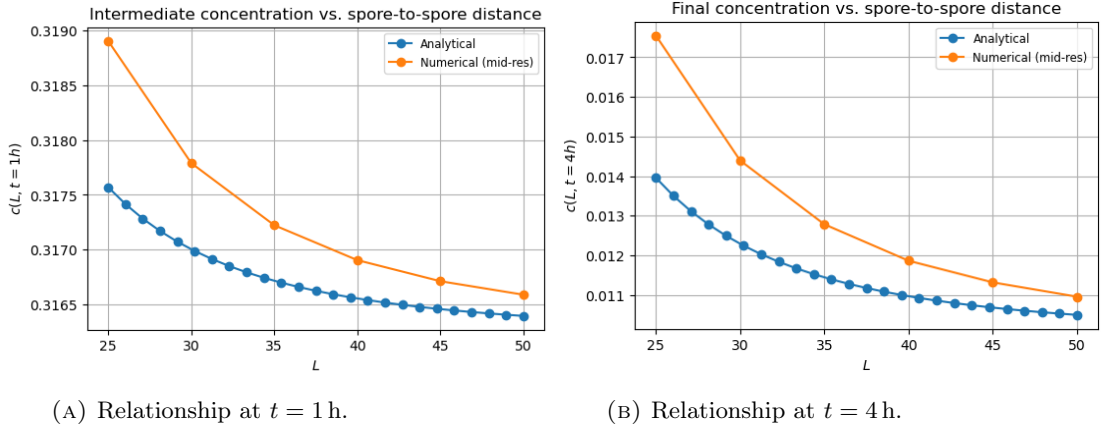


FIGURE 4.3: Spore-to-spore distance versus residual inhibitor concentration for the volume-based analytical model and the medium-resolution numerical model.

4.2 Single-spore experiments

Having validated the models and identified their limitations, the experiments continue by applying them to reality-based scenarios. Using the inferred parameters of the permeation model, the concentration evolutions over time are simulated for different scenarios and depicted in Figure 4.4. As the upper left plot shows, when permeating water and agarose, the concentrations diffuse below 10^{-12} M within 0.01 s — too fast to be captured in the figure. For both thicknesses of the agarose-like polysaccharide barrier, the inhibitor is depleted within less than a second. The hydrophobin layer yields the slowest release, the depletion occurring within 40 s, while the similarly permeable but thinner lipid bilayer results in a depletion within about 20 s. When the permeabilities are combined in the composite barrier scenarios, the release curves are just above similar, depleting just above 40 s to the rate-dominating hydrophobin permeability. When the cell membrane is added to the barrier composition, the depletion happens at nearly 1 min. All of these timings for full inhibitor depletion are very short compared to the time scale of germination onset visible in practice.

The bottom row of Figure 4.4 shows how depletion times, more aligned with the germination times, are produced by fitted permeation constants. The range of thresholds, of magnitude from 10^{-1} to 10^{-5} of the initial concentration $c_0 = 1.53 \times 10^{-5}\text{ M}$, is targeted at $t = 4\text{ h}$ in the bottom left plot and at $t = 2\text{ h}$ in the bottom right plot. The permeation constants found for these scenarios are listed in Table 4.1. Their order varies between 10^{-8} cm s^{-1} and 10^{-7} cm s^{-1} , at least a hundred times smaller than the least permeable composite barrier. The adsorption parameters inferred from literature account for a much less dramatic decrease in permeability, so in this formulation adsorption is not sufficient to explain the slow release.

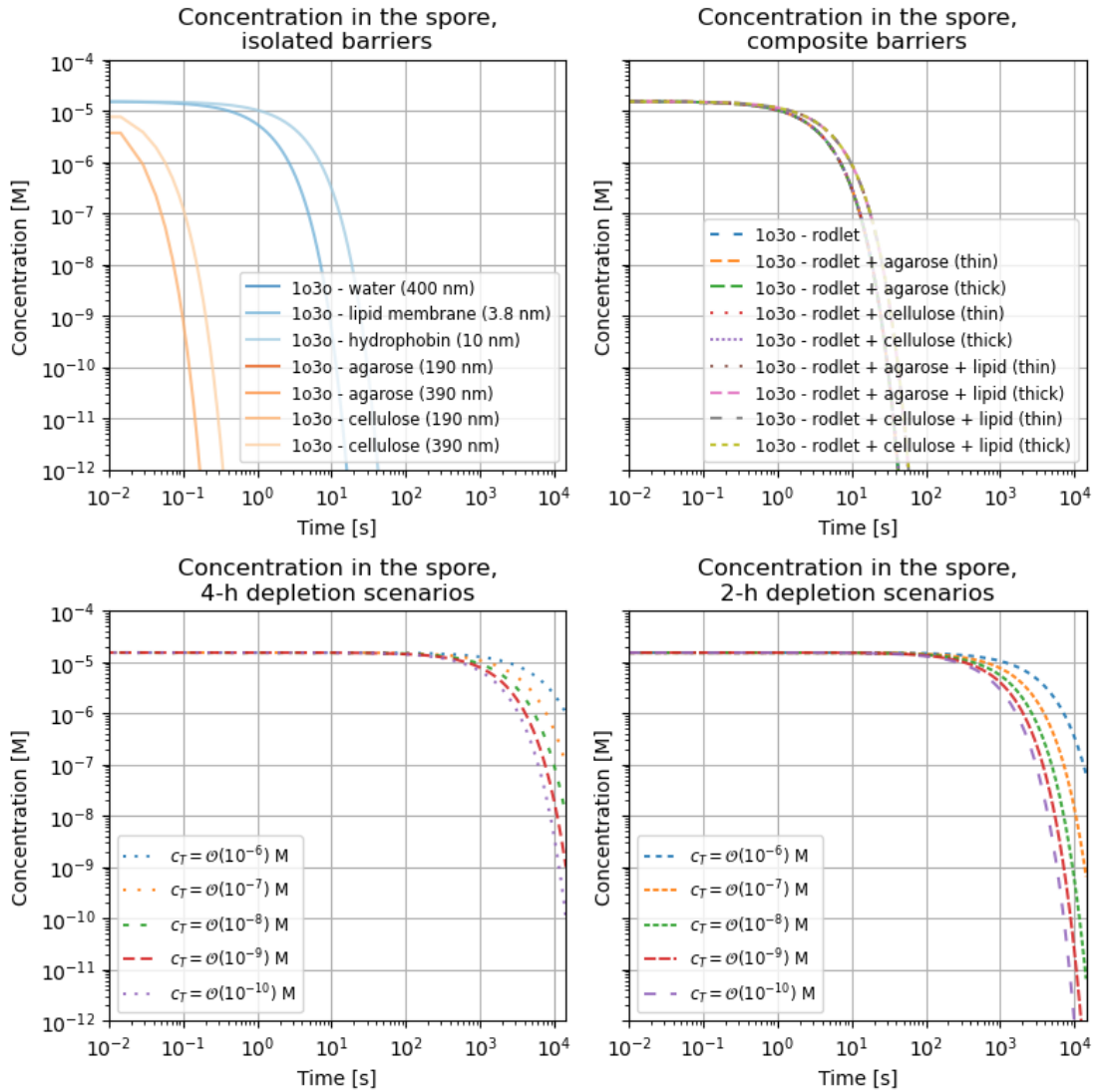


FIGURE 4.4: Results from the single-spore experiments, plotted on a log-log scale. Top row: internal concentration evolutions for 1-octen-3-ol permeating simple-material barriers (left) and composite barriers (right). The curves for 1-octen-3-ol through water and 1-octen-3-ol through agarose decay too fast to be shown on the logarithmic axis. Bottom row: internal concentration evolutions for a hypothetical permeation reaching thresholds of different magnitude at 4 hours of incubation (left) and at 2 hours of incubation (right).

c_T	P_s (4-hour depletion)	P_s (2-hour depletion)
$c_0 \times 10^{-1}$	$1.579 \times 10^{-8} \text{ cm s}^{-1}$	$3.157 \times 10^{-8} \text{ cm s}^{-1}$
$c_0 \times 10^{-2}$	$2.911 \times 10^{-8} \text{ cm s}^{-1}$	$5.822 \times 10^{-8} \text{ cm s}^{-1}$
$c_0 \times 10^{-3}$	$4.244 \times 10^{-8} \text{ cm s}^{-1}$	$8.487 \times 10^{-8} \text{ cm s}^{-1}$
$c_0 \times 10^{-4}$	$5.576 \times 10^{-8} \text{ cm s}^{-1}$	$1.115 \times 10^{-7} \text{ cm s}^{-1}$
$c_0 \times 10^{-5}$	$6.909 \times 10^{-8} \text{ cm s}^{-1}$	$1.382 \times 10^{-7} \text{ cm s}^{-1}$

TABLE 4.1: Permeation constants fitted to produce a 4-hour and a 2-hour depletion of the internal inhibitor to different threshold values.

4.3 Multi-spore experiments

The relationship between spore density, inhibitor saturation and deceleration of the inhibitor release is elucidated in the experiments with the medium-resolution model and the volume-based model. The analytical formula from Equation 3.55 allows the calculation of the equilibrium concentration in the spore at long incubation times, according to the volume-based model. Figure 4.5 shows that the numerical model arrives quite close to it, with a slight overestimation, possibly due to numerical error from the discretisation. Two regimes can be identified in the concentration curves. At early times, the concentration follows an exponential decrease, as indicated by the linear behaviour on the semi-logarithmic plots. The exponent of this decrease can be measured by fitting a model of the form $y = ae^\varepsilon$ to a range of early-time concentrations — in this case, the period $t \in [0, 600]$ s. As expected, the resulting exponent ε is correlated with the permeability P_s , which dictates the characteristic release time τ . Within a certain time period, the concentration curve undergoes a transition from an exponential decrease to a flattening trend towards an asymptotic limit. The magnitude of the steady-state value is markedly dependent on the spore density, increasing from 10^{-7} M at $\rho_s = 9.946 \times 10^3$ spores/mL to more than 10^{-2} M at $\rho_s = 1.25 \times 10^8$ spores/mL.

The results therefore confirm that conidial density affects the inhibitor saturation in the medium and that the approach to this saturation is dependent on the cell wall permeability. It is also interesting to observe whether the spore density has an additional effect on the inhibitor release at early times ($t < 10$ min). Figure 4.6 takes a closer look at the interaction between P_s and ρ_s in affecting the exponent of concentration decrease during this period. In the limit of $\rho_s \rightarrow 0$, the release follows the simple permeation model $c_{\text{in}} = c_0 e^{-t/\tau}$, so to normalise the exponent, one needs to multiply it by $-\tau = -\frac{V_s}{AP_s}$. In all observed permeability scenarios, the low-density spore cultures exhibit an early-time release aligned with simple permeation. As ρ_s increases, the normalised exponent itself reduces exponentially, as indicated by the linear trend on the double logarithmic plots on the left-hand side of the figure. Interestingly, despite normalising the effect of P_s by multiplying the exponent by τ , there is a slight difference between the normalised exponent at high conidial density as the permeability changes. For $P_s = 0.0014 \mu\text{m s}^{-1}$, the exponent is just below 0.99, while, for $P_s = 0.0008 \mu\text{m s}^{-1}$, the exponent has increased by about 0.001. This clearly reflects the role of the $(1 - \phi)$ term in the release exponent in Equation 3.64. In this analysis, the numerical and the analytical model exhibit alignment within an acceptable tolerance.

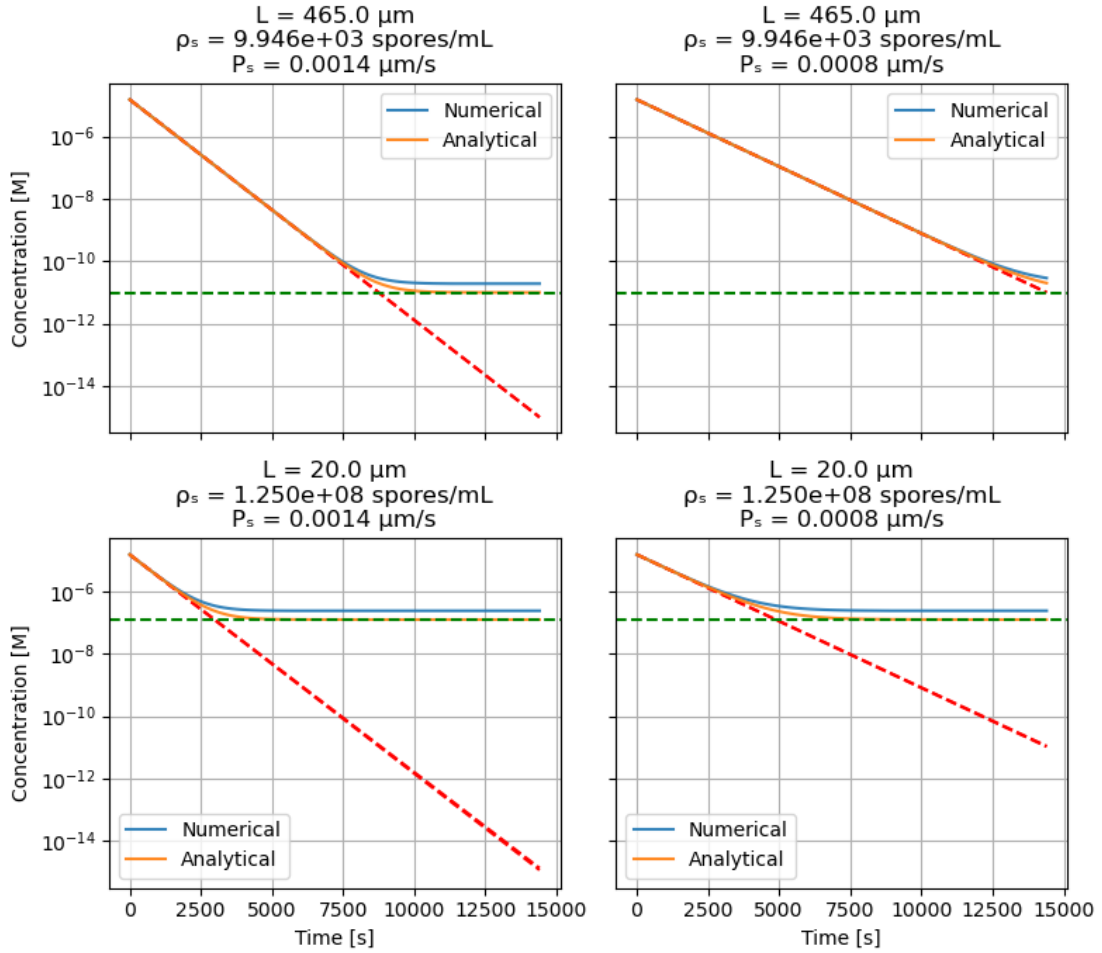


FIGURE 4.5: Time courses of the internal inhibitor concentration for the extreme values of the tested permeation constants (P_s) and spore densities (ρ_s), corresponding to spore-to-spore distances (L) in the multi-spore experiments. The green dashed lines indicate the equilibrium concentration in the spore according to the volume-based model. The red dashed lines indicate the fitted exponential law in the early time of release (first 10 min).

4.4 Spore cluster experiments

Having established that the global density of the spore culture affects the release of the inhibitor, it remains to be tested whether the local density of tight spore clusters has a diffusion-limiting influence. Snapshots of the inhibitor concentration distribution at different times, for a single spore and for a 13-spore cluster, with the protoplast region included and excluded from diffusion, are presented in Figure 4.7. The inhibitor appears to equilibrate fast in the medium, as indicated by the homogeneous ambient colour. The concentration in the case of a cell wall restricted distribution diffuses into the medium faster, as was already indicated during the model validation. However, the dense clusters do not appear to retain much more inhibitor compared to the single spore.

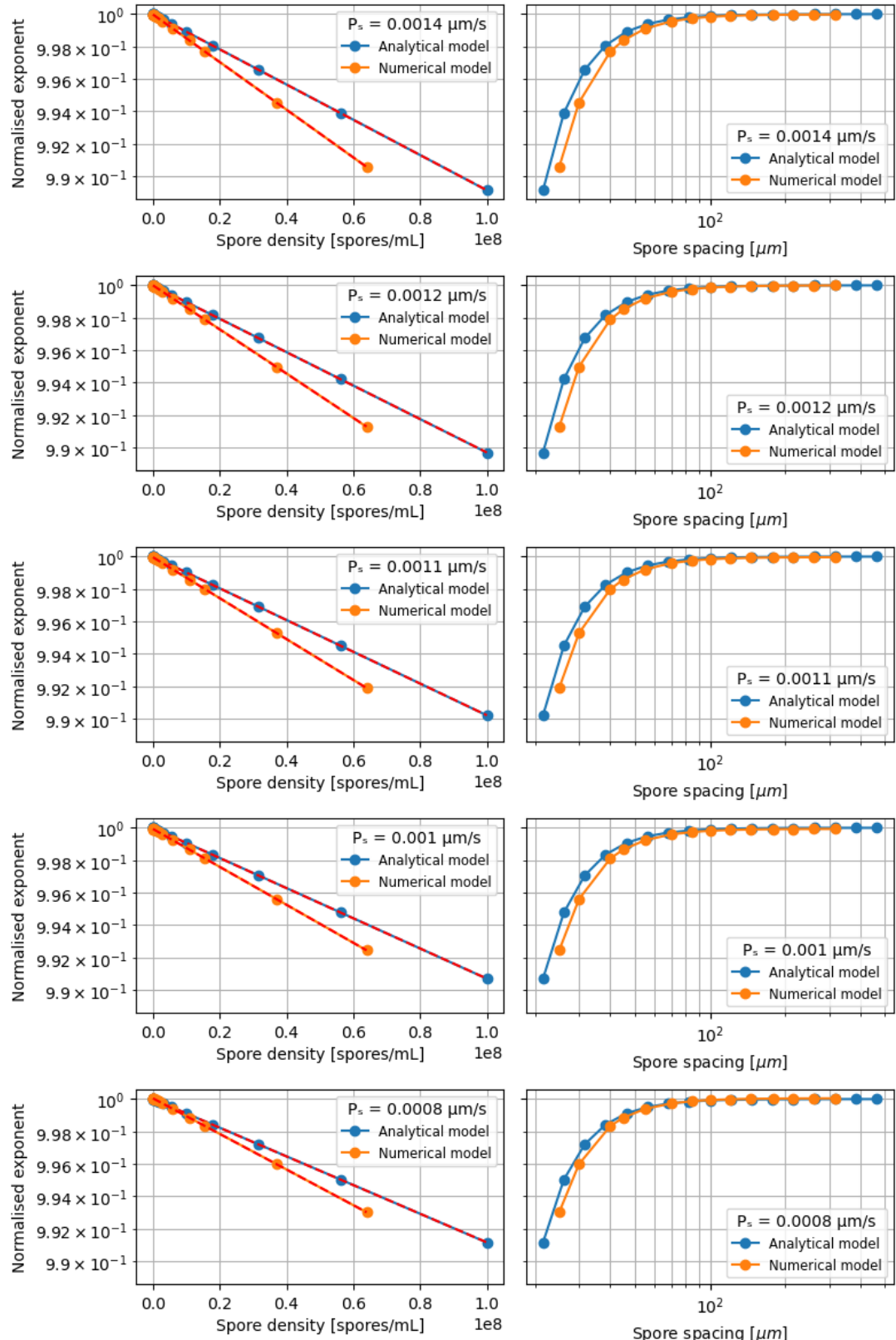


FIGURE 4.6: Analysis of the early-time release exponent for different permeation constants (P_s). Left: relationship between spore density and the normalised exponent (semi-logarithmic plot). Right: relationship between spore-to-spore distance and the normalised exponent (double-logarithmic plot).

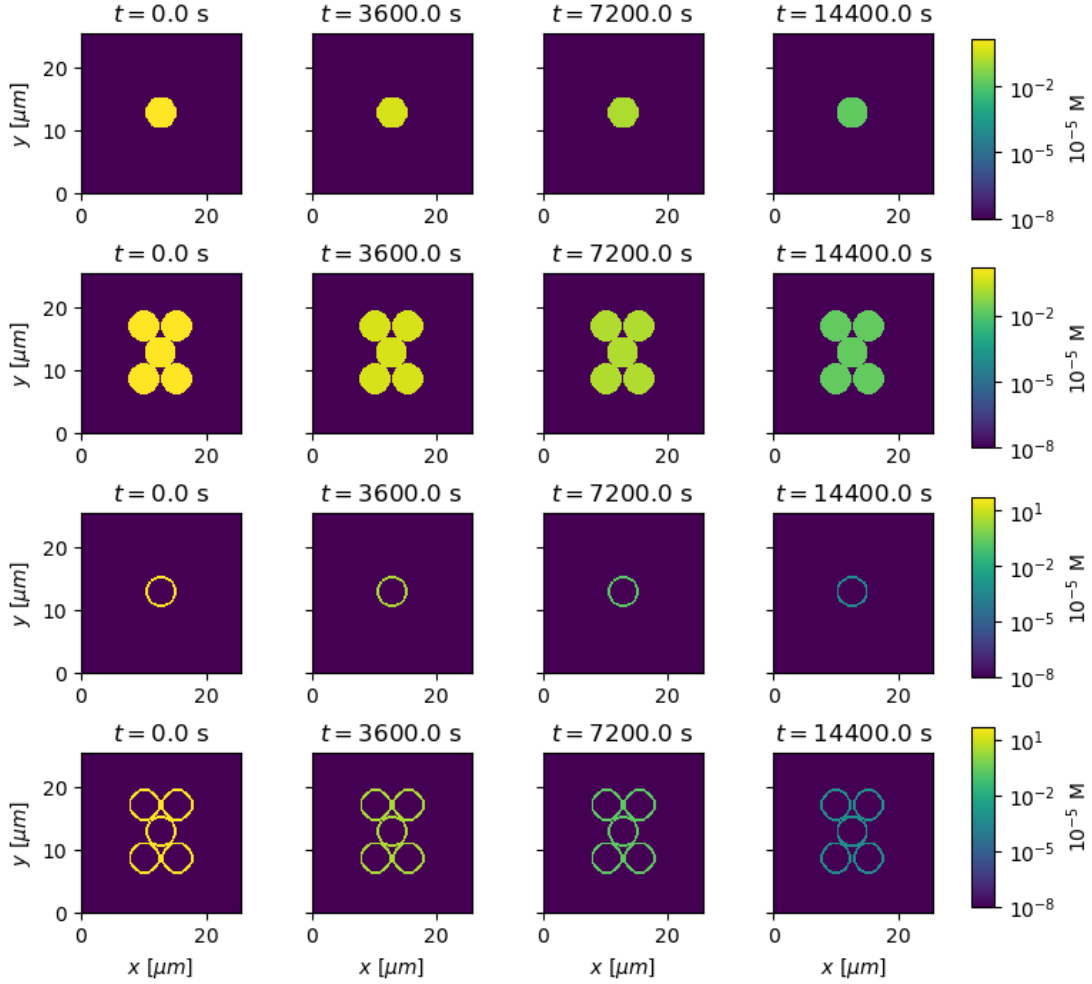


FIGURE 4.7: Cross-sections through the 3D lattice at different moments in time, with colour gradients indicating the inhibitor concentration. Top two rows: simulations with a full-spore inhibitor distribution. Bottom two rows: simulations with a protoplast excluded from diffusion.

The course of the average concentration in the single spore and in the central spore of the cluster is depicted in Figure 4.8. Since the inhibitor molecules are distributed in a smaller volume, the starting concentration in the excluded protoplast scenario is higher, but nonetheless drops faster than the full-spore scenario. A small difference is noticeable between the final concentration in the single-spore and in the dense-cluster scenarios. In the full-spore scenario, the dense cluster leaves about 7.6% more concentration in the central spore compared to the single spore. In the excluded-protoplast scenario, this difference is about 20%.

Additional experiments show that this slight diffusion-obstructing effect only applies when the spores are in direct contact, i.e. when they have at least one pair of adjacent cell wall lattice nodes. If there is as much as one medium node separating two spores, there is no measurable difference between the single-spore and the spore-cluster scenarios.

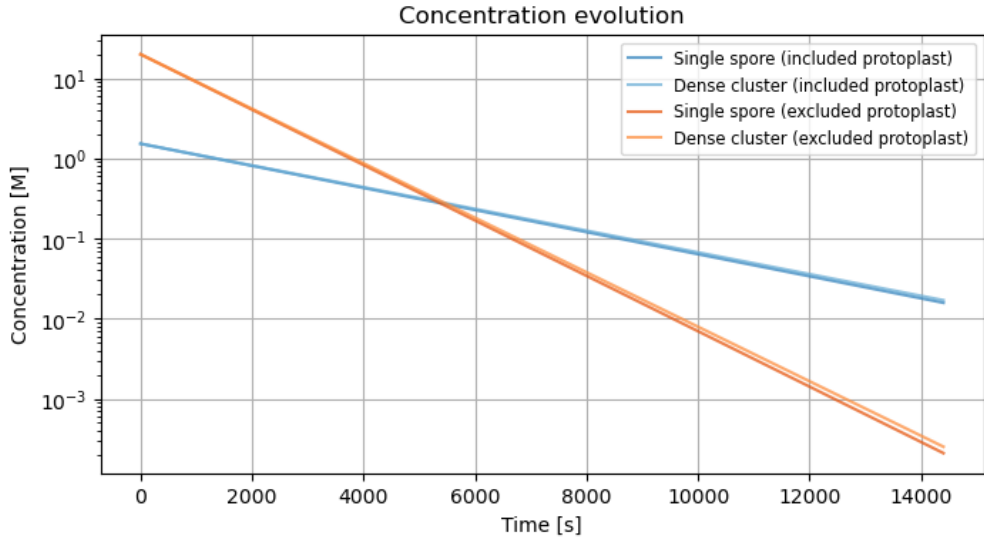


FIGURE 4.8: Time course of the internal inhibitor concentrations for the cases illustrated in Figure 4.7.

This implies that the simulations of spore clusters possibly redistribute the cell wall concentrations from one spore to another, effectively forming a conjoined inhibitor source with less interface area towards the medium. In conclusion, while the released inhibitor quickly diffuses through the cluster cavities, a small reduction of the inhibitor release is possible if the spores increase the surface of physical contact. As this reduction is not of an entire order, the effect of clusters is not considered significant enough to be included in the germination probability models.

4.5 Parameter estimation

4.5.1 Basic models and *A. niger* data

The parameter estimation is performed on *A. niger* data with varying success depending on the germination model variant. The C \wedge I model exhibits the closest fit, with an RMSE of 0.0573. The decline in germination probability with an increasing conidial density is accurately represented in the top plot of Figure 4.9a. The time courses of the germination probability for the Ala inducer bear closer resemblance to the Dantigny sigmoids than for the Pro inducer. While the density-dependent germination curve for Ala is lower than that for Pro, the difference is not as pronounced as in the data set and seems to decrease for large densities, contrary to the data trend.

Of all germination scenarios triggered by induction, (I \rightarrow T)C exhibits the lowest RMSE (0.0699), as seen in Figure 4.9c. In all time-course comparisons, the onset of germination

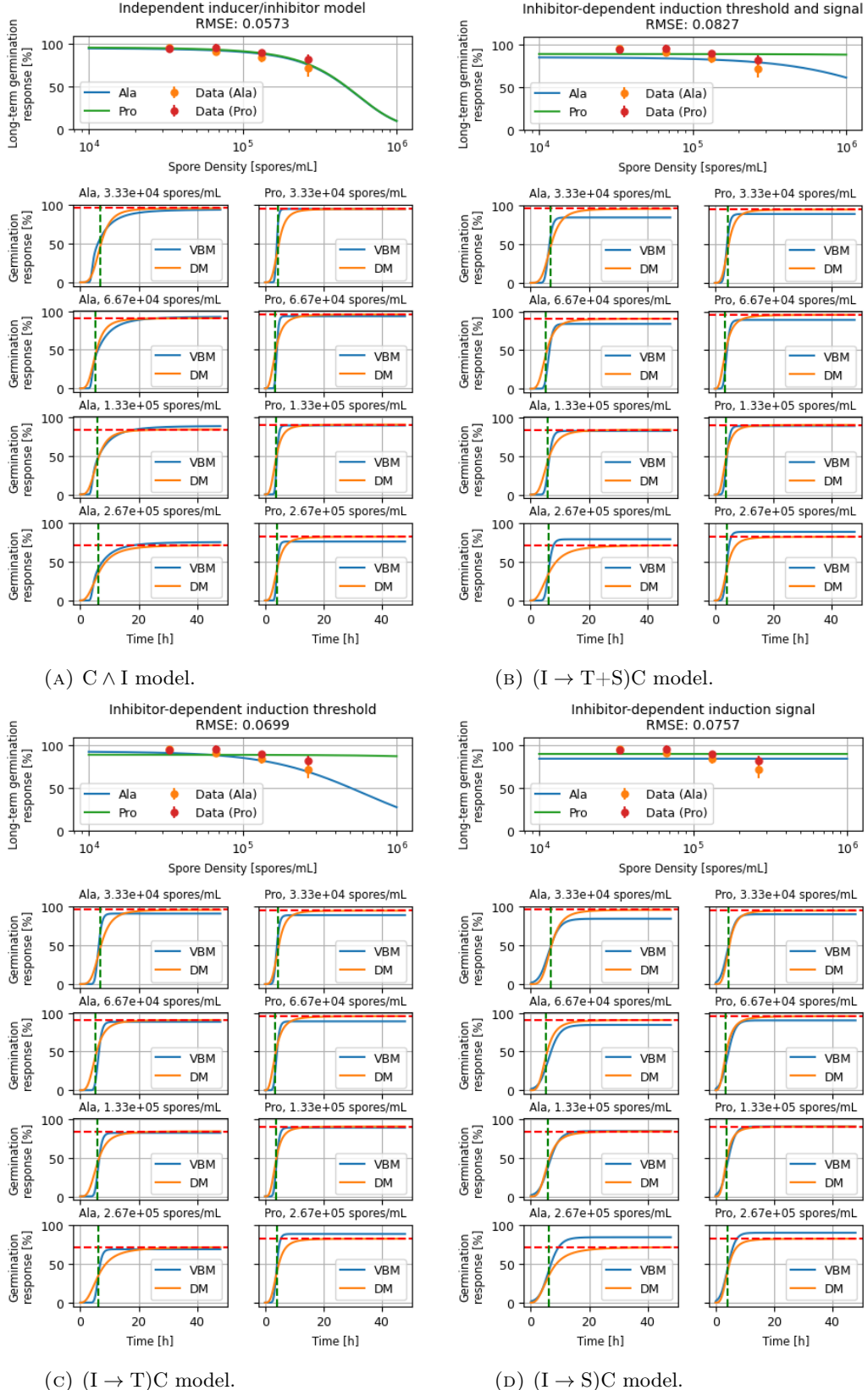


FIGURE 4.9: *A. niger* germination data vs. germination probabilities predicted by the models. Top: density-dependent long-term germination probability (p_{\max}). Bottom: time-dependent germination probability of the volume-based model (VBM) vs. the Dantigny model (DM), with p_{\max} (red dashed line) and τ_g (green dashed line).

is markedly steeper than the Dantigny curve. The stationary germination rate for Ala follows the data points closely, unlike the one for Pro, which remains almost flat for all spore densities. A lack of responsiveness to density is noticeable for both inducers in the case of the $(I \rightarrow S)C$ model, as Figure 4.9d suggests. On the other hand, the slopes of the time-dependent germination onset are much more aligned with the Dantigny curves compared to the previous model. Overall, this results in an RMSE of 0.0757. In the combined model, $(I \rightarrow T+S)C$, the fit is worse than both scenarios with separate inhibitor effects (RMSE of 0.0827), signalling a bad compromise of parameters for a combined threshold and signal modulation. This implies that the parameters for which an inhibitor-dependent induction threshold explains germination are not the same as those for which an inhibitor-dependent induction signal explains germination. The case in which the carbon signalling threshold is shifted by inhibition seems the most plausible of the three variants in this category.

If germination is considered triggered by inhibitor depletion, the fitness of the models is generally worse than in the previous two categories, with an RMSE of 0.129 for $(C \rightarrow T)I$, 0.0787 for $(C \rightarrow P)I$ and 0.114 for $(C \rightarrow T+P)I$. The assumptions of an inducer-dependent inhibition threshold (Figure 4.10a) and an inducer-dependent inhibitor threshold and release (Figure 4.10c) fail to represent any density-dependent modulation of the germination probability, even though the slopes of the time-dependent germination onset are not too dissimilar from the Dantigny curves. If the permeation of inhibitor is regulated by the inducer (Figure 4.10b), the density-dependence is represented but does not vary between Ala and Pro, and the time-dependent curves are markedly steeper than the Dantigny curves. Overall, the $(C \rightarrow P)I$ model has the most explanatory power of all three variants, with an RMSE of 0.0787, but is still more flawed compared to the other model categories.

Comparing the RMSE, the $C \wedge I$ model and the $(I \rightarrow T)C$ model exhibit the best performance. It is therefore decided that the model with two independent germination factors are combined with the models from the inhibitor-dependent induction family.

4.5.2 Combined models

First, the $(I \rightarrow T)C$ is modified, such that the inhibitor both shifts the induction threshold and additionally co-determines germination when it reaches the depletion threshold. This results in the $(I \rightarrow T)C \wedge I$ model with a germination probability defined as

$$p = \int_0^\infty [1 - \Phi(z_\gamma)] \int_0^\infty \int_0^\infty \Phi\left(\frac{s - kc_{in}^{inh} - \mu\omega_0}{\sigma_{\omega_0}}\right) f_\kappa(\kappa) f_\psi(\psi) f_\xi(\xi) d\kappa d\psi d\xi, \quad (4.1)$$

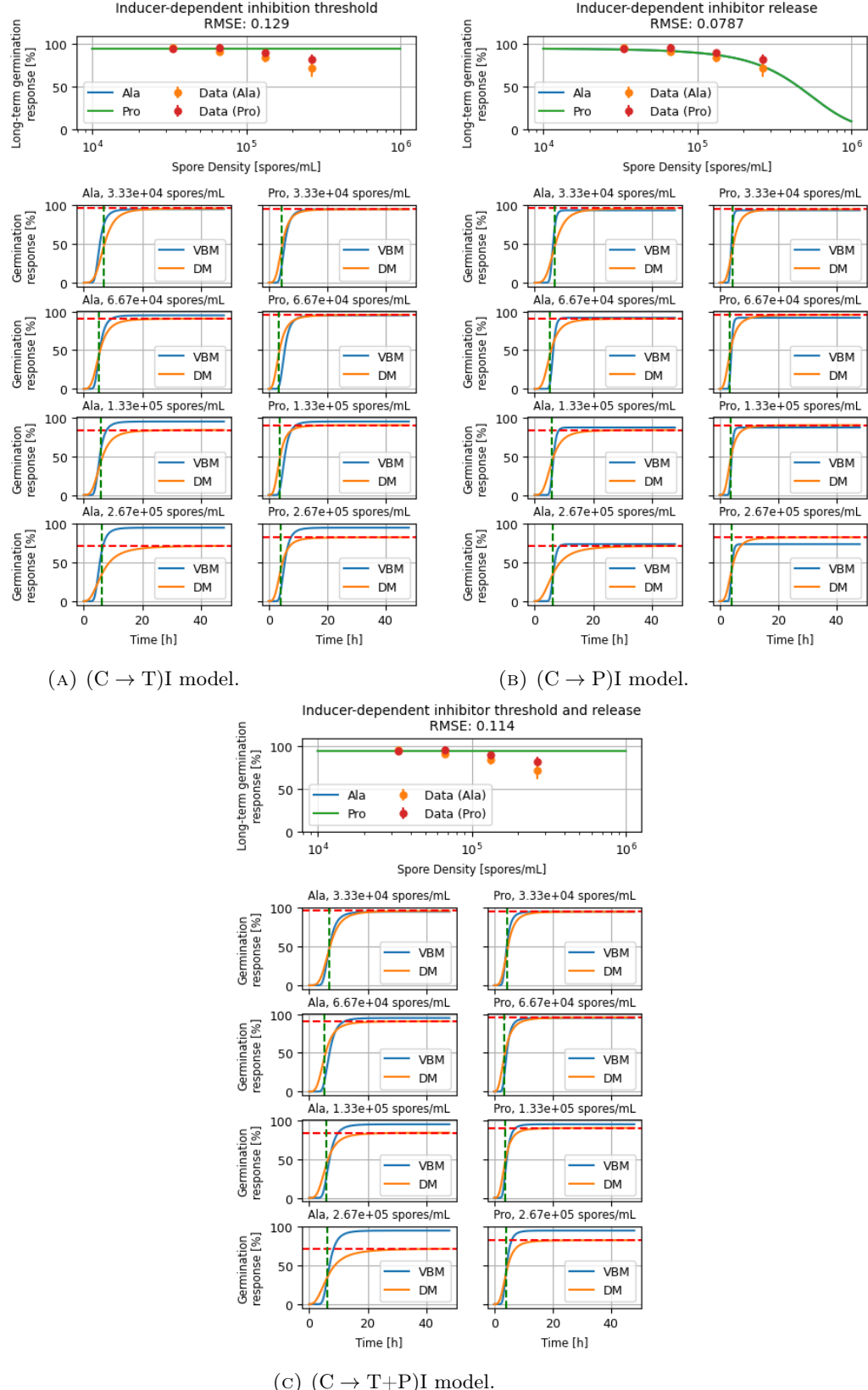


FIGURE 4.10: *A. niger* germination data vs. germination probabilities predicted by the models. Top plots: density-dependent long-term germination probability (p_{\max}). Bottom plots: time-dependent germination probability of the volume-based model (VBM) vs. the Dantigny model (DM), with p_{\max} (red dashed lines) and τ_g (green dashed lines).

where

$$z_\gamma = \frac{\beta - \mu_\gamma}{\sigma_\gamma}. \quad (4.2)$$

The results from its parameter estimation can be seen in Figure 4.11a. Its RMSE is higher than in its two predecessor models (0.0751) and it suffers a similar lack of sensitivity to spore density in the Pro case as the $(I \rightarrow T)C$ model.

In another explored combination, $(I \rightarrow S)C \wedge I$, the inhibitor modulates the induction signal and additionally co-determines germination by reaching its threshold. According to this combined model, the germination probability is

$$p = \int_0^\infty [1 - \Phi(z_\gamma)] \int_0^\infty \int_0^\infty \Phi(z_\omega) f_\kappa(\kappa) f_\psi(\psi) f_\xi(\xi) d\kappa d\psi d\xi, \quad (4.3)$$

where

$$z_\omega = \frac{s \left[1 + \left(\frac{c_{in}^{inh}}{K_I} \right)^n \right]^{-1} - \mu_\omega}{\sigma_\omega}. \quad (4.4)$$

This model yields the lowest RMSE so far (0.0564), correctly accentuating the difference between the density-dependent germination curves of Ala and Pro in Figure 4.11b. The time-dependent curves in the Ala case exhibit a close match with the Dantigny function, while in the Pro case they have a slightly higher onset steepness.

Finally, the model with a combined inhibitor effect on the induction threshold and signal is augmented with an inhibitor-dependent germination condition. This model, $(I \rightarrow T+S)C \wedge I$, computes the germination probability as

$$p = \int_0^\infty [1 - \Phi(z_\gamma)] \int_0^\infty \int_0^\infty \Phi(z_{\omega_0}) f_\kappa(\kappa) f_\psi(\psi) f_\xi(\xi) d\kappa d\psi d\xi, \quad (4.5)$$

where

$$z_{\omega_0} = \frac{s \left[1 + \left(\frac{c_{in}^{inh}}{K_I} \right)^n \right]^{-1} - kc_{in}^{inh} - \mu_{\omega_0}}{\sigma_{\omega_0}}. \quad (4.6)$$

The parameter estimation result using this model is less optimal than the previous two combinations, judging by its RMSE (0.0818). As seen in Figure 4.11c, this is more likely due to discrepancies in the the time-dependent curves than in the density-dependent

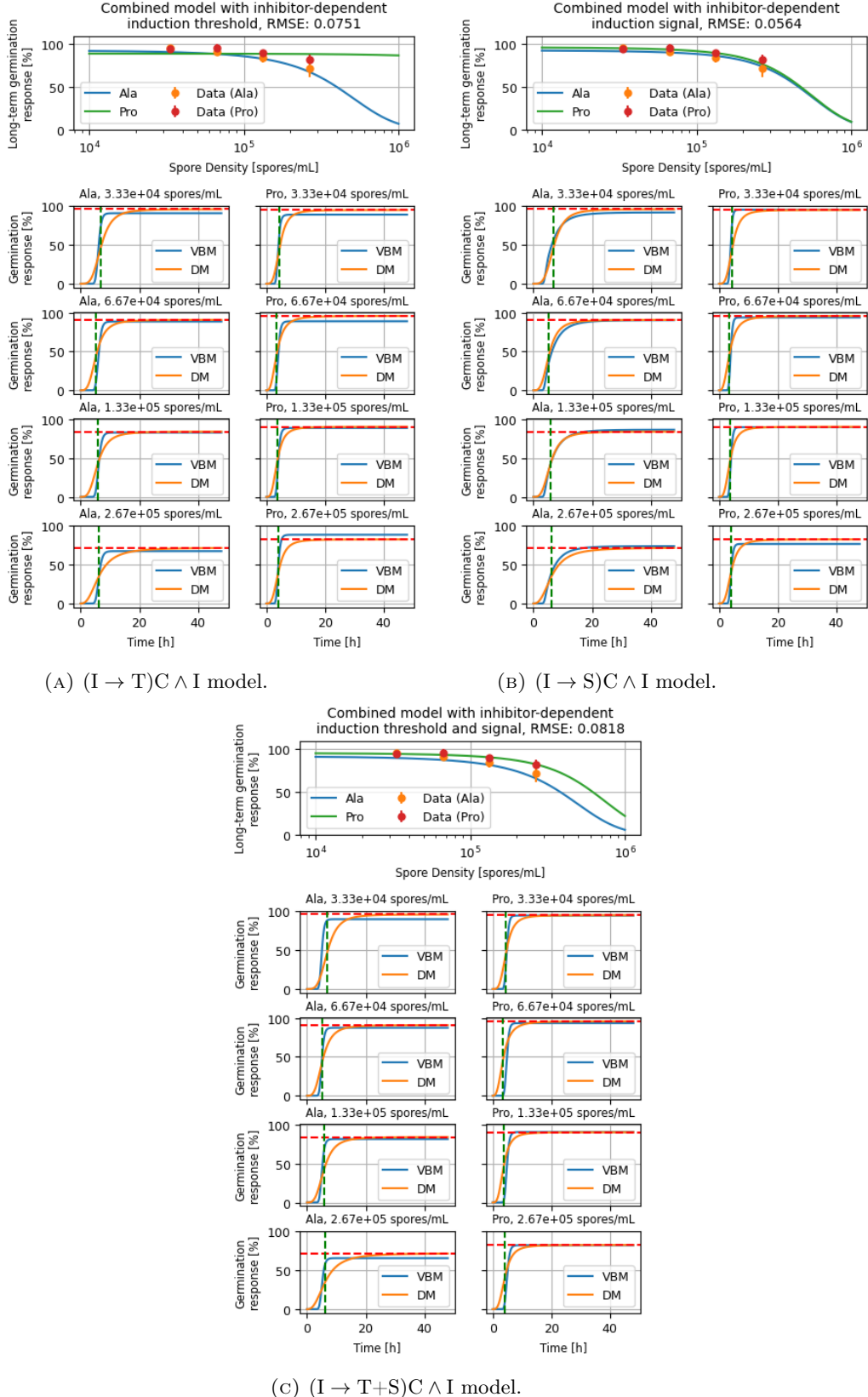


FIGURE 4.11: *A. niger* germination data vs. germination probabilities predicted by the models. Top plots: density-dependent long-term germination probability (p_{\max}). Bottom plots: time-dependent germination probability of the volume-based model (VBM) vs. the Dantigny model (DM), with p_{\max} (red dashed lines) and τ_g (green dashed lines).

curves. The latter show a qualitatively good match to the data, with the Ala and Pro curves having more similar values at low densities and diverging at higher densities.

Overall, the two-factor germination with an inhibitor-dependent induction signal ($(I \rightarrow S)C \wedge I$) exhibits the best fit, while the two-factor germination with both an inhibitor-dependent induction threshold and signal ($(I \rightarrow T+S)C \wedge I$) captures some important characteristics of the density-dependent germination data. The estimated parameters in every combined model are listed in Appendix A: [Estimated Parameters](#), Table A.1 and interpreted in the [Discussion](#) section.

4.5.3 Models with variable permeability

The fact that many time-dependent germination curves exhibit an onset steeper than the Dantigny sigmoid indicates that the germination times are insufficiently spread out, i.e. that there should be a larger heterogeneity in the timing of germination events. One additional parameter which can influence this variance is the cell wall porosity α , linked to the permeability P_s . This offers a chance to improve the performance of the models with promising characteristics: the simply framed $C \wedge I$ model and all the combined models with inhibitor-dependent inducer, $(I \rightarrow T)C \wedge I$, $(I \rightarrow S)C \wedge I$ and $(I \rightarrow T+S)C \wedge I$.

In the model with independent germination factors, the variation in α improves the RMSE to 0.0538. As Figure 4.12a indicates, the difference between Ala and Pro in density-driven inhibition is pronounced, albeit at low spore densities, and the time-dependent curves exhibit a close match with the Dantigny model. If both inhibition and induction are germination-determining but the inducer signal and threshold are additionally modulated by inhibition, the model yields an even lower RMSE (0.0478), as seen in Figure 4.12b. If only the induction threshold is affected, Figure 4.12c indicates a slightly higher RMSE (0.0485). If only the induction signal is affected, the lowest RMSE of all models is obtained (0.0379). However, Figure 4.12d indicates that the contribution to this is mainly from the alignment of the time-dependent curves and less so from the density-dependent relationship. Thus, the three models with a two-factor germination criterion and an inhibitor-dependent induction appear most valid. The fitted parameters for the series with variable cell wall porosity are listed in Table A.2.

4.5.4 Selected models and *A. nidulans* data

The three model variants with greatest ability to explain the *A. niger* data, $(I \rightarrow T)C \wedge I$, $(I \rightarrow S)C \wedge I$ and $(I \rightarrow T+S)C \wedge I$, are selected for the fitting procedure on *A. nidulans* data. As the set comprises steady-state germination percentages only, the long-term

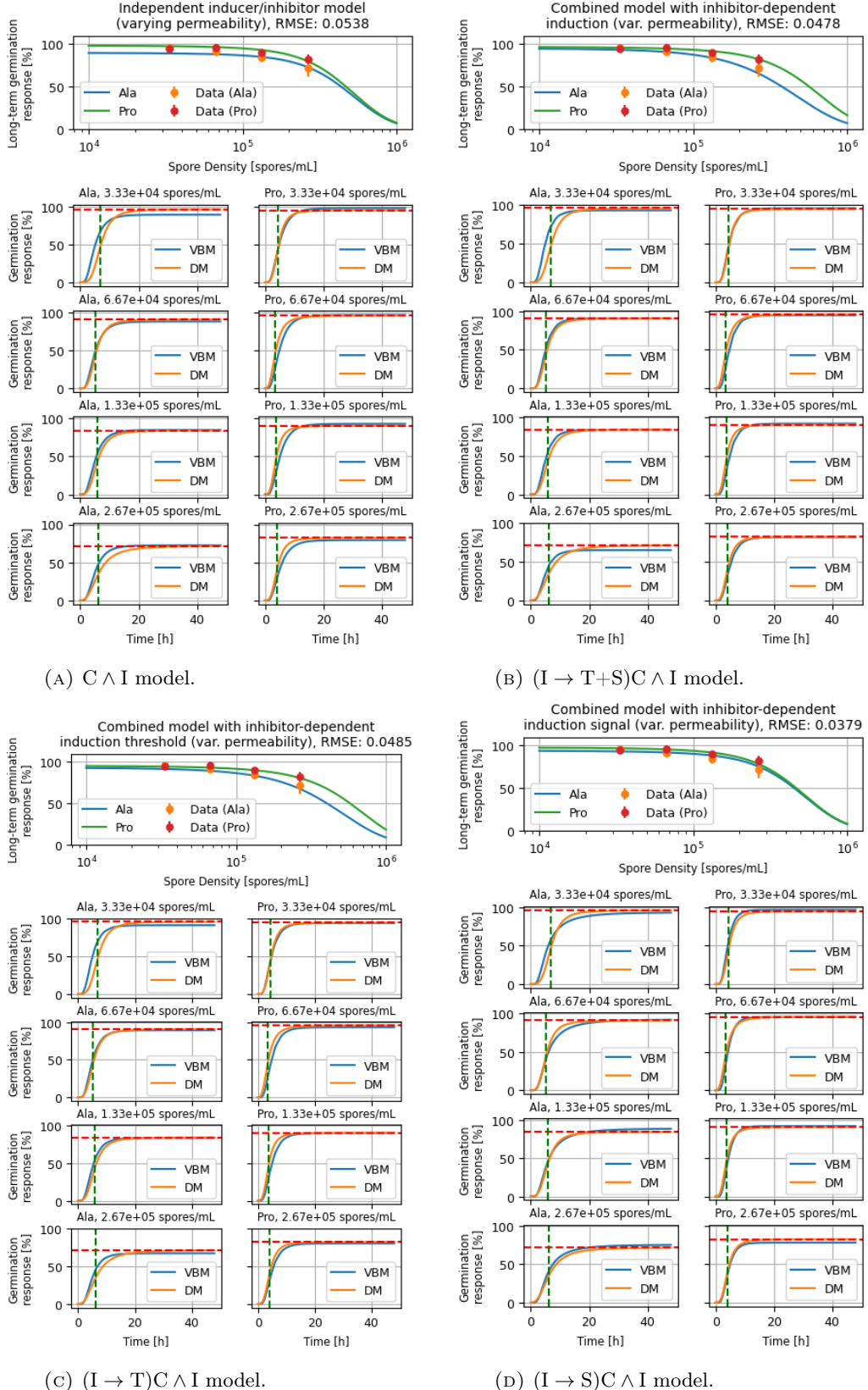


FIGURE 4.12: *A. niger* germination data vs. germination probabilities predicted by the models with variable α . Top plots: density-dependent p_{\max} . Bottom plots: time-dependent germination probability of the volume-based model (VBM) vs. the Dantigny model (DM), with p_{\max} (red dashed lines) and τ_g (green dashed lines).

FIGURE 4.13: *A. niger* germination data vs. germination probabilities predicted by the models with variable α . Top: density-dependent long-term germination probability (p_{\max}). Bottom: time-dependent germination probability vs. Dantigny curves.

equilibrium formulas are used. Furthermore, to account for the subset with exogenously added 1-octen-3-ol, the full concentration expression from Equation 3.63 (involving the variable c_{ex}) is used in deriving the equilibrium probabilities.

In the case of $(I \rightarrow T)C \wedge I$, the equilibrium probability is

$$p_{\text{eq}} = \int_0^\infty \int_0^\infty [1 - \Phi(z_{\gamma,\text{eq}})] \Phi(z_{\omega_0,\text{eq}}) f_\psi(\psi) f_\xi(\xi) d\psi d\xi. \quad (4.7)$$

With consideration of c_{ex} , the z -variables take the form

$$z_{\gamma,\text{eq}} = \frac{\phi + (1 - \phi) \frac{c_{\text{ex}}}{\psi} - \mu_\gamma}{\sigma_\gamma}, \quad z_{\omega_0,\text{eq}} = \frac{s_{\text{eq}} - k [\phi\psi + (1 - \phi)c_{\text{ex}}] - \mu_{\omega_0}}{\sigma_{\omega_0}}. \quad (4.8)$$

When an exogenous inhibitor concentration is not considered, the expression can be simplified by setting $c_{\text{ex}} = 0$. For $(I \rightarrow S)C \wedge I$, the equilibrium germination probability also follows Equation 4.7, but with

$$z_{\omega_0,\text{eq}} = \frac{s_{\text{eq}} \left[1 + \left(\frac{[\phi+(1-\phi)\frac{c_{\text{ex}}}{\psi}]\psi}{K_I} \right)^n \right]^{-1} - \mu_{\omega_0}}{\sigma_{\omega_0}}. \quad (4.9)$$

For $(I \rightarrow T+S)C \wedge I$, the z -value for the inducer criterion is

$$z_{\omega_0,\text{eq}} = \frac{s_{\text{eq}} \left[1 + \left(\frac{[\phi+(1-\phi)\frac{c_{\text{ex}}}{\psi}]\psi}{K_I} \right)^n \right]^{-1} - k [\phi\psi + (1 - \phi)c_{\text{ex}}] - \mu_{\omega_0}}{\sigma_{\omega_0}}. \quad (4.10)$$

The comparisons between fitted models and data are displayed in Appendix B: [Fitting Models To *A. nidulans* Data](#). Fitting the $(I \rightarrow T)C \wedge I$ model to the data with density-driven inhibition yields a curve which seems to accurately capture the transition from high to low germination between 10^6 and 10^7 spores/mL, with an RMSE of 0.0554 (Figure B.1a). When fitted separately to the data with exogenously added 1-octen-3-ol, an even better fit is revealed, with an RMSE of 0.00336 (Figure B.1b). However, when trying to explain both data sets simultaneously, a satisfactory consensus of the model parameters is not found. The fit is characterised by a sub-optimal RMSE of 0.277, with neither of the germination trends reproduced accurately (Figure B.1c).

The $(I \rightarrow T)C \wedge I$ model approximates the data with density-driven inhibition with slightly lower success than the previous model (RMSE of 0.0598, Figure B.2), but excels at matching the exogenously inhibited germination data (RMSE of 0.0224, Figure B.2b). In the simultaneous fitting procedure, the model only manages to approximate the density-dependent data, but fails to do so for the germination inhibited by exogenous 1-octen-3-ol (Figure B.2c), where germination is enabled only at low inhibitor concentration.

In the case of $(I \rightarrow T+S)C \wedge I$ (Figure B.3), the density-dependent fit is intermediate to the previous two models and the fit to the exogenously inhibited germination data is slightly worse (Figure B.3b). Like the $(I \rightarrow T)C \wedge I$, it finds an unsatisfactory solution in the simultaneous fitting to both data sets.

In summary, the parameter estimation procedure on *A. nidulans* data reveals that there are parameter configurations for which the three selected models can explain either the effects of density on germination or the effects of externally added 1-octen-3-ol on germination. But there is no parameter configuration for which the two effects may be assumed to originate from the same modelled phenomenon. This becomes even more evident when comparing the fitted parameters, presented in Appendix A: [Estimated Parameters](#), Tables A.3, A.4 and A.5.

Chapter 5

Discussion

5.1 Natural scenario

This thesis began by envisioning a hypothetical situation of a spore culture inoculating an aqueous medium. To relate this to the presented experiments and data, one can roughly estimate the spore densities that typically occur in nature. A single conidiophore may produce more than 10^4 conidia [14], amounting to about a billion conidia per mould colony [4]. Research has shown that the two most successful vectors of spore dispersal are hydrophobic surfaces and water drops [14]. Therefore, two respective dispersal situations can be thought of. If spores attach to the hydrophobic legs of an insect and are then discarded on the surface of a plant, a dew drop (presumably of $50\text{ }\mu\text{L}$) may form directly around them, entrapping them in water, where the examined diffusion processes may take place. On average, 3.4×10^4 spores out of 10^7 are picked up by hydrophobic surfaces [14]. Thus, in the extreme case when the entire spore mass of a colony is transferred, the drop would have 6.8×10^6 spores/mL. Alternatively, a rain drop may dislodge some spores from the colony — this is proven possible at a rate of 4.1×10^2 spores per 10^7 spores on average [14]. Referring to the same water volume, a settled drop would contain a maximum of 8.2×10^4 spores/mL. Thus, the first case should exhibit some degree of germination inhibition, while the second case would have a sparse inoculum where almost every spore can germinate. The higher spore densities observed in the studies (up to 10^8 spores/mL) are more relevant for artificial cultivations, such as stirred bioreactors.

5.2 Model characteristics

The models presented in this thesis primarily focus on the representation of inhibitor release by the spore, since its interaction with the number density of the spore culture is

considered less trivial than the entry of carbon sources into the cell wall. The reasoning behind this is that a high density of spores increases the ambient inhibitor concentration from zero to a relatively significant number (up to a μM [5]), while the external carbon source concentration pressure, usually in the mM order in laboratory experiments [2, 4], is likely not reduced much by its permeation into the cell walls of a dense spore culture.

It is important to note the many-spore simulation setups assume that the medium populated with spores spans infinitely in each dimension. In laboratory experiments, however, spores tend to gradually sink to the bottom of the medium [4], meaning that the density distribution changes over time and that a solid boundary (e.g. the bottom of a cultivation well) imposes a limit along the vertical dimension. These effects are considered too complex to be modelled in the current research.

The models demonstrate a different utility in addressing the research questions. The volume-based analytical model is highlighted as a good compromise between a simple formulation and descriptive capabilities. One could question the validity of the assumption of a designated volume per spore, particularly in the case of non-homogeneously distributed spores. In practice, the spore per volume is not necessarily to be understood as a geometric construct with spatially defined boundaries, but rather as a more abstract compartmentalisation of the spatial continuum. On the other hand, the idealisation of spore cultures as evenly spaced grids is a representation of average spore densities and is not dissimilar from coarse-graining and mean-field theory approaches used in statistical physics with satisfactory accuracy [109]. Nonetheless, if there is a non-linear interaction between the inhibitors released from different spores, less trivial than the co-occupation of space, the volume-based assumptions would lose its validity.

The numerical models act as support in the construction of the volume-based model but also come with their own unique functionality. For instance, the low-resolution numerical model serves as prototypical inspiration for the volume-based analytical model by compartmentalising space into “average-concentration” volumes, some of which can be designated to spores. The medium-resolution model proves useful in its representation of a wide range of spore densities, while still being relatively simple in its setup. It also appears to be the only numerical model capable of reproducing the concentration saturation of the volume-based model. There is a notable discrepancy from the analytical model in the saturation levels, possibly due to how concentration values are transferred from one lattice node to another. In the discrete scheme, molecules effectively traverse one lattice node per time step, whereas the fast diffusion constant in the medium generally implies a much larger diffusion radius for this time interval.

Where the medium-resolution model reaches its limit — at the detailed representation of spore geometries and their packing arrangements — the high-resolution model yields

great benefits. One of the valuable insights from it is that the spatial distribution of inhibitor in the spore and the spatial accessibility of spore regions greatly influence the rate of depletion. The homogeneous concentration distribution, also assumed by the other models, is too simplistic to paint an accurate picture. An accumulation in the inner cell wall is possible due to the adsorptive capacity of the polysaccharide matrix and the low permeability of the hydrophobin-melanin layer, but there does not seem to be a conclusive evidence of where the location of 1-octen-3-ol synthesis takes place. Furthermore, the internal diffusion constant D_B (Equation 3.43) is arbitrarily extrapolated from the external and interfacial diffusion constants, while it may in practice be subject to a different spatial differentiation. Once a more complete set of information can be compiled for this system, the high-resolution model can be set up with more accurate initial inhibitor distribution and diffusivity-based compartmentalisation of the spore.

5.3 Inhibition timing

An important finding from the examination of inhibitor release is that the depletion under known permeation constraints, even when decelerated by known adsorption kinetics, is much faster than the standard timing of germination. There could be several reasons for this. First, there may exist a considerable lag between the depletion of the inhibitor and the onset of conidial swelling, with slow metabolic processes taking place in the meantime. A second culprit could be the assumption of a non-renewable inhibitor in the spore — if 1-octen-3-ol is continuously synthesised in the dormant spore, then its release would be balanced with an internal concentration increase, leading to a much later depletion. Finally, the permeability and adsorption values used in the computations are a collection of rough estimates, mostly based on molecular analogues measured at various experimental settings, possibly underestimating the compactness of the cell wall matrix and the interactions with it.

As Figure 4.5 illustrates, the volume-based model is characterised by two regimes of concentration decrease: an exponential one at early times and a saturating one at late times. This can also be inferred from analysing Equation 3.64: as $t \rightarrow \infty$, the exponential term vanishes and the concentration is mostly left with a constant defined by ϕc_0 . The early linear regime is also modulated by the volume fraction ϕ , as exhibited by the term $\exp(-\frac{t}{\tau(1-\phi)})$, which means that a high density of spores would immediately decelerate the release of inhibitor.

The idea that inhibition is based on time-dependent diffusion highlights a new possibility to view the process of externally controlled inhibition. While previous experiments [2, 5] may reinforce the thought that newly introduced 1-octen-3-ol to a spore culture is

something that “adds” inhibition to their germination, this misses the more nuanced notion that the external 1-octen-3-ol concentration decreases and possibly reverses the release-driving gradient.

5.4 Effect of spore clusters

The results from the high-resolution simulations of spore clusters challenge the hypothesis that densely packed spores create a porous medium with limited diffusivity. While the surrounding of a spore with neighbours does slightly reduce the release of inhibitor, the area of contact is too small to reduce the outward flux significantly, and the diffusion through the intermediate spaces is still fast enough to “flush” the inhibitor away. On the other hand, the simulations may fail to represent some important characteristics of spore agglomerations. First, the cell wall interactions that enable adhesion may increase the contact area beyond a mere point of touch. Second, the simulations only consider a single degree of neighbourhood in the 13-spore cluster, whereas actual spore agglomerations may have multiple layers of surrounding spores, which likely amplifies the diffusion-limiting effect. The sizes of spore clusters, however, do not appear large enough to make the volume-based model applicable to intra-cluster diffusion [15, 24].

A further bias on the results may be from the implementation of an absorbing boundary condition, which guarantees that all inhibitor exiting the cluster is removed from the system. This measure is imposed due to the inability to compute large lattice sizes, where the external inhibitor can settle over a more extensive volume. Forcing the gradient at the boundaries, the absorbing boundary may also pull concentration values more rapidly out of the cluster, compared to a large system with a periodic boundary. Additionally, ambient concentrations close to the cluster may be more readily rounded to zero due to the limited precision of 32-bit floating-point numbers in the implicit solver implementation. Hence, if the computational obstacles of the high-resolution model are overcome, diffusion within and between spore clusters can be more accurately represented.

Due to its apparent insignificance and the difficulty of extracting a mathematical law from the numerical experiments, the cluster effect on the release rate is not integrated in the analytical model. Nonetheless, it remains to be tested whether more advanced numerical experiments could provide contrary evidence.

5.5 Germination models

The parameter estimation process highlights three candidates as having the best performance: the $(I \rightarrow T)C \wedge I$, $(I \rightarrow S)C \wedge I$ and $(I \rightarrow T+S)C \wedge I$ models. It is important to consider the conditions and implications for this result, and to attempt to relate it back to biologically sensible scenarios.

In the early stage of the parameter estimation, several consecutive runs were performed on each model, ensuring that the number of optimisation steps were sufficient for convergence. Nonetheless, the existence of tightly localised error minima, missed by the optimisation, cannot be ruled out. Larger-scale experiments with a greater population size in the DE algorithm could be performed to verify this. Furthermore, the Gauss-Hermite approximation of multi-dimensional integrals does not go without a loss of accuracy. Among some of the results, it has been noticed that a low number of nodes lead to a slight distortion of the germination curves, which in turn could bias the optimisation.

The general approach followed in the search of an appropriate germination model is to first test basic variants, then possible combinations of more successful candidates, then introduce variability in parameters which are causing rigidity in specific model features. The conceptual diagrams of the model variants are shown in Figure 5.1, together with their enhancement steps. As the complexity of the models increases, it appears logical that the additional degrees of freedom of the model (the number of parameters) generally reduce the RMSE. Sometimes, however, parameters shared between multiple model components constrain the optimisation process, despite the model being more complex. For example, in the basic case of an inhibitor-dependent induction, an effect on only one of the target components, threshold or signal, exhibits a better fit than a simultaneous effect on both components. This is not the case in their combined counterparts.

If the performance of a model is seen as indicative of the likelihood of the corresponding mechanism to occur in nature, then the results from the parameter estimation could be used to support or rule out natural scenarios. While relatively simple as an assumption, a germination triggered by non-interacting induction and inhibition seems plausible, especially if the heterogeneity of elements like the cell wall contributes to a wider distribution of germination times. A scenario is conceivable in which the inducer triggers a cell-wall restructuring that accelerates inhibitor release, but that would also imply that the permeation of the inducer itself would be modulated over time — a feedback loop which is not incorporated in the $(C \rightarrow P)I$ model. The scenario in which a similar process shifts the inhibition threshold is not impossible, but prioritising inhibitor depletion before induction in germination triggering goes against most intuition and scientific evidence: the pathways of nutrient signalling have been examined well enough define it as

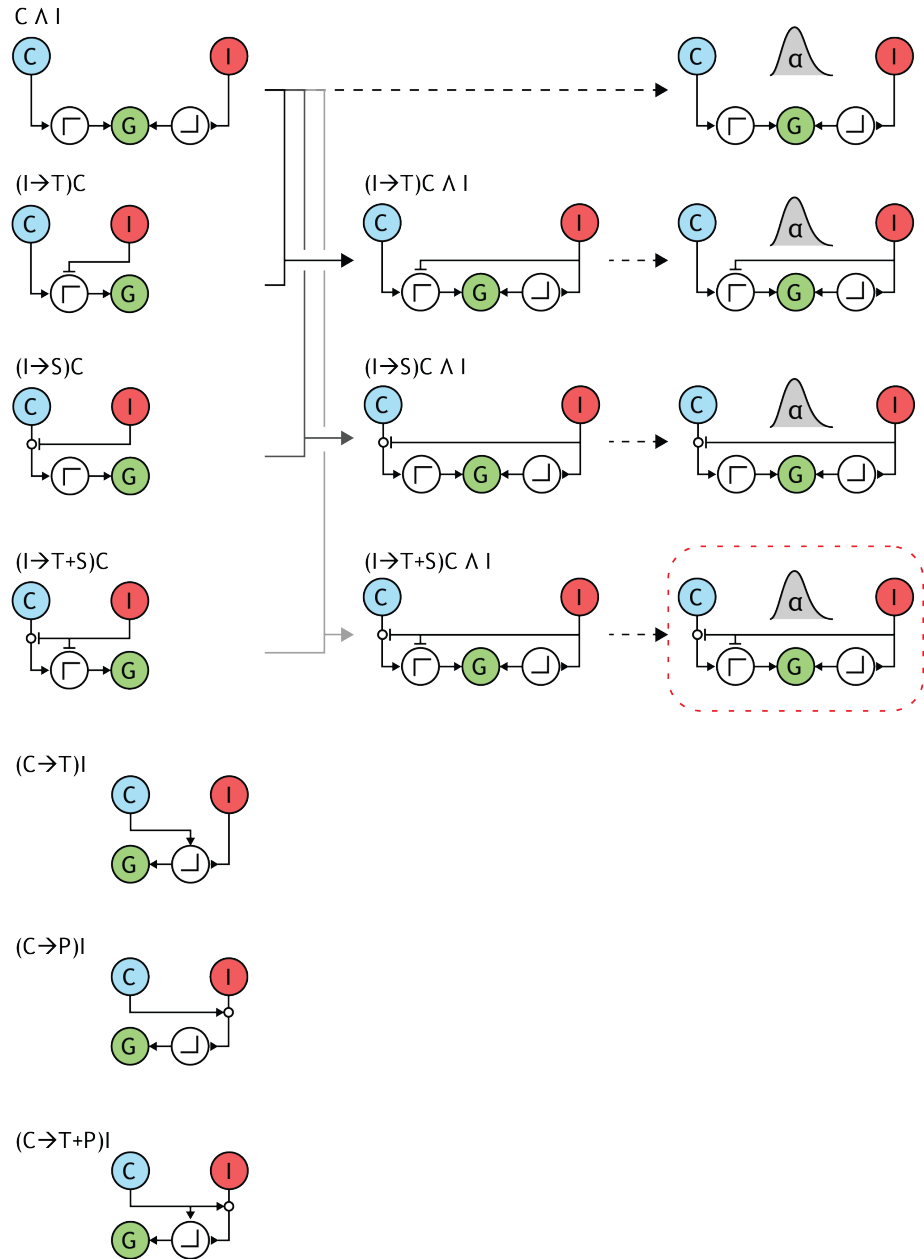


FIGURE 5.1: Diagrammatic illustration of the basic germination models (left column) and their enhancement through combinations (central column) and through the addition of varying cell wall permeability (right column). G indicates the germination event, C denotes the carbon source (inducer) and I denotes the inhibitor. The thresholds for the two germination factors are indicated by the Γ -like symbols. The dashed red line indicates the best performing model.

directly germination-defining. Therefore, it is reassuring that the $(C \rightarrow T)I$, $(C \rightarrow P)I$, $(C \rightarrow T+P)I$ models do not exhibit a good fit. The superior results from the combined models suggest that the role of the inhibitor could be twofold. On one hand, its depletion could activate a germination-associated metabolic cascade which is not dependent on the cAMP-PKA pathway. On the other hand, a branch of this cascade could affect the inducing signal — by either creating more favourable conditions for its transmission or by lowering the barrier for its triggering effect.

An important finding from the *A. nidulans* data fitting process is that the incorporation of exogenous 1-octen-3-ol in the germination model is inconsistent with the effect of dense spore cultures, if they would also be releasing the same inhibitor. In $(I \rightarrow T)C \wedge I$ and $(I \rightarrow T+S)C \wedge I$, if germination decreases for high doses of exogenous 1-octen-3-ol, then the mechanism of germination is not sensitive to density (Figures B.1c and B.3c). In $(I \rightarrow S)C \wedge I$, if germination is appropriately affected by conidial density, then even the slightest dose of 1-octen-3-ol eliminates germination (Figure B.2c). Naturally, this could be an indication that the model is missing an important component which could bind the two phenomena. Alternatively, this could point to a rejection of the hypothesis that 1-octen-3-ol is the naturally-occurring dominant inhibitor of germination in *A. nidulans* — an issue already questioned in the case of *A. flavus* [5]. This is consistent with the observation that experimentally tested external 1-octen-3-ol concentrations needed to inhibit germination are much larger than what is producible by the spore. Instead, inhibition could arise from a more complex concerted interaction between different VOCs, proteins and other secreted molecules, so merely adding 1-octen-3-ol to the culture does not necessarily reproduce the same in-vivo inhibition dynamics.

5.6 Interpretation of estimated parameters

A look into the estimated parameters can provide additional validation of the models, but can also challenge some assumptions made in the earlier experiments. In all time-dependent model fits, the inhibitor permeation constant P_s^{inh} is in the order of $10^{-8} \text{ cm s}^{-1}$, a range consistent with most depletion scenarios summarized in Table 4.1. The estimated carbon-source permeability, P_s^{cs} , is in most cases at least an order higher. Table A.1 shows one abnormal case in which the permeabilities of alanine and proline are radically different: the $(I \rightarrow S)C \wedge I$ model. The two amino acids differ slightly in their molecular size and partition coefficient, but not as much to explain such a discrepancy. This diminishes the validity of the model with an inhibitor-dependent induction signal.

The observation that $P_s^{\text{cs}} > P_s^{\text{inh}}$ appears counter-intuitive given the previous analysis of the hydrophobin layer permeability. While being slightly less hydrophilic can glucose,

alanine and proline have a partition coefficient much lower than that of 1-octen-3-ol, suggesting that their passage through the rodlet layer should be much more restricted. This could imply that the conidial hydrophobin-melanin cover is much more permeable to inducer molecules than in-vitro assembled hydrophobin bilayers. Furthermore, it could indicate that the diffusion-limiting role of adsorption is much stronger than the rodlet barrier, since it mostly affects the outflux of VOCs but not the incoming carbon sources.

The inducer half-saturation constants K_{cs} remain in the same order for alanine and proline, suggesting that receptors of the same type or with a similar frequency of distribution may be responsible for receiving the inducing signal. This may lead one to expect that the inhibition constants K_I should also be similar for the two amino acids, which is only the case for the combined models with variable cell wall porosity, as Table A.2 suggests. The same models also leads to more similar Hill coefficients, confirming that the inhibitory dynamics on the two inducing pathways are similar, regardless of the inducer type. However, it appears that the factor k by which the inhibitor shifts the threshold of induction is most homogeneous in the $(I \rightarrow T+S)C \wedge I$ model, both with and without variable cell wall permeability. If the induction pathways of alanine and proline are similar, one would not expect the inhibition of these to differ. This forms a case against the $(I \rightarrow T)C \wedge I$ model, where the two k values are markedly dissimilar.

The random variable parameters appear to have sensible values. The mean threshold of inhibition μ_γ is in the order of 10^{-5} , i.e. a significant reduction from the initial concentration. The cell wall porosity remains in the order of 10^{-1} , consistent with the inference of free volume in the cell wall matrix [120]. The mean initial concentration μ_ψ , however, is in the order of 0.1 M for all experiments, much higher than the estimate inferred from literature [5]. Nonetheless, preliminary calculations have shown that it is physically possible to accommodate the respective amount of molecules in a spore. As the high-resolution simulations demonstrated, the driving concentration could simply be increased due to narrow localisation. If also continuous inhibitor synthesis is also accounted for, then the value begins to make more sense.

Based on these observations, the $(I \rightarrow T+S)C \wedge I$ model exhibits the most realistic parameter values with respect to the *A. niger* data set. When the *A. nidulans* set is estimated on, Table A.3 shows that n , the γ , ω and ψ distributions remain mostly consistent for this model, but the constants K_{cs} and K_I differ. This could be explainable by physiological differences between the two fungal species. Most notably, the impact of the inhibitor on the induction threshold has a radically different scale factor k in the case of the *A. nidulans* set. Since *A. nidulans* has significantly different germination patterns compared to *A. niger* [3], the disparity in this parameter could be due species-specific evolutionary adaptations.

Chapter 6

Conclusion and Future Work

This thesis embarked on a search for a mathematical model of diffusive signalling in *Aspergillus* spore colonies. With regard to germination induction, it was shown that the entry of carbon source molecules into the cell wall may be limited by the barrier permeability. Regarding germination inhibition, calculations showed that passive diffusion must be substantially obstructed, or countered by continuous inhibitor synthesis, for the inhibitor to be depleted on the time scale of germination. A mathematical framework was proposed to capture known inhibitory effects of conidial density on inhibition and, in combination with a model of heterogeneity, managed to reproduce recorded germination data with relatively high accuracy. However, the results pointed against 1-octen-3-ol being a sole primary inhibitor of germination in *A. nidulans*. The most valid model of the germination mechanism was found to include two triggering criteria, one based on the depletion of inhibitor and another based on an inducing signal whose threshold and strength are influenced by the inhibitor.

As a by-product of this research, multiple numerical models were developed that could find application in more complex diffusion simulations, not only in the context of spores, but also in any setup which involves slowly releasing spores in a fast diffusing medium. The low-resolution model could be used as a computationally efficient tool in rough approximations of molecular transport on scales much larger than the size of the sources. Given the close alignment of the medium-resolution model with the volume-based analytical model, it could be used to explore the effects of irregularly distributed spores and validate the homogeneous grid approximation. The high-resolution model offers interesting opportunities for the detailed exploration of interfacial diffusivities in geometrically complex configurations. A necessary requirement for this is to construct a more exhaustive model of the cell wall layers with their respective permeabilities, and a better informed distribution of the diffusing species within the spore volume. While not

implemented in the current studies, the diffusion of nutrients (i.e. inducing molecules) within spore clusters could also be integrated in this framework, observing how an incoming front of carbon source molecules reaches the interior of a spore aggregate, similar to other studies with modelled hyphal networks [94].

To address questions below the scale of the high-resolution model, and to inform its parameters with rigorously determined statistical measurements, molecular dynamics (MD) simulations could prove to be instrumental. This is especially valid for the case of the complex cell wall structure, where layers do not have strict boundaries but rather interlink into an intricate network, with different molecules serving as specialised building blocks. MD has been applied to similar contexts [43, 128] and is becoming increasingly available to researchers [129]. Thus, by performing large-scale simulations of molecular trajectories through an assembled cell wall complex, the permeation constants could be defined more concretely, ideally under consideration of the polysaccharide interactions with the passing molecules.

The results from the current research motivate targeted investigations on some subsequent questions: Is there a lag between inhibitor depletion and, if not, why is the inhibitor release seemingly so slow? How do multiple species of inhibitor coordinate during their release from the spore? Addressing these questions involves the exploration of model extensions, e.g. by introducing inhibitor renewal in the spore, incorporating lag time as a variable, looking into potential feedback mechanisms and involving more complex systems of ODEs in the determination of germination probability.

If these extensions demonstrate a tighter alignment between model and data, they could be instrumental to answering more advanced questions: How do inter- and intra- species inhibition interact in mixed spore cultures [1]? What is the effect of exogenously adding of a mixture of inhibitors to a spore culture? The answers bear relevance to a wide range of applications, from optimising industrial biosynthesis of useful substances and building materials to antagonistic biocontrol of harmful fungi through competition with benign ones. When coupled with established hyphal growth models and the ever-expanding scope of metabolic and gene regulatory network models, the model of diffusive signalling could become a defining component in the construction of a digital twin of the fungal life cycle. Endeavours like this could not only have practical benefits, but also encourage interdisciplinary collaboration in harnessing computing technology for the better understanding of fungi and their ecosystems.

Chapter 7

Ethics and Data Management

I hereby acknowledge that the present thesis meets the standards of the ethical code (<https://ivi.uva.nl/research/ethical-code/ethical-code.html>) and research data management policies (<https://rdm.uva.nl/en>) of UvA and Ivi. Additionally, my reflection on the ethical aspects of the current project concerns three topics: the societal impact of the field of research, the responsible and commensurate use of computation and the ethics of Artificial Intelligence for the acquisition of information for the thesis.

The use of *Aspergillus* moulds and other filamentous fungi for biosynthesis and biosorption can be seen as a promising component for a circular economy, harnessing the capabilities of available biological systems to improve human wellbeing. To reinforce such techniques in a sustainable way, society needs to develop a deep understanding of the ecological factors surrounding the fungi and an awareness of potential risks, especially when pathogenicity is involved. Computational Science provides tools to analyse the vast complexity of natural systems and to assemble interdisciplinary knowledge for addressing relevant research questions.

It is important to maintain an awareness of the energetic costs related to computation in such cases — while powerful complex models can yield unprecedented insight, often a simplification of these can provide sufficiently valuable results. Therefore, the trajectory followed in this thesis was to maintain a limit of complexity that permits the execution of experiments on a desktop computer architecture, and use more elaborate models as a stepping stone for arriving at simpler computational solutions.

Large Language Models (LLMs) have been used to reflect on, inspire, verify and compute many aspects in this thesis. I acknowledge the usefulness of such tools but recognise the risks associated with them — the inherent bias, the energy consumption and the potentially unauthorised use of intellectual property in training sets. For this reason, I

have strived to maintain a critical view of the input obtained with them, and have always prioritised references to scientific resources whenever available and applicable.

The following table lists the data used in this thesis (including source codes). I confirm that the list is complete and the listed data are sufficient to reproduce the results of the thesis. If a prohibitive non-disclosure agreement is in effect at the time of submission "NDA" is written under "Availability" and "License" for the concerned data items.

Short description (max. 10 words)	Availability (e.g., URL, DOI)	License (e.g., MIT, GPL, Creative Commons)
Example dataset 1	<github url> or Figshare	GPL
Example source code	DOI (from Zenodo)	MIT
Example sensitive data	NDA	NDA

Appendix A

Estimated Parameters

Parameter	Model: $(I \rightarrow T)C \wedge I$	Model: $(I \rightarrow S)C \wedge I$	Model: $(I \rightarrow T+S)C \wedge I$	Units
P_s^{inh}	4.2319×10^{-4}	6.3956×10^{-4}	5.1449×10^{-4}	$\mu\text{m s}^{-1}$
P_s^{cs}	$9.4855 \times 10^{-3} *$ $9.6350 \times 10^{-4} **$	$1.9595 \times 10^{-6} *$ $5.6809 \times 10^{-3} **$	$8.9918 \times 10^{-3} *$ $4.6816 \times 10^{-3} **$	$\mu\text{m s}^{-1}$
k	$2.0789 \times 10^1 *$ $5.4641 \times 10^{-1} **$		$3.4688 \times 10^2 *$ $1.9828 \times 10^2 **$	—
K_I		$1.9383 \times 10^{-2} *$ $6.0568 \times 10^{-1} **$	$2.3363 \times 10^{-3} *$ $6.6210 \times 10^{-1} **$	M
K_{cs}	$6.7247 *$ $7.6924 **$	$1.4729 \times 10^{-2} *$ $3.2188 \times 10^{-2} **$	$8.2306 \times 10^{-2} *$ $4.1054 \times 10^{-2} **$	M
n		$1.2950 *$ $2.6325 **$	$2.7575 *$ $1.0069 **$	—
μ_γ	7.8219×10^{-2}	3.7564×10^{-5}	4.9369×10^{-5}	—
σ_γ	4.3042×10^{-6}	2.0720×10^{-5}	2.9083×10^{-5}	—
μ_ω	$8.3023 \times 10^{-4} *$ $7.9775 \times 10^{-4} **$	$2.9838 \times 10^{-1} *$ $6.0636 \times 10^{-2} **$	$9.6089 \times 10^{-2} *$ $3.8092 \times 10^{-2} **$	—
σ_ω	$4.4878 \times 10^{-4} *$ $4.0620 \times 10^{-4} **$	$5.9110 \times 10^{-2} *$ $2.7591 \times 10^{-6} **$	$6.9761 \times 10^{-3} *$ $1.6345 \times 10^{-3} **$	—
μ_ψ	9.8732×10^{-1}	9.8460×10^{-1}	8.5417×10^{-1}	M
σ_ψ	2.0058×10^{-4}	7.9399×10^{-1}	1.4533×10^{-2}	M

TABLE A.1: Parameters for the $(I \rightarrow T)C \wedge I$, $(I \rightarrow S)C \wedge I$ and $(I \rightarrow T+S)C \wedge I$ models, fitted on *A. niger* data by Ijadpanahsaravi et al. [1]; *: alanine, **: proline.

Parameter	Model: $C \wedge I$	Model: $(I \rightarrow T)C \wedge I$	Model: $(I \rightarrow S)C \wedge I$	Model: $(I \rightarrow T+S)C \wedge I$	Units
P_s^{inh}	6.3713×10^{-4}	7.4559×10^{-4}	8.1118×10^{-4}	8.1371×10^{-4}	$\mu\text{m s}^{-1}$
P_s^{cs}	$2.2234 \times 10^{-3} *$ $8.8045 \times 10^{-3} **$	$9.1422 \times 10^{-3} *$ $7.5977 \times 10^{-3} **$	$1.8394 \times 10^{-6} *$ $6.2726 \times 10^{-3} **$	$5.4319 \times 10^{-3} *$ $6.3523 \times 10^{-4} **$	$\mu\text{m s}^{-1}$
k		$4.0108 \times 10^2 *$ $6.2367 \times 10^1 **$		$4.0027 \times 10^2 *$ $1.1725 \times 10^2 **$	—
K_I			$4.2889 \times 10^{-1} *$ $7.4325 \times 10^{-1} **$	$5.7296 \times 10^{-1} *$ $3.0237 \times 10^{-1} **$	M
K_{cs}	$8.9137 \times 10^{-2} *$ $2.4530 \times 10^{-4} **$	$8.9036 \times 10^{-2} *$ $5.7986 \times 10^{-2} **$	$1.4112 \times 10^{-2} *$ $3.6660 \times 10^{-2} **$	$1.2957 \times 10^{-2} *$ $2.7037 \times 10^{-2} **$	M
n			$1.4793 *$ $1.8462 **$	$2.7786 *$ $2.1021 **$	—
μ_γ	3.7113×10^{-5}	4.5787×10^{-5}	3.7064×10^{-5}	4.4994×10^{-5}	—
σ_γ	1.7445×10^{-5}	2.7178×10^{-5}	1.8616×10^{-5}	2.4422×10^{-5}	—
μ_ω	$6.4159 \times 10^{-2} *$ $6.8579 \times 10^{-2} **$	$9.6341 \times 10^{-2} *$ $1.4110 \times 10^{-1} **$	$2.4015 \times 10^{-1} *$ $2.6748 \times 10^{-2} **$	$4.2022 \times 10^{-1} *$ $7.3414 \times 10^{-2} **$	—
σ_ω	$2.7081 \times 10^{-2} *$ $1.0373 \times 10^{-5} **$	$2.3388 \times 10^{-3} *$ $6.3534 \times 10^{-5} **$	$9.5741 \times 10^{-2} *$ $6.2965 \times 10^{-6} **$	$7.3403 \times 10^{-3} *$ $3.6295 \times 10^{-6} **$	—
μ_ψ		2.4229×10^{-1}	7.1718×10^{-1}	9.9262×10^{-1}	M
σ_ψ		1.6158×10^{-1}	1.5635×10^{-1}	8.0986×10^{-1}	M
μ_α	9.6290×10^{-1}	8.1394×10^{-1}	8.3779×10^{-1}	7.5311×10^{-1}	—
σ_α	5.4609×10^{-1}	4.2488×10^{-1}	3.7772×10^{-1}	3.8193×10^{-1}	—

TABLE A.2: Parameters for the $C \wedge I$, $(I \rightarrow T)C \wedge I$, $(I \rightarrow S)C \wedge I$ and $(I \rightarrow T+S)C \wedge I$ models with varying permeability, fitted on *A. niger* data by Ijadpanahsaravi et al. [1]; *: alanine, **: proline.

Parameter	Model: $(I \rightarrow T)C \wedge I$	Model: $(I \rightarrow S)C \wedge I$	Model: $(I \rightarrow T+S)C \wedge I$	Units
k	3.3799×10^{-1}		3.4594×10^{-3}	—
K_I		6.1060×10^{-1}	1.4881×10^{-3}	M
K_{cs}	1.7922×10^{-2}	4.9540×10^{-3}	5.1903×10^{-3}	M
n		2.6211	2.3103	—
μ_γ	4.3473×10^{-5}	4.4199×10^{-5}	4.4085×10^{-5}	—
σ_γ	4.1900×10^{-5}	4.0926×10^{-5}	4.1010×10^{-5}	—
μ_ω	8.2103×10^{-2}	1.3430×10^{-1}	2.3719×10^{-1}	—
σ_ω	3.4592×10^{-4}	3.9778×10^{-3}	1.5583×10^{-4}	—
μ_ψ	2.1604×10^{-2}	4.0387×10^{-1}	6.8414×10^{-1}	M
σ_ψ	1.6178×10^{-3}	3.8206×10^{-2}	5.1230×10^{-2}	M

TABLE A.3: Parameters for the $(I \rightarrow T)C \wedge I$, $(I \rightarrow S)C \wedge I$ and $(I \rightarrow T+S)C \wedge I$ models, fitted on *A. nidulans* germination data with density-driven inhibition by Herrero-Garcia et al. [2].

Parameter	Model: $(I \rightarrow T)C \wedge I$	Model: $(I \rightarrow S)C \wedge I$	Model: $(I \rightarrow T+S)C \wedge I$	Units
k	6.5464		1.4193	—
K_I		2.5442×10^{-2}	4.0465×10^{-3}	M
K_{cs}	1.6453×10^{-1}	3.1629×10^{-2}	3.1633×10^{-1}	M
n		2.6202	1.6949	—
μ_γ	3.3645×10^{-3}	4.0334×10^{-2}	7.8096×10^{-2}	—
σ_γ	1.2239×10^{-4}	5.1119×10^{-6}	7.3351×10^{-6}	—
μ_ω	8.9933×10^{-4}	6.2136×10^{-2}	4.3528×10^{-4}	—
σ_ω	8.8132×10^{-4}	6.0672×10^{-2}	4.0460×10^{-4}	—
μ_ψ	7.2531×10^{-1}	6.3118×10^{-2}	3.1029×10^{-2}	M
σ_ψ	4.9611×10^{-1}	3.5123×10^{-2}	2.1055×10^{-2}	M

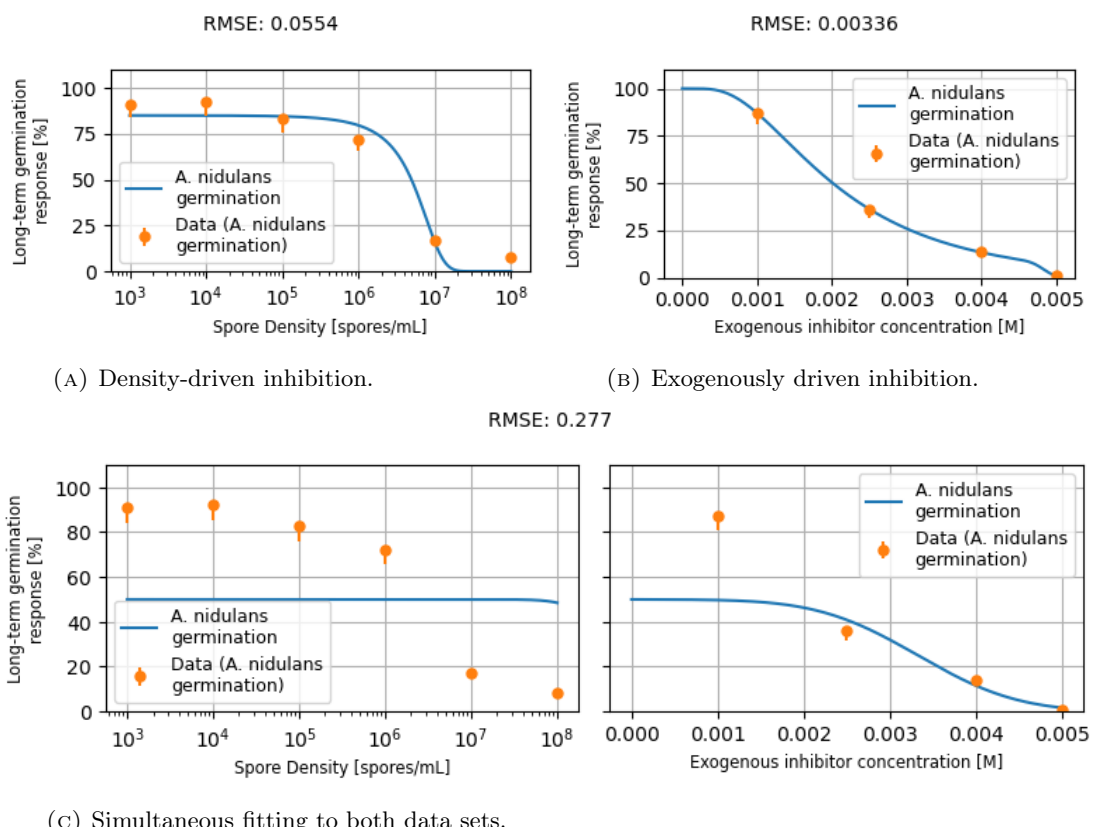
TABLE A.4: Parameters for the $(I \rightarrow T)C \wedge I$, $(I \rightarrow S)C \wedge I$ and $(I \rightarrow T+S)C \wedge I$ models, fitted on *A. nidulans* data of exogenously inhibited germination by Herrero-Garcia et al. [2].

Parameter	Model: $(I \rightarrow T)C \wedge I$	Model: $(I \rightarrow S)C \wedge I$	Model: $(I \rightarrow T+S)C \wedge I$	Units
k	5.3782×10^1		1.0271×10^2	—
K_I		6.7008×10^{-1}	7.5659×10^{-1}	M
K_{cs}	1.7158×10^{-2}	1.4236×10^{-2}	5.1402×10^{-3}	M
n		2.1419	2.9162	—
μ_γ	9.9987×10^{-5}	4.4698×10^{-5}	9.9000×10^{-5}	—
σ_γ	2.2018	4.1589×10^{-5}	2.1585	—
μ_ω	6.5397×10^{-2}	2.6618×10^{-2}	1.7711×10^{-1}	—
σ_ω	4.9089×10^{-2}	3.5245×10^{-3}	9.3748×10^{-2}	—
μ_ψ	9.9428×10^{-1}	9.9999×10^{-1}	9.9792×10^{-1}	M
σ_ψ	8.9050×10^{-1}	9.7285×10^{-1}	8.5642×10^{-1}	M

TABLE A.5: Parameters for the $(I \rightarrow T)C \wedge I$, $(I \rightarrow S)C \wedge I$ and $(I \rightarrow T+S)C \wedge I$ models, fitted on *A. nidulans* data with both density-driven and exogenously driven inhibition by Herrero-Garcia et al. [2].

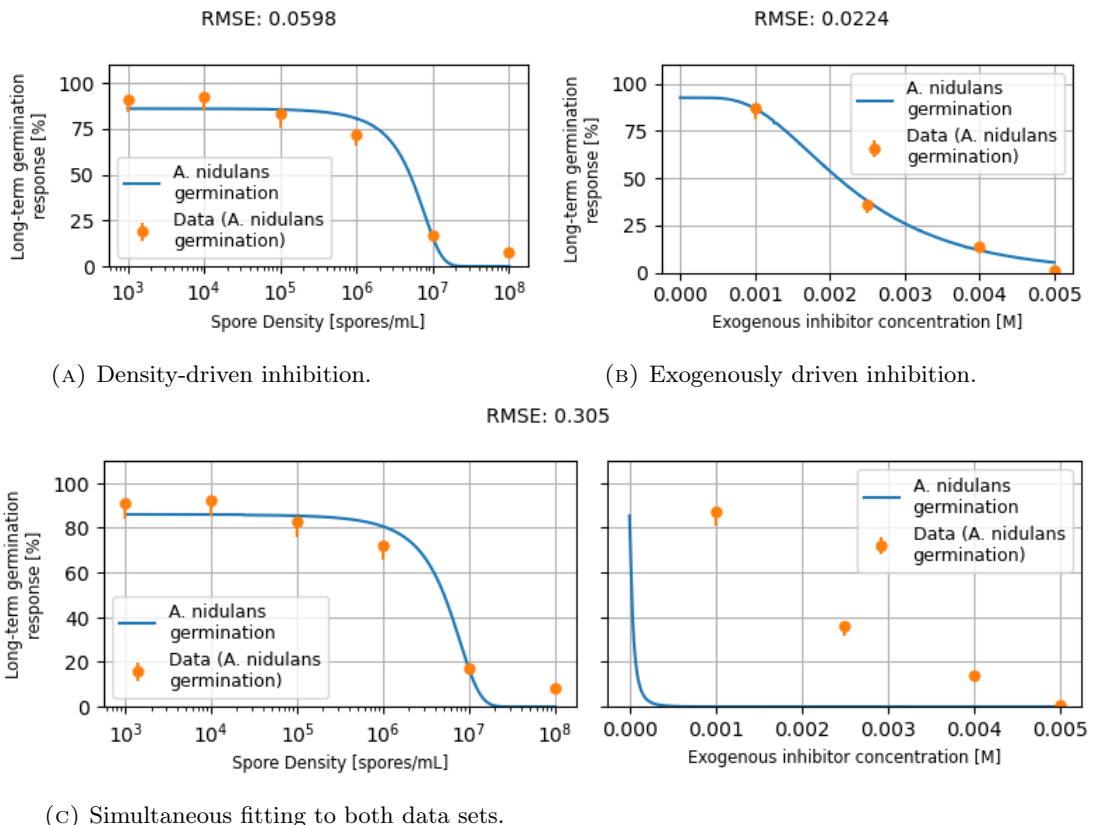
Appendix B

Fitting Models To *A. nidulans* Data



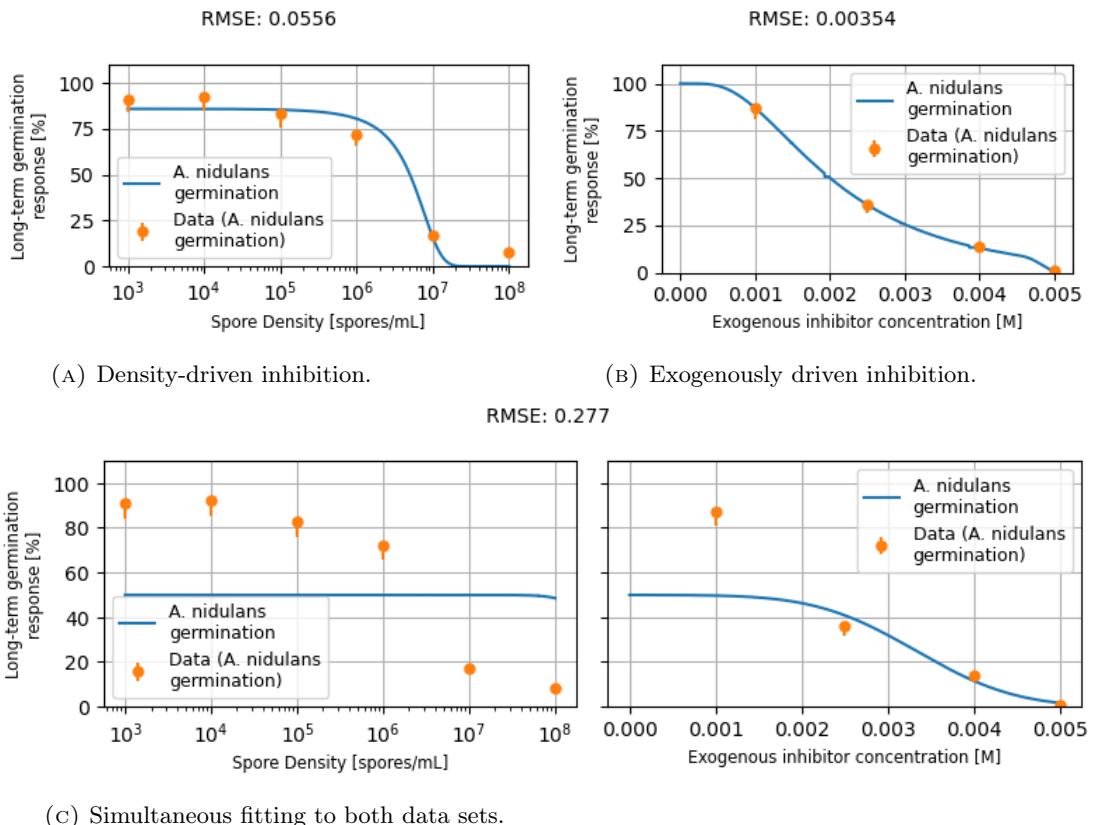
(c) Simultaneous fitting to both data sets.

FIGURE B.1: *A. nidulans* germination data vs. germination probabilities predicted by the $(I \rightarrow T)C \wedge I$ model.



(c) Simultaneous fitting to both data sets.

FIGURE B.2: *A. nidulans* germination data vs. germination probabilities predicted by the $(I \rightarrow S)C \wedge I$ model.



(c) Simultaneous fitting to both data sets.

FIGURE B.3: *A. nidulans* germination data vs. germination probabilities predicted by the $(I \rightarrow T+S)C \wedge I$ model.

Bibliography

- [1] Maryam Ijadpanahsaravi, L. Basten Snoek, Wieke R. Teertstra, and Han A. B. Wösten. The impact of inter- and intra-species spore density on germination of the food spoilage fungus *aspergillus niger*. *International journal of food microbiology*, 410:110495, 2023. URL <https://api.semanticscholar.org/CorpusID:265268197>.
- [2] Erika Herrero-García, Aitor Garzia, Shandra Cordobés, Eduardo Antonio Espeso, and Unai O. Ugalde. 8-carbon oxylipins inhibit germination and growth, and stimulate aerial conidiation in *aspergillus nidulans*. *Fungal biology*, 115 4-5:393–400, 2011. URL <https://api.semanticscholar.org/CorpusID:33687383>.
- [3] Maryam Ijadpanahsaravi, Wieke R. Teertstra, and Han A. B. Wösten. Inter- and intra-species heterogeneity in germination of *aspergillus conidia*. *Antonie Van Leeuwenhoek*, 115:1151 – 1164, 2022. URL <https://api.semanticscholar.org/CorpusID:250697351>.
- [4] Maryam Ijadpanahsaravi, Maarten Punt, Han A. B. Wösten, and Wieke R. Teertstra. Minimal nutrient requirements for induction of germination of *aspergillus niger* conidia. *Fungal biology*, 125 3:231–238, 2020. URL <https://api.semanticscholar.org/CorpusID:229474784>.
- [5] Kana Miyamoto, Tomoko Murakami, Pattana Kakumyan, Nancy P. Keller, and Kenji Matsui. Formation of 1-octen-3-ol from *aspergillus flavus* conidia is accelerated after disruption of cells independently of ppo oxygenases, and is not a main cause of inhibition of germination. *PeerJ*, 2, 2014. URL <https://api.semanticscholar.org/CorpusID:8514039>.
- [6] Gaëlle Lamon, Alons Lends, Isabel Valsecchi, Sarah Sze, Wah Wong, Vincent Dupres, Frank Lafont, James Tolchard, Christine Schmitt, Adeline Mallet, Axelle Grélard, Estelle Morvan, Erick J Dufourc, Birgit Habenstein, J. Iñaki Guijarro, Vishukumar Aimanianda, and Antoine Loquet. Solid-state nmr molecular snapshots of *aspergillus fumigatus* cell wall architecture during a conidial morphotype transition. *Proceedings of the National Academy of Sciences of the United States*

- of America, 120, 2023. URL <https://api.semanticscholar.org/CorpusID:256414380>.
- [7] Rocio Garcia-Rubio, Haroldo Cesar de Oliveira, Johanna Rivera, and Nuria Trevijano-Contador. The fungal cell wall: Candida, cryptococcus, and aspergillus species. *Frontiers in Microbiology*, 10, 2020. URL <https://api.semanticscholar.org/CorpusID:210072641>.
- [8] Naresh Magan and David Aldred. Post-harvest control strategies: minimizing mycotoxins in the food chain. *International journal of food microbiology*, 119 1-2: 131–9, 2007. URL <https://api.semanticscholar.org/CorpusID:5623278>.
- [9] Vera Meyer, Evelina Y. Basenko, Philipp Benz, Gerhard H. Braus, Mark X. Cadick, Michael Csukai, Ronald P. de Vries, Jens Christian Frisvad, Nina Gundl Cimerman, Thomas Haarmann, Robert I Johnson, Nancy P. Keller, Uffe Hasbro Mortensen, Rolando Perez, Arthur F. J. Ram, Phil Ross, Volha Shapaval, Charlotte Steiniger, Hans van den Brink, Jolanda M. van Munster, and Han A. B. Wösten. Growing a circular economy with fungal biotechnology: a white paper. *Fungal Biology and Biotechnology*, 7, 2020. URL <https://api.semanticscholar.org/CorpusID:215411291>.
- [10] Timothy C. Cairns, Corrado Nai, and Vera Meyer. How a fungus shapes biotechnology: 100 years of aspergillus niger research. *Fungal Biology and Biotechnology*, 5, 2018. URL <https://api.semanticscholar.org/CorpusID:44079887>.
- [11] Aïda M. Farag, Hanan M. Abd-Elnabey, Hassan A. H. Ibrahim, and M. El-shenawy. Purification, characterization and antimicrobial activity of chitinase from marine-derived aspergillus terreus. *The Egyptian Journal of Aquatic Research*, 42:185–192, 2016. URL <https://api.semanticscholar.org/CorpusID:89393495>.
- [12] Ken ichi Kusumoto, Youhei Yamagata, Rina Tazawa, Manabu Kitagawa, Taeko Kato, Kenji Isobe, and Yutaka Kashiwagi. Japanese traditional miso and koji making. *Journal of Fungi*, 7, 2021. URL <https://api.semanticscholar.org/CorpusID:236320190>.
- [13] Scott Baker and Joan W Bennett. An overview of the genus aspergillus. 2016. URL <https://api.semanticscholar.org/CorpusID:41156761>.
- [14] Wieke R. Teertstra, Martin Tegelaar, Jan Dijksterhuis, Elena A. Golovina, Robin A. Ohm, and Han A. B. Wösten. Maturation of conidia on conidiophores of aspergillus niger. *Fungal genetics and biology : FG & B*, 98:61–70, 2017. URL <https://api.semanticscholar.org/CorpusID:5170504>.

- [15] Henri Müller, Lars Barthel, Stefan Schmideder, Tabea Schütze, Vera Meyer, and Heiko Briesen. From spores to fungal pellets: A new high-throughput image analysis highlights the structural development of *aspergillus niger*. *Biotechnology and Bioengineering*, 119:2182 – 2195, 2022. URL <https://api.semanticscholar.org/CorpusID:248414482>.
- [16] Jae-Hyuk Yu. Regulation of development in *aspergillus nidulans* and *aspergillus fumigatus*. *Mycobiology*, 38:229 – 237, 2010. URL <https://api.semanticscholar.org/CorpusID:17713460>.
- [17] Alessandro Comarú Pasqualotto. Differences in pathogenicity and clinical syndromes due to *aspergillus fumigatus* and *aspergillus flavus*. *Medical mycology*, 47 Suppl 1:S261–70, 2009. URL <https://api.semanticscholar.org/CorpusID:14966082>.
- [18] Ana M. Levin, Ronald P. de Vries, Ana Conesa, Charissa de Bekker, Manuel Talón, Hildegard Menke, Noël N. M. E. van Peij, and Han A. B. Wösten. Spatial differentiation in the vegetative mycelium of *aspergillus niger*. *Eukaryotic Cell*, 6:2311 – 2322, 2007. URL <https://api.semanticscholar.org/CorpusID:13962412>.
- [19] Arman Vinck, Maarten Terlou, Wiebe R. Pestman, Edwin P. Martens, Arthur F. J. Ram, Cees A.M.J.J. van den Hondel, and Han A. B. Wösten. Hyphal differentiation in the exploring mycelium of *aspergillus niger*. *Molecular Microbiology*, 58, 2005. URL <https://api.semanticscholar.org/CorpusID:25043490>.
- [20] Charissa de Bekker, Oskar Bruning, Martijs J. Jonker, Timo M. Breit, and Han A. B. Wösten. Single cell transcriptomics of neighboring hyphae of *aspergillus niger*. *Genome Biology*, 12:R71 – R71, 2011. URL <https://api.semanticscholar.org/CorpusID:3723570>.
- [21] Anneke Bekker. Hyphal heterogeneity in *aspergillus niger*. 2011. URL <https://api.semanticscholar.org/CorpusID:85893807>.
- [22] Jun Lyu, Martin Tegelaar, Harm Post, Juan P. Moran Torres, Costanza Torchia, Af Maarten Altelaar, R. Bleichrodt, Hans de Cock, Luis G Lugones, and Han A. B. Wösten. Heterogeneity in spore aggregation and germination results in different sized, cooperative microcolonies in an *aspergillus niger* culture. *mBio*, 14, 2023. URL <https://api.semanticscholar.org/CorpusID:255593469>.
- [23] Maria Papagianni and Michael Matthey. Morphological development of *aspergillus niger* in submerged citric acid fermentation as a function of the spore inoculum level. application of neural network and cluster analysis for characterization of

- mycelial morphology. *Microbial Cell Factories*, 5:3 – 3, 2006. URL <https://api.semanticscholar.org/CorpusID:263970456>.
- [24] L. H. Grimm, Sven Kelly, Jan G. Hengstler, Andy Göbel, Rainer Krull, and Dietmar C. Hempel. Kinetic studies on the aggregation of aspergillus niger conidia. *Biotechnology and Bioengineering*, 87, 2004. URL <https://api.semanticscholar.org/CorpusID:9913113>.
- [25] Maryam Ijadpanahsaravi and Han A. B. Wösten. Germination strategies of stress resistant aspergillus conidia. *Current Opinion in Food Science*, 2024. URL <https://api.semanticscholar.org/CorpusID:269584162>.
- [26] David C. Rinker, Thomas J. C. Sauters, Karin Steffen, Adiyantara Gumilang, Huzefa A. Raja, Manuel Rangel-Grimaldo, Camila Figueiredo Pinzan, Patrícia Alves de Castro, Thaila Fernanda dos Reis, Endrews Delbaje, Jos Houbraken, Gustavo Henrique Goldman, Nicholas H. Oberlies, and Antonis Rokas. Strain heterogeneity in a non-pathogenic aspergillus fungus highlights factors associated with virulence. *Communications Biology*, 7, 2024. URL <https://api.semanticscholar.org/CorpusID:272399768>.
- [27] Tim J. H. Baltussen, Jan Zoll, Paul E. Verweij, and Willem J. G. Melchers. Molecular mechanisms of conidial germination in aspergillus spp. *Microbiology and Molecular Biology Reviews*, 84, 2019. URL <https://api.semanticscholar.org/CorpusID:208642285>.
- [28] Claude Lamarre, Serguei Sokol, J. P. Debeaupuis, Christine Henry, Céline Masoni Lacroix, Philippe Glaser, Jean Yves Coppee, Jean Marie François, and Jean Paul Latgé. Transcriptomic analysis of the exit from dormancy of aspergillus fumigatus conidia. *BMC Genomics*, 9:417 – 417, 2008. URL <https://api.semanticscholar.org/CorpusID:3052406>.
- [29] M. R. van Leeuwen, Pauline Krijgsheld, R. Bleichrodt, Hildegard Menke, Hein Stam, Jacques Stark, Han A. B. Wösten, and Jan Dijksterhuis. Germination of conidia of aspergillus niger is accompanied by major changes in rna profiles. *Studies in Mycology*, 74:59 – 70, 2012. URL <https://api.semanticscholar.org/CorpusID:24131978>.
- [30] Anne Lafon, Jeong-Ah Seo, Kap-Hoon Han, Jae-Hyuk Yu, and Christophe d'Enfert. The heterotrimeric g-protein ganb(α)-sfad(β)-gpga(γ) is a carbon source sensor involved in early camp-dependent germination in aspergillus nidulans. *Genetics*, 171:71 – 80, 2005. URL <https://api.semanticscholar.org/CorpusID:83831096>.

- [31] Pauline Krijgsheld, R. Bleichrodt, G. J. van Veluw, Fengfeng Wang, Wally H. Müller, Jan Dijksterhuis, and Han A. B. Wösten. Development in aspergillus. *Studies in Mycology*, 74:1 – 29, 2012. URL <https://api.semanticscholar.org/CorpusID:3029708>.
- [32] Nir Osherov and Gregory S. May. Conidial germination in aspergillus nidulans requires ras signaling and protein synthesis. *Genetics*, 155 2:647–56, 2000. URL <https://api.semanticscholar.org/CorpusID:15056931>.
- [33] Javier Barrios-González, Claudia Barbosa Martínez, A. Aguilera, and Maurice Raimbault. Germination of concentrated suspensions of spores from aspergillus niger. *Biotechnology Letters*, 11:551–554, 1989. URL <https://api.semanticscholar.org/CorpusID:8897649>.
- [34] Anthony P. J. Trinci and Christine Whittaker. Self-inhibition of spore germination in aspergillus nidulans. *Transactions of The British Mycological Society*, 51:594–596, 1968. URL <https://api.semanticscholar.org/CorpusID:83539867>.
- [35] Daryl D. Rowan. Volatile metabolites. *Metabolites*, 1:41 – 63, 2011. URL <https://api.semanticscholar.org/CorpusID:9681436>.
- [36] Dimitrios I. Tsitsigiannis and Nancy P. Keller. Oxylipins as developmental and host-fungal communication signals. *Trends in microbiology*, 15 3:109–18, 2007. URL <https://api.semanticscholar.org/CorpusID:32110042>.
- [37] Gilma Silva Chitarra, Tjakko Abée, Frank M. Rombouts, Maarten A. Posthumus, and Jan Dijksterhuis. Germination of penicillium paneum conidia is regulated by 1-octen-3-ol, a volatile self-inhibitor. *Applied and Environmental Microbiology*, 70:2823 – 2829, 2004. URL <https://api.semanticscholar.org/CorpusID:19828197>.
- [38] Digar Singh and Choong Hwan Lee. Volatiles mediated interactions between aspergillus oryzae strains modulate morphological transition and exometabolomes. *Frontiers in Microbiology*, 9, 2018. URL <https://api.semanticscholar.org/CorpusID:4625706>.
- [39] Digar Singh, Su Young Son, and Choong Hwan Lee. Critical thresholds of 1-octen-3-ol shape inter-species aspergillus interactions modulating the growth and secondary metabolism. *Scientific Reports*, 10, 2020. URL <https://api.semanticscholar.org/CorpusID:220350995>.
- [40] Gilma Silva Chitarra, Tjakko Abée, Frank M. Rombouts, and Jan Dijksterhuis. 1-octen-3-ol inhibits conidia germination of penicillium paneum despite of mild

- effects on membrane permeability, respiration, intracellular ph, and changes the protein composition. *FEMS microbiology ecology*, 54:1:67–75, 2005. URL <https://api.semanticscholar.org/CorpusID:24273006>.
- [41] Gilma Silva Chitarra. *Germination inhibitors of fungal spores: identification and mode of action*. PhD thesis, Wageningen University, 2003.
- [42] Neil A. R. Gow, Jean Paul Latgé, and Carol A. Munro. The fungal cell wall: Structure, biosynthesis, and function. *Microbiology Spectrum*, 5, 2017. URL <https://api.semanticscholar.org/CorpusID:5026076>.
- [43] Malitha C. Dickwella Widanage, Isha Gautam, Daipayan Sarkar, Frédéric Mentink-Vigier, Josh V. Vermaas, Shi-You Ding, Andrew S. Lipton, Thierry Fontaine, J.-P. Latgé, Ping Wang, and Tuo Wang. Adaptative survival of *Aspergillus fumigatus* to echinocandins arises from cell wall remodeling beyond β -1,3-glucan synthesis inhibition. *Nature Communications*, 15, 2024. URL <https://api.semanticscholar.org/CorpusID:271598394>.
- [44] Benjamin D. Strycker, Zehua Han, Blake Commer, Brian D. Shaw, Alexei V. Sokolov, and Marlan O. Scully. Cars spectroscopy of *Aspergillus nidulans* spores. *Scientific Reports*, 9, 2019. URL <https://api.semanticscholar.org/CorpusID:59945452>.
- [45] Liming Zhao, David Schaefer, and Mark R. Marten. Assessment of elasticity and topography of *Aspergillus nidulans* spores via atomic force microscopy. *Applied and Environmental Microbiology*, 71:955 – 960, 2005. URL <https://api.semanticscholar.org/CorpusID:7644450>.
- [46] Xue Kang, Alex Kirui, Artur Muszyński, Malitha C. Dickwella Widanage, Adrian Chen, Parastoo Azadi, Ping Wang, Frédéric Mentink-Vigier, and Tuo Wang. Molecular architecture of fungal cell walls revealed by solid-state nmr. *Nature Communications*, 9, 2018. URL <https://api.semanticscholar.org/CorpusID:49869140>.
- [47] Shaun M. Bowman and Stephen J. Free. The structure and synthesis of the fungal cell wall. *BioEssays*, 28, 2006. URL <https://api.semanticscholar.org/CorpusID:22623524>.
- [48] Anne Beauvais, Silvia Bozza, Olaf Kniemeyer, Céline Formosa, Viviane Balloy, Christine Henry, R W Roberson, Etienne Dague, Michel Chignard, Axel A. Brakhage, Luigina Romani, and Jean Paul Latgé. Deletion of the α -(1,3)-glucan synthase genes induces a restructuring of the conidial cell wall responsible for the avirulence of *Aspergillus fumigatus*. *PLoS Pathogens*, 9, 2013. URL <https://api.semanticscholar.org/CorpusID:1077628>.

- [49] Natsuno Shimizu, Tamaki Katagiri, Akira Matsumoto, Yoshihiko Matsuda, Hiroshi Arai, Nobumitsu Sasaki, Keietsu Abe, Toru Katase, Hiroki Ishida, Ken ichi Kusumoto, Michio Takeuchi, and Youhei Yamagata. Oryzapsins, the orthologs of yeast yapsin in aspergillus oryzae, affect ergosterol synthesis. *Applied Microbiology and Biotechnology*, 105:8481 – 8494, 2021. URL <https://api.semanticscholar.org/CorpusID:239034466>.
- [50] Sarah R Ball, Ann H. Kwan, and Margaret Sunde. Hydrophobin rodlets on the fungal cell wall. *Current topics in microbiology and immunology*, 2019. URL <https://api.semanticscholar.org/CorpusID:209474642>.
- [51] Takumi Tanaka, Yuki Terauchi, Akira Yoshimi, and Keietsu Abe. Aspergillus hydrophobins: Physicochemical properties, biochemical properties, and functions in solid polymer degradation. *Microorganisms*, 10, 2022. URL <https://api.semanticscholar.org/CorpusID:251102031>.
- [52] Han AB Wösten. Hydrophobins: multipurpose proteins. *Annual Reviews in Microbiology*, 55(1):625–646, 2001.
- [53] Jens Dynesen and Jens Nielsen. Surface hydrophobicity of aspergillus nidulans conidiospores and its role in pellet formation. *Biotechnology progress*, 19(3):1049–1052, 2003.
- [54] Marc Pihet, Patrick Vandepitte, Guy Tronchin, Gilles Rénier, Patrick Saulnier, Sonia Georgeault, Romain Mallet, Dominique Chabasse, Francçoise Symoens, and J. P. Bouchara. Melanin is an essential component for the integrity of the cell wall of aspergillus fumigatus conidia. *BMC Microbiology*, 9:177 – 177, 2009. URL <https://api.semanticscholar.org/CorpusID:8777822>.
- [55] Georgios Chamilos and Agostinho Carvalho. Aspergillus fumigatus dhn-melanin. *The Fungal Cell Wall: An Armour and a Weapon for Human Fungal Pathogens*, pages 17–28, 2020.
- [56] Isabel Valsecchi, Jennifer I. Lai, Emmanuel Stephen-Victor, Ariane Pillé, Audrey Beaussart, Victor Lo, Chi L.L. Pham, Vishukumar Aimanianda, Ann H. Kwan, Magalie Duchateau, Quentin Giai Gianetto, Mariette Matondo, Mélanie Lehoux, Donald C. Sheppard, Yves F. Dufrêne, Jagadeesh Bayry, J. Iñaki Guijarro, Margaret Sunde, and Jean Paul Latgé. Assembly and disassembly of aspergillus fumigatus conidial rodlets. *The Cell Surface*, 5, 2019. URL <https://api.semanticscholar.org/CorpusID:196902127>.
- [57] Azusa Takahashi-Nakaguchi, Kanae Sakai, Hiroki Takahashi, Daisuke Hagiwara, Takahito Toyotome, Hiroji Chibana, Akira Watanabe, Takashi Yaguchi, Masashi

- Yamaguchi, Katsuhiko Kamei, and Tohru Gono. *Aspergillus fumigatus* adhesion factors in dormant conidia revealed through comparative phenotypic and transcriptomic analyses. *Cellular Microbiology*, 20, 2017. URL <https://api.semanticscholar.org/CorpusID:3854030>.
- [58] Guy Tronchin, J. P. Bouchara, M Ferron, Gérald Larcher, and Dominique Chabasse. Cell surface properties of *aspergillus fumigatus* conidia: correlation between adherence, agglutination, and rearrangements of the cell wall. *Canadian journal of microbiology*, 41 8:714–21, 1995. URL <https://api.semanticscholar.org/CorpusID:34937464>.
- [59] L. H. Grimm, Sven Kelly, I. I. Völkerding, Rainer Krull, and Dietmar C. Hempel. Influence of mechanical stress and surface interaction on the aggregation of *aspergillus niger* conidia. *Biotechnology and Bioengineering*, 92, 2005. URL <https://api.semanticscholar.org/CorpusID:24999675>.
- [60] Philip C Nelson, Marko Radosavljevic, and Sarina Bromberg. *Biological Physics: Energy, Information, Life*. Chiliagon Science, 2003. URL <https://api.semanticscholar.org/CorpusID:267787080>.
- [61] Adolf Fick. Ueber diffusion. *Annalen der Physik*, 170(1):59–86, 1855. doi: <https://doi.org/10.1002/andp.18551700105>. URL <https://onlinelibrary.wiley.com/doi/abs/10.1002/andp.18551700105>.
- [62] Howard C. Berg. *Random Walks in Biology: New and Expanded Edition*. Princeton University Press, rev - revised edition, 1993. ISBN 9780691000640. URL <http://www.jstor.org/stable/j.ctv7r40w6>.
- [63] Toby Kay and Luca Giuggioli. Diffusion through permeable interfaces: Fundamental equations and their application to first-passage and local time statistics. *Physical Review Research*, 2022. URL <https://api.semanticscholar.org/CorpusID:252142011>.
- [64] Johannes G. Wijmans and Richard W. Baker. The solution-diffusion model: a review. *Journal of Membrane Science*, 107:1–21, 1995. URL <https://api.semanticscholar.org/CorpusID:93286517>.
- [65] Peter O. Brunn. Interaction between pores in diffusion through membranes of arbitrary thickness. *Journal of Membrane Science*, 19:117–135, 1984. URL <https://api.semanticscholar.org/CorpusID:94608682>.

- [66] Nicole J. Yang and Marlon J. Hinner. Getting across the cell membrane: an overview for small molecules, peptides, and proteins. *Methods in molecular biology*, 1266:29–53, 2015. URL <https://api.semanticscholar.org/CorpusID:33492435>.
- [67] Andreas Missner and Peter Pohl. 110 years of the meyer-overton rule: predicting membrane permeability of gases and other small compounds. *Chemphyschem : a European journal of chemical physics and physical chemistry*, 10 9-10:1405–14, 2009. URL <https://api.semanticscholar.org/CorpusID:41670339>.
- [68] Frank A.P.C. Gobas, Jean M. Lahittete, Gil Garofalo, Wan Ying Shiu, and Donald Mackay. A novel method for measuring membrane-water partition coefficients of hydrophobic organic chemicals: comparison with 1-octanol-water partitioning. *Journal of pharmaceutical sciences*, 77 3:265–72, 1988. URL <https://api.semanticscholar.org/CorpusID:750860>.
- [69] John F. Nagle, John C. Mathai, Mark L. Zeidel, and Stephanie A. Tristram-Nagle. Theory of passive permeability through lipid bilayers. *The Journal of General Physiology*, 131:77 – 85, 2008. URL <https://api.semanticscholar.org/CorpusID:451226>.
- [70] Rudolf Höber. Physikalische chemie der zelle und der gewebe. *Nature*, 112:93–93. URL <https://api.semanticscholar.org/CorpusID:4055737>.
- [71] Bridget Tang, Katie Chong, Walter W. Massefski, and Robert Evans. Quantitative interpretation of protein diffusion coefficients in mixed protiated–deuteriated aqueous solvents. *The Journal of Physical Chemistry. B*, 126:5887 – 5895, 2022. URL <https://api.semanticscholar.org/CorpusID:251281253>.
- [72] Jess V Nauman, Phil G. Campbell, Frederick Lanni, and John Lynde Anderson. Diffusion of insulin-like growth factor-i and ribonuclease through fibrin gels. *Biochemical journal*, 92 12:4444–50, 2007. URL <https://api.semanticscholar.org/CorpusID:42228357>.
- [73] Joseph G. H. Wessels. Hydrophobins: proteins that change the nature of the fungal surface. *Advances in microbial physiology*, 38:1–45, 1997. URL <https://api.semanticscholar.org/CorpusID:3016101>.
- [74] X. Wang, Fuxin Shi, Han A. B. Wösten, Harm Jan Hektor, Bert Poolman, and George Thomas Robillard. The sc3 hydrophobin self-assembles into a membrane with distinct mass transfer properties. *Biophysical journal*, 88 5:3434–43, 2005. URL <https://api.semanticscholar.org/CorpusID:16739076>.

- [75] Friederike Nolle, Leonhard J Starke, Alessandra Griffó, Michael Lienemann, Karin Jacobs, Ralf Seemann, Jean-Baptiste Fleury, Jochen S. Hub, and Hendrik Hähl. Hydrophobin bilayer as water impermeable protein membrane. *Langmuir*, 39:13790 – 13800, 2023. URL <https://api.semanticscholar.org/CorpusID:262061982>.
- [76] Sophie Paris, J. P. Debeaupuis, Reto Crameri, Marion G. Carey, F. Charles, Marie-Christine Prevost, Christine Schmitt, Bruno Philippe, and Jean Paul Latgé. Conidial hydrophobins of *aspergillus fumigatus*. *Applied and Environmental Microbiology*, 69:1581 – 1588, 2003. URL <https://api.semanticscholar.org/CorpusID:29195537>.
- [77] Tong Zhang and Hff Fang. Effective diffusion coefficients of glucose in artificial biofilms. *Environmental Technology*, 26:155 – 160, 2005. URL <https://api.semanticscholar.org/CorpusID:41242504>.
- [78] Nicklaus Carter, Julia Towne, and David J. Neivandt. Finite element analysis of glucose diffusivity in cellulose nanofibril peripheral nerve conduits. *Cellulose*, 28:2791 – 2803, 2021. URL <https://api.semanticscholar.org/CorpusID:231858923>.
- [79] Robert Charles Hardy and Robert L. Cottington. Viscosity of deuterium oxide and water in the range 5 to 125 c. *Journal of research of the National Bureau of Standards*, 42:573, 1949. URL <https://api.semanticscholar.org/CorpusID:97507608>.
- [80] D.A.T. Dick. The permeability coefficient of water in the cell membrane and the diffusion coefficient in the cell interior. *Journal of theoretical biology*, 7 3:504–31, 1964. URL <https://api.semanticscholar.org/CorpusID:10977619>.
- [81] G J Bresseleers, H. L. Goderis, and Paul P. Tobback. Measurement of the glucose permeation rate across phospholipid bilayers using small unilamellar vesicles. effect of membrane composition and temperature. *Biochimica et biophysica acta*, 772 3: 374–82, 1984. URL <https://api.semanticscholar.org/CorpusID:9584953>.
- [82] Henry V Jakubowski, Patricia Flatt, Henry Agnew, and Delmar Larsen. Fundamentals of biochemistry, a free and new libretext book for undergraduate courses. *The FASEB Journal*, 36, 2022. URL <https://api.semanticscholar.org/CorpusID:248635799>.
- [83] Stanley Brul, J Nussbaum, and S. K. Dielbandhoesing. Fluorescent probes for wall porosity and membrane integrity in filamentous fungi. *Journal of Microbiological Methods*, 28:169–178, 1997. URL <https://api.semanticscholar.org/CorpusID:85293622>.

- [84] Surya K. Ghosh, Andrey G. Cherstvy, and Ralf Metzler. Non-universal tracer diffusion in crowded media of non-inert obstacles. *Physical chemistry chemical physics : PCCP*, 17 3:1847–58, 2014. URL <https://api.semanticscholar.org/CorpusID:16336167>.
- [85] Andrea Hille, Thomas R. Neu, Dietmar C. Hempel, and Harald Horn. Effective diffusivities and mass fluxes in fungal biopellets. *Biotechnology and Bioengineering*, 103, 2009. URL <https://api.semanticscholar.org/CorpusID:24078572>.
- [86] Siti Nur Izzati Saiful Anuar, Farhana Othman, Tay Chia Chay, and Nor Atikah Husna Ahmad Nasir. Biosorption of mercury ion (hg^{2+}) using live and dead cells of *rhizopus oryzae* and *aspergillus niger* : Characterization, kinetic and isotherm studies. *Journal of Pure and Applied Microbiology*, 14:1749–1760, 2020. URL <https://api.semanticscholar.org/CorpusID:225014932>.
- [87] Katarzyna E. Nowak, Adrian Wiater, Adam Choma, Dariusz Wiącek, Andrzej Bieganowski, Marek Siwulski, and Adam Waśko. Fungal (1-3)- α -d-glucans as a new kind of biosorbent for heavy metals. *International journal of biological macromolecules*, 2019. URL <https://api.semanticscholar.org/CorpusID:195843248>.
- [88] Zhuowei Cheng, Ke Feng, Yousheng Su, Jiexu Ye, Dongzhi Chen, Shihan Zhang, Xiaoming Zhang, and Dionysios Demetriou Dionysiou. Novel biosorbents synthesized from fungal and bacterial biomass and their applications in the adsorption of volatile organic compounds. *Bioresource technology*, 300:122705, 2019. URL <https://api.semanticscholar.org/CorpusID:210158540>.
- [89] Huimin Zhang, Dan Wu, Qilin Huang, Zhiyu Liu, Xiaogang Luo, Shanbai Xiong, and Tao Yin. Adsorption kinetics and thermodynamics of yeast β -glucan for off-odor compounds in silver carp mince. *Food chemistry*, 319:126232, 2020. URL <https://api.semanticscholar.org/CorpusID:213316784>.
- [90] Hans Swenson and Nicholas P. Stadie. Langmuir’s theory of adsorption: A centennial review. *Langmuir : the ACS journal of surfaces and colloids*, 35 16:5409–5426, 2019. URL <https://api.semanticscholar.org/CorpusID:85529840>.
- [91] Gopal C. Paul and C. R. Thomas. Characterisation of mycelial morphology using image analysis. *Advances in biochemical engineering/biotechnology*, 60:1–59, 1998. URL <https://api.semanticscholar.org/CorpusID:27768320>.
- [92] Stefan Schmidededer, Lars Barthel, Tiaan Friedrich, Michaela Thalhammer, Ludwig Niessen, Vera Meyer, and Heiko Briesen. Biotechnology and bioengineering. 2019. URL <https://api.semanticscholar.org/CorpusID:73449481>.

- [93] Katherine Celler, Cristian Picioreanu, Mark C. M. Loosdrecht, and Gilles P. van Wezel. Structured morphological modeling as a framework for rational strain design of streptomyces species. *Antonie Van Leeuwenhoek*, 102:409 – 423, 2012. URL <https://api.semanticscholar.org/CorpusID:3082757>.
- [94] Stefan Schmidededer, Henri Müller, Lars Barthel, Tiaan Friedrich, Ludwig Niessen, Vera Meyer, and Heiko Briesen. Universal law for diffusive mass transport through mycelial networks. *Biotechnology and Bioengineering*, 118:930 – 943, 2020. URL <https://api.semanticscholar.org/CorpusID:226295463>.
- [95] Rudibert King. Mathematical modelling of the morphology of streptomyces species. *Advances in Biochemical Engineering Biotechnology*, 60:95–124, 1998. URL <https://api.semanticscholar.org/CorpusID:81193860>.
- [96] Fordyce A. Davidson. Mathematical modelling of mycelia: a question of scale. *Fungal Biology Reviews*, 21:30–41, 2007. URL <https://api.semanticscholar.org/CorpusID:55811444>.
- [97] Salomon Bartnicki-Garcia, Frank Hergert, and Gerhard Gierz. Computer simulation of fungal morphogenesis and the mathematical basis for hyphal (tip) growth. *Protoplasma*, 153:46–57, 1989. URL <https://api.semanticscholar.org/CorpusID:26356194>.
- [98] Salomon Bartnicki-Garcia, David D Bartnicki, Gerhard Gierz, Rosa María López-Franco, and Charles E. Bracker. Evidence that spizenkörper behavior determines the shape of a fungal hypha: a test of the hyphoid model. *Experimental mycology*, 19 2:153–9, 1995. URL <https://api.semanticscholar.org/CorpusID:25159340>.
- [99] Sonia Marín, Vicente Sanchis, Alberto López Teixido, R Saenz, Antonio J. Ramos, Inmaculada Viñas, and Naresh Magan. Water and temperature relations and microconidial germination of fusarium moniliforme and fusarium proliferatum from maize. *Canadian journal of microbiology*, 42 10:1045–50, 1996. URL <https://api.semanticscholar.org/CorpusID:20389193>.
- [100] Philippe Dantigny, Sidjè Paule-Marina Nanguy, Daniela Judet-Correia, and Maurice Bensoussan. A new model for germination of fungi. *International journal of food microbiology*, 146 2:176–81, 2011. URL <https://api.semanticscholar.org/CorpusID:38620666>.
- [101] J. Crank. *The Mathematics Of Diffusion*. 1956. URL <https://api.semanticscholar.org/CorpusID:118605965>.
- [102] Alan Mathison Turing. The chemical basis of morphogenesis. *Bulletin of mathematical biology*, 52:153–197, 1990.

- [103] Thomas A. Witten and Leonard M. Sander. Diffusion-limited aggregation, a kinetic critical phenomenon. *Physical Review Letters*, 47:1400–1403, 1981. URL <https://api.semanticscholar.org/CorpusID:120168490>.
- [104] Nicholas J. Savill and Paulien Hogeweg. Modelling morphogenesis: From single cells to crawling slugs. *Journal of theoretical biology*, 184 3:229–235, 1997. URL <https://api.semanticscholar.org/CorpusID:1611700>.
- [105] Leonor Michaelis, Maud L Menten, et al. Die kinetik der invertinwirkung. *Biochem. z.*, 49(333-369):352, 1913.
- [106] H Robert Horton, Laurence A Moran, K Gray Scrimgeour, Marc D Perry, and J David Rawn. *Principles of biochemistry*. 2006.
- [107] E. Otto and Heinz Fissan. Brownian coagulation of submicron particles. *Advanced Powder Technology*, 10:1–20, 1999. URL <https://api.semanticscholar.org/CorpusID:93058148>.
- [108] Jeffrey D. Picka. Statistical inference for disordered sphere packings. *Statistics Surveys*, 6:74–112, 2007. URL <https://api.semanticscholar.org/CorpusID:8801717>.
- [109] Wim Van Saarloos, Vincenzo Vitelli, and Zorana Zeravcic. *Soft Matter: Concepts, Phenomena, and Applications*. Princeton University Press, 2024.
- [110] D. A. T. Dick. The rate of diffusion of water in the protoplasm of living cells. *Experimental cell research*, 17 1:5–12, 1959. URL <https://api.semanticscholar.org/CorpusID:43911310>.
- [111] Michael T Heath. *Scientific computing: an introductory survey, revised second edition*. SIAM, 2018.
- [112] Tommaso Toffoli and Norman Margolus. *Cellular automata machines: a new environment for modeling*. MIT press, 1987.
- [113] Steven C Chapra, Raymond P Canale, et al. *Numerical methods for engineers*, volume 1221. Mcgraw-hill New York, 2011.
- [114] Darius Pupeikis, Vytautas Stankevičius, and Arūnas Burlingis. The effect of the fourier number on calculation of an unsteady heat transfer of building walls. *Journal of Civil Engineering and Management*, 16:298–305, 2010. URL <https://api.semanticscholar.org/CorpusID:109838722>.
- [115] Shin-Taek Jeong. Stability of finite difference schemes on the diffusion equation with discontinuous coefficients. 2018. URL <https://api.semanticscholar.org/CorpusID:32296632>.

- [116] Didier Rajon, Phillip W. Patton, A. P. Shah, Christopher J. Watchman, and Wesley E. Bolch. Surface area overestimation within three-dimensional digital images and its consequence for skeletal dosimetry. *Medical physics*, 29 5:682–93, 2002. URL <https://api.semanticscholar.org/CorpusID:23912422>.
- [117] Keh Chin Chang and U. J. Payne. Numerical treatment of diffusion coefficients at interfaces. *Numerical Heat Transfer Part A-applications*, 21:363–376, 1992. URL <https://api.semanticscholar.org/CorpusID:120393842>.
- [118] María Florencia Mazzobre, M. Román, Ariel Feo Mourelle, and Horacio R. Corti. Octanol-water partition coefficient of glucose, sucrose, and trehalose. *Carbohydrate research*, 340 6:1207–11, 2005. URL <https://api.semanticscholar.org/CorpusID:11188601>.
- [119] Birger Brodin, Bente Steffansen, and Carsten Uhd Nielsen. Passive diffusion of drug substances: the concepts of flux and permeability. In *Molecular Biopharmaceutics*, 2010. URL <https://api.semanticscholar.org/CorpusID:12995364>.
- [120] Zbigniew Ulanowski and Ian Keith Ludlow. Water distribution, size and wall thickness in lycoperdon pyriforme spores. *Fungal Biology*, 93:28–32, 1989. URL <https://api.semanticscholar.org/CorpusID:84216118>.
- [121] Sheldon M Ross. *Simulation*. academic press, 2022.
- [122] L Mazmalyan, V Ohanian, and D Trietsch. The lognormal central limit theorem for positive random variables (working paper). 2008.
- [123] Heino Prinz. Hill coefficients, dose-response curves and allosteric mechanisms. *Journal of Chemical Biology*, 3:37–44, 2010. URL <https://api.semanticscholar.org/CorpusID:11374436>.
- [124] Guido Pontecorvo, Joseph A. Roper, L. M. Chemmons, K. D. Macdonald, and Andrew Bufton. The genetics of aspergillus nidulans. *Advances in genetics*, 5: 141–238, 1953. URL <https://api.semanticscholar.org/CorpusID:5482740>.
- [125] Zhiyong Zhang, Jianyong Zhu, and Feiping Nie. A novel hybrid adaptive differential evolution for global optimization. *Scientific Reports*, 14, 2024. URL <https://api.semanticscholar.org/CorpusID:271950331>.
- [126] Michael JD Powell. *A direct search optimization method that models the objective and constraint functions by linear interpolation*. Springer, 1994.
- [127] Qing Liu and Donald A. Pierce. A note on gauss—hermite quadrature. *Biometrika*, 81:624–629, 1994. URL <https://api.semanticscholar.org/CorpusID:121043480>.

- [128] Liyanage D. Fernando, Wancheng Zhao, Isha Gautam, Ankur Ankur, and Tuo Wang. Polysaccharide assemblies in fungal and plant cell walls explored by solid-state nmr. *Structure*, 2023. URL <https://api.semanticscholar.org/CorpusID:261016854>.
- [129] Johanna K. S. Tiemann, Magdalena Szczuka, Lisa Bouarroudj, Mohamed Oussaren, Steven Garcia, Rebecca J. Howard, Lucie Delemotte, Erik Lindahl, Marc Baaden, Kresten Lindorff-Larsen, Matthieu Chavent, and Pierre Poulain. Mdverse: Shedding light on the dark matter of molecular dynamics simulations. *bioRxiv*, 2023. URL <https://api.semanticscholar.org/CorpusID:258487280>.